Detection Power, Temporal Response, and Spatial Resolution of IRON fMRI in Awake, Behaving Monkeys at 3 Tesla

by

Francisca Maria Pais Horta Leite
Licenciada in Technological Physics Engineering
Technical University of Lisbon, 1997

Submitted to the Harvard-MIT Division of Health Sciences and Technology
in partial fulfillment of the requirements for the degree of

Doctor of Philosophy

at the

MASSACHUSETTS INSTITUTE OF TECHNOLOGY
[February 2007]
September 2006

Signature of Author.....
Harvard-MIT Division of Health Sciences and Technology
September 26th, 2006

Certified by.....
Joseph B. Mandeville, Ph.D.
Instructor in Radiology at HMS
Assistant in Physics at MGH/Radiology
Thesis supervisor

Accepted by.....
Martha L. Gray, Ph.D.
Edward Hood Taplin Professor of Medical and Electrical Engineering
Director, Harvard-MIT Division of Health Sciences and Technology

Detection Power, Temporal Response, and Spatial Resolution of IRON fMRI in Awake, Behaving Monkeys at 3 Tesla

by

Francisca Maria Pais Horta Leite

Submitted to the Harvard-MIT Division of Health Sciences and Technology
in partial fulfillment of the requirements for the degree of

Doctor of Philosophy in Medical Physics

Abstract

The main goal of this thesis was to systematically characterize the detection sensitivity, temporal response, and spatial resolution of IRON contrast for fMRI within the awake, behaving monkey. Understanding these issues provides insights into the physiology of the functional response to local changes in brain activity, enables researchers to optimize experimental designs, and delineates the advantages and limitations of neuroimaging within this important animal model.

The injection of the iron oxide contrast agent (MION) provided a 9-fold increase in eficiency for block designs relatively to BOLD contrast. Because the hemodynamic response function acts as a low-pass filter on neural activation to attenuate the size of differential responses to alternate stimuli, this factor dropped to approximately 2 for rapidly presented stimuli. Detection efficiency for event-related stimulus designs for BOLD and IRON contrasts could be optimized using random or semi-random distributions for interstimulus intervals. Small increases in predictability could be traded for large gains in efficiency, particularly for the IRON method.

A general linear model was successfully employed to describe IRON and BOLD impulse response functions. Both responses were accurately described by a bimodal exponential model with similar time constants, a fast (4.5 sec) and a slow (13.5 sec). The slow response comprised 80% of IRON signal, and was responsible for the BOLD post-stimulus undershoot. It likely encompasses changes in post-arteriole blood volume.

Optimized IRON activation maps do not show activation in draining veins or draining tissue, in contrast with BOLD contrast. To examine what happens at the level of small vessels and capillaries, we used point-image stimuli to measure IRON and BOLD point spread functions (PSF) in V1. We estimated an IRON PSF no larger than approximately 0.4 mm, and a BOLD PSF with twice the size.

Severe image distortions arising from monkey's body motion outside of the field of view currently limit the achievable spatial resolution. Preliminary data suggests multi-shot EPI with navigators may be useful in improving image stability at higher resolution for IRON fMRI, which can employ short echo times to minimize phase variations, while achieving maximum efficiency by increasing the MION dose.

Thesis Supervisor: Joseph B. Mandeville
Title: Instructor in Radiology at HMS and Assistant in Physics at MGH/Radiology

Acknowledgments

The time has finally arrived. It is hard to believe that my never ending PhD is actually coming to an end. It has been quite a journey. A journey whose positive outcome I owe first and foremost to Joe Mandeville. There are no words to express how grateful I am for his unlimited support, understanding and enthusiasm. Joe's office door is always open when I need advice, his codes always changed within a minute's notice to make my life easier. What I have learned from Joe is beyond imagination. His patience, tolerance and humility have inspired me as a researcher and as an individual, and I have always been able to count on Joe's thoughtfulness and friendship in some difficult periods of my life. Some moments are forever engraved in my mind: Joe and I trying to get Falco's head through the opening of the chair, the most difficult task of my PhD; watching drops of sweat running down Joe's nose while trying to inject MION in a monkey's femoral vein (even if I was the one holding the needle); some comparatively relaxed moments at the scanner, discussing strategies to reduce image distortions; the many talks we had in Joe's office, which would not only address the most recent modifications to xdisplay, but would range all the way from noise autocorrelation models, to finding Joe's childhood house in Montana with Google maps, or giving me suggestions about where to go during my California road trip... For all this and so much more, thank you Joe. It has been a great pleasure to work under your supervision. I'll be waiting for your visit to Portugal so I can take you to "slurp sardines" while drinking a Portuguese beer at some nice restaurant overseeing the beach, across the Atlantic from the Martinos Center.

If it wasn't for Bruce Rosen, the director of such an impressive center as the Martinos Center, to take time to read through his email and reply to some 24 year old student from Portugal, asking if she could come to the center to conduct research towards a PhD degree from Portugal, I would never have come to Boston in the first place. From that moment on, Bruce's support and enthusiasm about my work at the center, my application first to MIT and later to HST, has only increased. Bruce is the most enthusiastic person I know: every time I have the chance to spend one hour in Bruce's office, my motivation sky rockets. Unfortunately this thesis does not end with a paper in Science, but still, I hope you find I honored the amazing opportunity you gave me.

I would not have learned half of what I learned about MRI if it wasn't for Professor David Cory. And more importantly, I think I only really started to appreciate the beauty of MRI after sitting through 22.56J and preparing for my oral exam, both times under his supervision. It was David Cory who first suggested that I should read the initial Peter Mansfield's papers introducing k-space formalism in analogy to x-ray scattering. It was also David Cory who taught me about

product operators, and to make me almost want to switch to spectroscopy so I could apply what I was learning about quantum coherences. I also owe to Professor Cory supporting me through my successful application to HST, and to agree to serve in my thesis committee.

I am truly grateful to all the members of my thesis committee, Joe Mandeville, Bruce Rosen, David Cory, Tomaso Poggio and Roger Tootell, for all the constructive suggestions, valuable insight, and firm support demonstrated throughout the duration of my thesis work. I also acknowledge the financial support from Fundação para a Ciência e Tecnologia (doctoral fellowship PRAXIS XXI BD/13473/97), and Fundação Calouste Gulbenkian (doctoral fellowhip no 43057).

Working with monkeys is not an easy task, and it would have been an impossible one without the excellent Monkey Group at the Martinos Center. If Wim Vanduffel hadn't relocated here, I doubt half of this thesis would have happened. My many thanks to Leeland Ekstrom, Tamara Knutsen, Reza Rajimehr, Mark Khachaturian, Hauke Kolster, Helen Deng, Lori Jasinski, John Arsenault, and the person who started it all, Doris Tsao.

Moving from Portugal to the Martinos Center, at the time the NMR Center at MGH, was facilitated because of people like Ken Kwong. Ken in the "glue" of the Martinos Center. Even though Ken has a nice office in the second floor, if you need to see him you can be sure you'll find him talking with the students, because that is where he loves to be. Rick Hoge was also incredibly helpful in my first months at the Center. Nouchine Hadjikhani was not only my first friend at the Martinos Center, but also the first person to make me feel at home in Boston. She introduced me to many people at the Martinos Center who greatly contributed in making my life there a lot easier and happier: Sari Levanen, Mette Wiegel, Dave Tuch, and Christian Haselgrove. There are many people I would, for one reason or another, like to acknowledge at the center: Larry Wald, Bruce Jenkins, Iris Chen, Tim Reese, Yuka Sasaki, Fa-Hsuan Lin, Doug Greve, Scott Packard, Christopher Moore, Randy Gollub, Jorge Jovicich, Paul Raines, Vicka Corey, David Covin, Sam Mehl, Thomas Benner, Christina Triantafyllou, Andreas Potthast, Chris Wiggins, Mary Foley, Jill Clark, Larry White, Simon Sigalovsky, and I am sure many others I am forgetting. I have also appreciated the help of Maria Angela Franceschini, George Themelis and Juliette Selb. Extremely important in the successful completion of this PhD have been Bruce's personal secretaries, especially Carol Barnstead and Linda Butler. Young "Superman" Kim always manages to put a smile on my face. I would also like to thank my fellow graduate students for all the support and help in many different aspects of my work at the center: Dan Wehner, Poe-Joe Chen, Leeland Ekstrom, Mark Khachaturian, Peng Yu, Shuning Huang, and Miriam Makhlouf. This list would not be complete without Leonardo Angelone, Cherif Sahyoun and

Megan Blackwell. You have been much more than colleagues; you are good friends who I know I can always count on. Megan has been with me since the start, has accompanied me through the highs and lows at the Martinos Center, at MIT, and in life. You are a special person, who I wish all the best in your PhD. Oh, and of course, a special thanks to Rob Nabuurs, who convinced me that everything is possible.

If there is something I am really proud of, it is to be a student at MIT. From the amazing professors, to the helpful and caring staff, to the inspiring students, everything at MIT has contributed to make my stay there, in the most amazing university campus I know, an unforgettable experience. The professors and students at the Nuclear Engineering Department were my first home at MIT. I would especially like to thank Professor Molvig for his truly stimulating lectures, Professor Sow-Hsin Chen for a second chance, and Professor Alan Jasanoff for attending by defense. Many were the students that started with me whom I like to acknowledge, even though some of them are already applying to faculty positions while I am still a mere graduate student (the bastards): Antonino Romano, Bilge Yildiz, Jacopo Saccheri, amongst others. The best food I had for lunch at MIT I owe to Antonio Faraone, who has a postdoc could take me to Pritchett's. And from the same period I cannot forget Cansu Tunca and Ali Ergut.

HST is my home away from home. If it wasn't for Professor Roger Mark I would never have applied to MEMP, one of the best decisions of my life. Cathy Modica, Domingo Altarejo, Ron Smith, I will never forget you. Taking classes with HST faculty has greatly enriched my life, and made be seriously consider applying to Medical School. But the most amazing experience was ICM at Mount Auburn Hospital with Valerie Pronio-Stelluto. Furthermore, I have made many good friends at HST. First and foremost, Blanca Himes and Jenny Mu, my companions in Pathology and Anatomy. I truly hope we will always keep in touch. Riccardo Lattanzi and Lisa Treat, you've made ISMRM even better! Nik Kojic has always succeeded in making me laugh, even when I only wanted to cry. Caroline Boudoux, you make the best fruit salad. I would also like to acknowledge Georg Gerber, Mike Hemond, Erika Wagner and Martin Zalesak.

If I had to guess, at the time I finished my degree in Portugal, that I would ever be admitted to MIT, it would take me a million years. But now, looking back, I see how everything in my life fell in place to take me where I am. Many people contributed to this endeavor. Professor Eduardo Ducla-Soares was the first person to shift my attention to the field of Biophysics and Medical Physics. His enthusiastic lectures have not only aroused my curiosity about functional neuroimaging (amongst so many other subjects), but have also inspired me to pursue an academic career. Professor Pedro Miranda was also instrumental in my successful application to MIT, and I

will always remember Professor Dinis Pestana and its amazing Statistics classes in the first year of my doctoral program in Portugal.

Studying at Instituto Superior Técnico has been another extremely important factor putting me in this road whose end I now see. More than learning about Physics and Math, being a student in the Physics Department taught me how to think. Many were the Professors that inspired me at IST, and some of them I only truly valued when I was already at MIT.

I would also like to acknowledge Professor Gabriel Feio at the Instituto de Física Matemática, the first person to teach me about NMR, while supervising my final year project in IST.

This list would not be complete if I didn't mention a great teacher I had in High School: teacher Hernãni made me love Physics and Math, and inspired me to always aim higher.

The research world has many problems, but attending conferences in paradisiacal places is the least of them. Every year new and old friends meet at the ISMRM conference. Hanging out with the Portuguese gang is always a pleasure: Zé "The Beatles' Hairdo" Pedro, Rita "Contagious Laugh" Nunes, and Tiago "Nanni Moretti" Rodrigues, are part of the reason it is hard for me to think about leaving Science. I would also like to acknowledge Patrícia Figueiredo and Mário Secca.

My life in the USA has been made a lot easier due to all the friends I have made here. One of the first was Ricardo Schiappa, who not only convinced me to apply to MIT, but also helped me immensely in the first few years.

My roommates throughout these last 7 years, Leonor Sarmento (and Manel!), Valentina Sequi and Birgit Schoeberl were a pleasure to live with, and became good friends. Thanks to Birgit I met amazingly nice people like Brit Assmus, Lilla Zollei, Hélène Karcher and David Garcia-Alvarez, among others. With Birgit I started skiing regularly again, went surfing in the freezing New England waves, and organized awesome parties at our place. Wolfgang Bergmeier, Ellen O'Shaughnessy, Florian Altmann, regular attendants of our parties and ski companions, it's been wonderful meeting you. I would also like to acknowledge Juan Pedraza, the best salsa dancer I know, the always creative Yasmine Abbas, and the patient Franco Vairani.

The first Portuguese I met in the States was Luísa Marcelino, thanks to Lena Paveia. Thanks Luísa for all the helpful talks we had throughout the years. The second was Inês Sousa, who not only helped me find a house but also introduced me to PSA, the MIT Portuguese Student Association.

Portuguese in Boston – Cambridge are like grapes, you meet one you meet a whole bunch. And so far, the harvest as been amazing: Cátia Fonseca and Beatriz Oliveira quickly became good friends; Nuno, Manela e Francisca, Francisco Veloso, Carla Vale, Camões, and many others from

those "ancient" first years; João Rocha, always there; Rodrigo Miragaia, Sara Maia, Xana Sanfins, Pedro Ferreira in the second round; Xana Frias, Zé "Fofo" Antão, Inês Baptista (Oh Kiiiika!!), Cristina Nogueira, Pedro Carvalho and Inezinha, Joana Sá, Joana Loureiro, Joana Felgueiras, André Valente, are now good friends who I know I can count on, and regular party companions. Inbal and Rui, you are such a special couple, I am so happy I met you! And the ultimate dinner organizers: Miguel and his huge glasses of "water" and Rita, who never lets me say no. Because of them, biking home at 6 am, after eating the most amazing fava beans, and then "a bucha" around 4 am, has become common. Jumping on the sofa, dancing, and practicing hand stands against the wall, are also frequent events. As are laughing, sharing and talking with Rita about everything and about nothing, one more time realizing what a special person and a wonderful friend she is.

Tiago: first we hated each other, then we were friends, then we weren't, then he took me to Yoga, and then that dinner at Central Kitchen, and before I realized he was my best friend. In Cambridge, somewhere in the Pacific Highway, in Portugal, in London, I know I can always count on you to talk, to laugh, to jump of joy, or to take me out when I just want to cry in bed.

Talking of Portuguese in Boston, is talking of suffering and cheering for the Portuguese Soccer Team. I made the promise, during the last world cup, that if Portugal won to Holland (sorry Rob!) I would include Scolari in my acknowledgments. I do it with pleasure. I thank Scolari, and Figo, and Ricardo, and all the amazing Portuguese players for showing us we can do it, for uniting a country, for making us, emigrants in a strange land, feel more connected.

Even after an eternity abroad, my friends in Portugal still believe I will come back. And more than that, I like to believe they still hope I will ;) From the remote golden fields in Alentejo, to the deep blue water of the Atlantic in Torreira, I have amazing friends who have always been there for me. In Estremoz, for more years than I like to remember: Ana Preta, Raquel Cortes, Ana Taborda, Ana Raposo, Sofia Lameiras, Maria João, Pedro Costa, Tó Godinho, Nuno Pereira, Bruno Grades, Nuno Rato. This list is not complete without Miguel Cortes, my alter ego, and Ana Anjinho. Ana is more than a friend, she's family. There are no words to express how important she is in my life. She has always been there for me, and I know she always will, and so will Zezinha and João. Thank you! And please, keep buying Ferrero Rocher.

Every time I arrive in Torreira, the first thing I like to do is to go to the beach and smell the ocean. And then I go home, slurp some "carapaus" grilled by my dad in the backyard, and wait anxiously for the time to go out and meet my friends: Bernardo Aguiar, I miss going to Alberto with you; Carlos Goulão, I still can't believe you are ditching me; André Goulão, thanks to msn you are always there for me; Filipe Prata, I wish you a lot of "sussexo"; Zé e Sofia, thank you so

much for all your help; Jorge and Daniela, when are you getting married? Claúdia Tavares, Ana Sofia, Inês Soares, Margarida Araújo e Sá, Filipa Sequeira, Kikas, I miss you girls! Sofia Rocha, is there a guest room? Ana Teresa, I miss our walks along the beach or down 5th Avenue. Margarida Aguiar (Mags!), I can hardly wait to meet Bernardinho next time I invite myself to dinner at yours and Nuno's wonderful "canteen". Maria, Maria, Maria... you've always made me dream higher.

Time traveling to Domus Nostra: Leonor Vasconcelos (thank you, thank you, thank you!), Madalena Melo, Teresa Oliveira, Teresa Pereira, Teresa Morais, those were happy times! Even Marilda couldn't stop us! Joana, my dear Joana, how I miss you. Margariiiida Meeelo, what can I say that makes justice to how much I like you?

At Técnico: Marta Fajardo and Laura Barros, you made me feel like I belonged. João Tavares Cabral, Guilherme Milhano and Nuno Romão, thanks for your help and friendship. Studying at IST was great, but it wouldn't have been the same without Ana Isa, Palila, Rodrigo Albuquerque, and Luís Guilherme, among others.

Moving forward a few years: Ana Sá da Costa (Bija!), please stop getting pregnant so we can go out again! Vera Appleton, thank you for caring so much. Zé Diogo, Duarte Morais Cabral, Jota, António Costa Quinta e Joana, Tomás Marques, you've enriched my life.

A detour to Belgium: Lies, my dear friend, you bring out the best in me.

João Paveia, I wish you could be here.

João. Thank you. For showing me the world. For everything. You will always be in my heart.

Conceicão Berger, thank you for all your support and friendship, you are my role model. My dear Tomás, thank you for being such a special and refreshing person. Tio Zé, António, Tia Nené, Tio Jorge, Avô Meneses, Tia Manela, you are forever part of my family.

And finally... Tia Benedita, who could imagine I would miss you so much. Tia Angelina, I know we are always fighting but I really like you. Maneu and Jaime, I'm so proud we are related. Teresa, thanks for being the best sister-in-law I could ask for. André, Afonso, Carolina e Eduardo, you are the greatest gifts my brothers could have given me. I miss you immensely. Ok, and now I am crying. Gá, Zé, I love you so much. You are the best brothers in the world. Francisco, this thesis is in your memory. Mom, Dad... words fail me.

Para a Luísa e o Valério,
os meus queridos Pais

Contents

List of Figures

List of Tables

Chapter 1

Introduction

1.1 Outline of the thesis

The **main goal** of this thesis was to systematically characterize the detection sensitivity, temporal response, and spatial resolution of a new method of contrast for functional MRI (fMRI) within the awake, behaving macaque. Understanding these issues provides insights into the physiology of the functional response to local changes in brain activity, enables researchers to optimize experimental designs, and delineates the advantages and limitations of neuroimaging within this important animal model.

While BOLD (blood oxygen level dependent) signal is an effective neuroimaging tool for studying human populations, investigations in anesthetized rodents (1998, 1999) demonstrated that the use of exogenous contrast agent could significantly enhance detection power relative to BOLD fMRI, while the temporal response was modified. With this as a starting point, we sought to extend these methods to primates in the awake state, and then to exploit this model for careful comparisons of functional methodologies.

The remainder of this chapter provides a brief history of the foundations of functional brain imaging, a description of essential physiology relevant to the functional responses employed in our studies, and an overview of fMRI. Obviously, many aspects of MRI physics are common to the alternative methodologies enabled by this flexible imaging modality, whereas the choice of contrast for fMRI can significantly modify experimental choices and functional results.

Chapter 2 of this thesis measures and compares the functional sensitivity of BOLD signal relative to fMRI that employs an exogenous contrast agent; we refer to the latter as the IRON method (increased relaxation for optimized neuroimaging). BOLD and IRON studies were performed for different types of stimulus' paradigms. Special care was taken to accurately measure temporal fMRI responses, and to estimate the impulse response functions for BOLD and IRON contrasts using a basis of mono-exponential functions. In order to achieve this goal, a simple model of the hemodynamic response to neuronal activation had to be established. A general linear model provided a good first order approximation for BOLD and IRON responses, in agreement with previous reports for BOLD fMRI (e.g., Friston et al., 1995). We found that both BOLD and IRON data could be fit very well using the same two temporal components, and the relative magnitudes in each case made good sense in terms of the expected contribution of

arterials (fast component) and post-arterials (slow component). BOLD signal is dominated by the fast component, but IRON is dominated by the slow component, which accounts for 80% of the IRON response in block designs, and 40% of the BOLD response.

The slowness of the IRON method of contrast was the beginning point to chapter 3. Having found that the injection of an exogenous contrast agent provided a three-fold increase in sensitivity for a block design, but only 1.5 for fixed event-related (ER) designs, made us ask whether we could optimize the IRON response to rapid event-related designs, such that the longer duration of these responses with respect to BOLD responses would not penalize the use of IRON contrast. Because randomized event-related designs were known to increase estimation efficiency for BOLD fMRI (Burock et al., 1998), we hypothesized that due to its inherently slower impulse response function (IRF), the IRON method will benefit more from randomization of the interstimulus intervals (ISI) than the BOLD method, in terms of detection efficiency. In order to confirm this hypothesis, different ER designs were considered in terms of the distribution of ISIs: fixed, random, semi-random. We found that semi-random distributions of ISIs led to the most efficient designs in terms of detection sensitivity, without significantly increasing the predictability of the design, which we measured based on a metric of the entropy of a discrete distribution.

Chapter 4 switched the focus to space: we now tried to determine the ultimate spatial resolution of BOLD and IRON fMRI. We knew, from the work that led to chapter 2, that apparent spatial specificity was enhanced with IRON contrast. That is, activation maps obtained after the injection of an optimized dose of MION contrast agent did not show activation in draining veins or draining tissue, in contrast with very large "false" activations detected in these regions with BOLD contrast. The next obvious question was what would happen at the level of small vessels and capillaries for discrete and subtle stimuli which would not be expected to show detectable nonlocal venous drainage. To examine this issue we used stimuli where small spots of varying diameters would alternate between black and white at a frequency optimized to elicit activation in the primary visual cortex (V1). We measured the FWHM of the "cortical point image" in V1 by extrapolating these measures to infinitesimal pixel size, in order to obtain an estimate of the point spread function (PSF) for BOLD and IRON fMRI. Additional factors could contribute to a higher effective measurement of the point spread function: finite image resolution, phase encoding blurring that is larger for IRON contrast because injection of MION markedly reduces T_2^*, blurring due to image distortions, and fixation blurring. We also looked at the activation maps obtained with BOLD and IRON contrasts in response to holes' stimuli, and found no significant differences between the two methods.

Throughout all the work that led to the chapters 2, 3 and 4, we assumed that a general linear model (GLM) including the contributions of the vascular response to a given stimuli, the time courses of the monkey's eye fixation, and a rough measure of the motion-induced distortions, captured most of the relevant dynamics, and that the contribution of mechanisms not specified in the GLM could be neglected. In chapter 5, the accuracy of this assumption is examined by looking at the structure of the residuals. Data was acquired with fixation-only, and after linearly removing the known sources of signal, the obtained residuals were Fourier transformed. The BOLD and IRON spectra were compared and the contribution of respiration and of a general component that varies inversely with the frequency assessed.

The main impediment in achieving higher spatial resolution was the presence of severe image distortions arising from monkey's body motion outside of the field of view (FOV). The body motion originated strong susceptibility gradients that caused severe magnetic field inhomogeneities, affecting the acquired images especially in the most posterior inferior region of the monkey's brain. The distortions were sometimes so severe that the true activations were completely erased, and the resultant activation maps showed only the effects of the motion. This is an urgent problem that needs to be address before better measurements of the PSF can be obtained in awake monkey, and its resolution will greatly increase the efficiency of data acquisition. In chapter 6 of this thesis, we tried to solve this problem by moving from single-shot EPI to multi-shot EPI with navigators. It will become clear in that chapter the reasons behind the failure of this approach, and what we think is the right strategy for solving this problem.

In the last chapter I summarize our experimental findings. Our main conclusions are presented and integrated with additional research that emerged during the development of this thesis, to show that IRON contrast fMRI is an excellent choice to use in awake, behaving macaque monkey fMRI at 3 Tesla. A discussion on the current limitations in achieving better spatial resolution, and on what we believe are the next steps for the measurement of the ultimate fMRI PSF conclude this thesis.

The majority of the work presented in this thesis has been published in scientific journals and/or presented in international conferences. In 2002, chapter 2 was published in NeuroImage (Leite et al., 2002a), and presented orally at the ISMRM conference (Leite et al., 2002b). Chapter 3 was also presented orally at the 2003 ISMRM conference (Leite and Mandeville, 2003), and has recently been published in NeuroImage (Leite and Mandeville, 2006a). Different aspects of Chapter 4 have been presented orally, or in poster form, at ISMRM conferences (Leite et al., 2004, 2005), and at the OHBM conference (Leite et al., 2006c). This chapter is almost ready for submission to a journal, which I hope will occur in the beginning of October. Preliminary work

leading to chapter 5 has been presented at the ISMRM conference this year (Leite et al., 2006b), but additional data are required before this work can be considered for publication.

1.2 A brief history of fMRI

The first human functional MRI experiments utilized bolus injections of an exogenous contrast agent (Belliveau et al., 1991) to detect brain activation in response to a visual stimulus. Human functional experiments using blood oxygen level dependent (BOLD) contrast followed shortly thereafter (Kwong et al., 1992; Ogawa et al., 1992). From the early 1990s to the present, the functional MRI literature has increased in a cubic relationship with the relative year of publication.

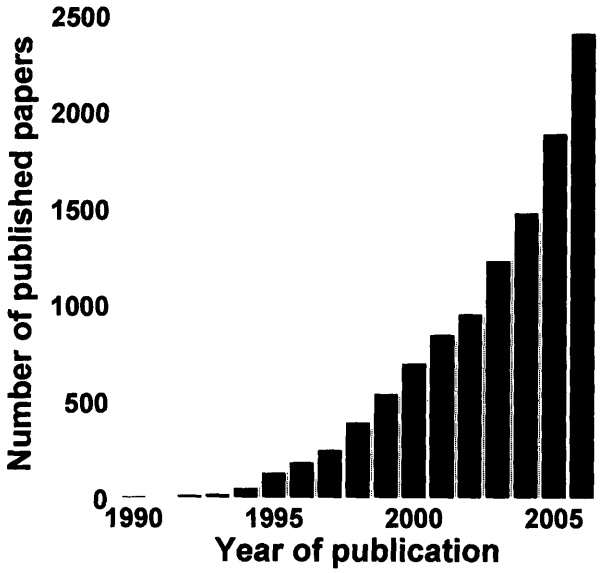

Fig. 1.1 Annual number of published papers with 'fMRI' and/or 'functional MRI' and/or 'functional magnetic resonance imaging' in the title and/or abstract. Search performed on PubMed.

Even though approximately 9 papers are published every working day, the question of how exactly fMRI activity translates into neural activity remains incompletely answered.

1.2.1 Early observations on neurophysiology

It was shown by Mosso in the 19th century (Mosso, 1881) that blood pulsations in the brain, which he monitored through a breach in the skull in terms of changes in intracranial pressure, would change in response to an outside stimulus. His conclusion that brain circulation changes selectively with neuronal activity was supported by Roy and Sherrington (Roy and Sherrington, 1890), who postulated that changes in blood flow are delicately correlated with changes in neuronal metabolism. But 6 years later, Leonard Hill, an eminent physiologist, concluded that no relationship exists between brain function and brain circulation (Hill, 1896). Twenty years later, Fulton found increased flow turbulence in occipital cortex during visual stimulation by recording

the bruit from a vascular malformation in occipital cortex (Fulton, 1928). He concluded that cortical blood flow changes according to the complexity of the visual task and the attention of the subject to that task, in agreement with Roy and Sherrington's hypothesis.

But it wasn't until 1948 that the first quantitative method for measuring whole brain blood flow and metabolism in humans was developed (Kety and Schmidt, 1948; Kety, 1951; Laudau et al., 1955). The method was based upon the uptake by the brain of a diffusible inert gas supplied by way of the arterial blood. The theory on which this method was based led to the development of current methods for the measurement of regional blood flow, metabolism, and the visualization of functional activity throughout the human brain (Ingvar and Lassen, 1962; Sokoloff, 1977). For the first time in history, it became possible to study what the different parts of the brain were doing in targeted experiments without the necessity of lesion models. Finally, in 1965, Ingvar and Risberg (Ingvar and Risberg, 1965) demonstrated directly in normal human subjects that blood flow changes regionally during changes in brain activity, definitely proving Roy and Sherrington's general hypothesis.

1.2.2 The emergence of neuroimaging technology

In 1936, Pauling and Coryell observed that changing the amount of oxygen carried by hemoglobin changes the degree to which hemoglobin disturbs a magnetic field (Pauling and Coryell, 1936). Ten years later, the physical principles of nuclear magnetic resonance (NMR) were discovered independently by Felix Bloch (Bloch, 1946) and Edward Purcell and his colleagues (Purcell et al., 1946). These principles governing the behavior of protons in a magnetic field would eventually lead to a number of magnetic resonance technologies. But it wasn't until 1973 that Paul Lauterbur expanded NMR principles to be utilized for imaging, thus introducing magnetic resonance imaging (MRI) (Lauterbur, 1973).

Also in 1973, Godfrey Hounsfield introduced X-ray computed tomography (CT) (Hounsfield, 1973), and just two years later positron emission tomography (PET) was derived from CT (Ter-Pogossian et al., 1975). It was then realized that highly accurate measurements of human brain function could be made with measurements of either blood flow or metabolism. Blood flow became the favored technique because it could be measured quickly using $H_2{}^{15}O$, allowing for many repeat measurements in the same subject.

Finally, in 1990, following on the footsteps of Pauling and Coryell and their findings on magnetic field perturbations induced by deoxyhemoglobin, Ogawa and colleagues (Ogawa et al., 1990) demonstrated that in vivo, localized changes in blood oxygenation could be detected by MRI. This MRI signal became known as the blood oxygen level dependent (BOLD) signal.

1.2.3 Metabolic and vascular "response" to neuronal activity

Blood flow generally increases in activated brain regions. Why? This is, so far, an unanswered question. But an intuitive thought is that when the neurons become active, the neuronal metabolism needs to increase in order to generate larger quantities of adenosine triphosphate (ATP), requiring increased delivery of glucose and oxygen.

While ATP can be generated by anaerobic glycolysis, this mechanism is much less efficient, in terms of quantity of ATP generated, than oxidative phosphorylation. Therefore, it was thought that while glucose consumption would probable increase by a larger amount in order to sustain both anaerobic and aerobic generation of energy, the oxygen consumption would also increase significantly, proportionally to the increase in blood flow. But surprisingly, in a seminal paper by Fox and Raichle using PET (Fox and Raichle, 1986), it was demonstrated that the cerebral metabolic rate of oxygen, or $CMRO_2$, increased only slightly in response to a stimulus, while cerebral blood flow, CBF, increased by approximately 30%. This CBF increase, out of proportion to the change in oxygen consumption, leads to the paradoxical fall of the concentration of deoxygenated hemoglobin in activated regions of the brain.

Furthermore, increases in CBF imply increases in cerebral blood volume (CBV) due to vessel compliance. The relationship between changes in flow and changes in volume was thoroughly established by Grubb, who showed that $CBV = 0.80\ CBF^{0.38}$ (Grubb et al., 1974).

In summary, in response to activation there is a large increase in CBF, and more moderate increases in CBV and $CMRO_2$.

Key issues in functional neuroimaging are still waiting for a satisfactory explanation. What are the quantitative relationships and physiological mechanisms that govern the responses of blood flow, glucose utilization, and oxygen consumption during neural activation? What function(s) serves the large increase in blood flow? Many other questions exist, but the question that first motivated this work is the following: what can we measure using functional MRI methods?

1.3 Background

1.3.1 Contrast mechanisms

The NMR signal at the receiver is proportional to the transverse magnetization,

$$S = \rho \frac{\left(1 - e^{-TR/T_1}\right) e^{-TE/T_2}}{1 - e^{-TR/T_1} \cos\alpha} \sin\alpha, \qquad (1.1)$$

where ρ is the proton density in the sample to be imaged, $R_1 = 1/T_1$ is the longitudinal relaxation rate, $R_2 = 1/T_2$ is the transverse relaxation rate, TE is the echo time, TR is the repetition time, and

α relates to the fraction of longitudinal magnetization flipped to the transverse plane. In all subsequent formulae, R_2 is used to denote either spin-echo relaxation or gradient echo relaxation (generally denoted R_2^*, which includes additional contributions due to microscopic or macroscopic non-uniformities in magnetic field, $R_2^* = R_2 + R_2'$). These relaxation rates can be manipulated to reflect the local concentration of an exogenous or endogenous contrast agent, with the following approximate form:

$$R_{1or2} = R_{1or2}^{endogenous} + R_{1or2}^{agent} \approx R_{1or2}^{endogenous} + k_{1or2}[agent]. \quad (1.2)$$

1.4.1.1 Blood Oxygen Level Dependent contrast (BOLD)

BOLD contrast uses deoxyhemoglobin as an endogenous contrast agent. Hemoglobin in the blood exists in two different forms depending upon whether it is bound to oxygen (oxyhemoglobin: HbO_2) or not (deoxyhemoglobin: dHb). These two forms have different magnetic properties: oxyhemoglobin is diamagnetic and deoxyhemoglobin is paramagnetic. For BOLD contrast, the approximate functional form above is more accurately modeled as:

$$R_2^{BOLD}(t) = kCBV^{\alpha}(t)[dHb]^{\beta}(t). \quad (1.3)$$

Monte Carlo simulations predict that R_2^{BOLD} should vary linearly with CBV ($\alpha = 1$) and slightly superlinearly with [dHb] ($\beta > 1$) at low magnetic fields like 1.5 Tesla (Boxerman et al., 1995). At high fields such as 7 Tesla, a good approximation is obtained using ($\alpha = \beta = 1$) (Boxerman et al., 1995), as assumed by Ogawa et al. (1993).

During activation, blood flow increases much more than oxygen extraction, so the concentration of deoxyhemoglobin decreases relative to the resting state, and R_2^{BOLD} decreases.

It can be shown that the BOLD signal depends on $CMRO_2$, CBF and CBV. From the hemoglobin saturation curve, $[dHb]_{blood} = (1\text{-}Y)[Hb]_{blood}$, Fick's law for oxygen flux conservation across the capillary bed, $CBF[Hb](1\text{-}Y_{venous}) = CMRO_2$, and by assuming that $Y_a = 1$, one gets

$$R_2^{BOLD}(t) = kCBV^{\alpha}(t)\left(\frac{CMRO_2(t)}{CBF(t)}\right)^{\beta}. \quad (1.4)$$

A linearized version of this equation for $\alpha = \beta = 1$, and assuming small changes during activation, is given by (Ogawa et al., 1993)

$$\Delta R_2(t) = -k[dHb]_0\left(\frac{\Delta CBF(t)}{CBF_0} - \frac{\Delta CBV(t)}{CBV_0} - \frac{\Delta CMRO_2(t)}{CMRO_{20}}\right). \quad (1.5)$$

1.4.1.2 Increased Relaxation for Optimized Neuroimaging (IRON)

Alternatively, one can perform T_2 or T_2^* fMRI using an exogenous contrast agent like MION (Monocrystalline Iron Oxide Nanoparticle). MION has a high magnetic susceptibility, remains intravascular and has a relatively long half-life (about 8 hours). Assuming that the blood concentration of MION is constant in time (steady-state), the functional form for IRON contrast will simplify to

$$R_2^{MION}(t) = kCBV(t), \tag{1.6}$$

and the relative change in CBV with activation is simply given by (Hamberg et al., 1996; Mandeville et al., 1998)

$$\frac{\Delta CBV(t)}{CBV_0} = \frac{\Delta R_2(t)}{R_2^{MION}(0)}. \tag{1.7}$$

IRON contrast was first used for fMRI in anesthetized rats (Kennan et al., 1998; Mandeville et al., 1998; van Bruggen et al., 1998), and its use was later extended to awake monkeys (Vanduffel et al., 2001).

1.4.2 Signal-to-noise ratio (SNR)

The size of the signal relative to the size of the noise is known as signal-to-noise ratio (SNR). SNR may be improved by signal averaging, as signal adds coherently and noise adds in random phase. Because the noise power is additive, the root mean square of the noise amplitude is proportional to $N^{1/2}$, where N is the number of averages. As a result, the SNR improves with $N^{1/2}$.

The thermal equilibrium magnetization for spins of gyromagnetic ratio γ and spin quantum number I in a longitudinal field B_0 is given by

$$M_0 = N_S \gamma^2 \hbar^2 I(I+1) B_0 / 3k_B T_S, \tag{1.8}$$

where N_S is the number of spins per volume and T_S the sample temperature. According to Lenz's law, which states that the emf induced in a receiver coil is proportional to the time rate of change of field within the coil, the signal amplitude will be proportional to $M_0\omega_0$ or $\gamma^3 I(I+1)B_0^2$. Therefore, the signal amplitude will increase proportionally to the square of magnetic field, the third power of the gyromagnetic ratio, and the number of spins in the volume. In summary, SNR is given by

$$SNR \sim \omega \cdot V \cdot \sqrt{T_{ACQ}} \cdot f \cdot \Psi(T_1, T_2, T_2^*), \tag{1.9}$$

where ω is the operating frequency, V is the volume of a voxel, T_{ACQ} is the k-space acquisition time, $f \leq 1$ is a function that depends on the k-space trajectory in the pulse sequence, and Ψ is a

function of T_1, T_2 and T_2^*. SNR increases proportionally to B_0 because the noise in MRI is also proportional to B_0 (Edelstein et al., 1986).

In echo planar images, the high temporal resolution is usually achieved at the expense of SNR or spatial resolution. This tradeoff is unavoidable. EPI is further limited by the T_2 of the sample, the characteristics of the imaging gradients, and other hardware considerations.

1.4.3 Sensitivity

The functional contrast-to-noise ratio depends upon both the physiology and the physics of a given technique. It can be defined generally as

$$\mathrm{fCNR} = \frac{\delta S_t}{\sigma_t} = \mathrm{fSNR}\frac{\delta S_t}{\bar{S}_t}, \tag{1.10}$$

where δS_t refers to the time-dependent signal changes, σ_t is the temporal standard deviation of the signal, $\bar{S}_t$ is the time-averaged signal, and fSNR is the functional SNR, given by $\mathrm{fSNR} = \bar{S}_t/\sigma_t$. Because some noise can be coherent, fSNR ≤ aSNR, where aSNR is the "anatomical SNR", defined in the previous section.

Fractional changes in signal are roughly proportional to absolute changes in relaxation rates, as can be seen by expanding the exponential for small changes in relaxation rate:

$$\frac{dS}{S(t)} = e^{-TE\Delta E_2(t)} - 1 \sim -TE\Delta E_2(t). \tag{1.11}$$

Using these expressions, the CNR for endogenous (BOLD) or exogenous (IRON) contrast agents can be given as (Mandeville and Marota, 1999)

$$\mathrm{CNR}_{T_2}(t) = \left(S_0 e^{-TE\,R_2^{other}}\right)\left(TE\,R_2^{agent}(0)e^{-TE\,R_2^{agent}(0)}\right)\left(\frac{\Delta R_2(t)}{R_2^{agent}(0)}\right). \tag{1.12}$$

The first term on the rhs of this equation is a scaling factor related to the baseline state, and is the same for BOLD and IRON. The second term is an amplification factor that depends upon the method and basal physiology, and it is maximized for TE R_2^{agent} (0) = 1. At common magnetic field strengths, BOLD imaging lies far below the optimal signal attenuation. For example, at 1.5 Tesla, R_2^{agent} (0) ~ 2 sec^{-1}, and for TE = 40 msec the amplification factor will be approximately equal to 20% of the maximum value. With an exogenous contrast agent one can theoretically achieve the maximum amplification simply by changing the dose of agent injected and optimizing the echo time accordingly. The third term has to do with activation and is usually of the same order of magnitude for BOLD and IRON contrasts in steady state, although results to date indicate that BOLD and IRON temporal responses differ significantly, so that CNR is a complicated function of the duration and timing of stimuli, the choice of echo time and contrast

agent dose, the magnetic field strength, and (for reasons explained below) the local blood volume fraction.

1.4.4 Spatial specificity

Another way to express CNR at a spatial location **r** and time t as (Mandeville and Marota, 1999)

$$CNR_{T_2}(\mathbf{r},t) = SNR(\mathbf{r})W(\mathbf{r})\Phi(\mathbf{r},t). \quad (1.13)$$

SNR(**r**) is the SNR at rest (before injection of the contrast agent in the case of IRON contrast), W(**r**) is a vascular weighting function, and $\Phi(\mathbf{r},t)$ depends upon the functional changes but is independent of baseline physiology.

For BOLD contrast, the vascular weighting function (assuming small changes in signal and a tight regional linear relationship between resting state values of CBF and $CMRO_2$) is given by

$$W_{BOLD}(\mathbf{r}) = kv(\mathbf{r}), \text{ with } k = TE\left\langle R_2^{BOLD}\right\rangle_{brain}. \quad (1.14)$$

For IRON contrast, the vascular weighting function is given by

$$W_{IRON}(\mathbf{r}) = v(\mathbf{r})e^{-v(\mathbf{r})}. \quad (1.15)$$

From the above expressions for the vascular weighting, one can see that BOLD linearly amplifies CNR by resting state CBV ("brain versus vein" ambiguity). Intuitively, this occurs because the BOLD effect is so weak that it produces no regional dependence on SNR (to first order), so CNR is driven by fractional signal changes, which scale linearly with the resting state blood volume fraction. Conversely, the IRON method is much less sensitive to resting CBV when an appropriate dose of contrast agent is used to produce an optimal tradeoff between SNR and fractional signal changes. Regions with a high blood volume fraction will have large fractional signal changes but small basal SNR, whereas lower blood volume areas will have smaller fractional signal changes but higher SNR. In fact, the dose of contrast agent can be selected to target a specific tissue blood volume fraction, so that the maximum sensitivity occurs for blood volume fractions that correspond to regions without significant large vessel contributions.

1.4.5 Linearity

We often assume that the vascular system is a time-invariant linear system (e.g., Friston et al., 1995) that is, the output of this system, the vascular response, is given by the convolution of the neuronal input with the system impulse response function. We further assume that the neuronal system follows the stimulus time course in a linear manner, such that the vascular response can be predicted by convolution of the vascular impulse response function with the timing diagram of the stimulus design.

The linear model appears to be a good first-order approximation to relate brain function to BOLD and IRON contrasts. It has been shown that BOLD signal changes in the visual cortex scale roughly linearly with stimulus contrast and duration (Boynton et al., 1996) and there is good evidence of near-linear additivity of responses to successive, brief stimuli presented at rates up to one every two seconds (Dale and Buckner, 1997). Nonetheless, nonlinearities have been observed as a function of the magnitude and duration of sustained stimulations (Vasquez and Noll, 1998), and at rapid rates of brief stimulation (Friston et al., 1998). These nonlinearities may reflect saturation of the BOLD signal, neural transients or habituation of neural activity, or a combination of factors.

Linearity is a powerful assumption that not only greatly simplifies data analysis but also provides useful insights into the relationship between neural activity and related vascular changes.

1.4.6 Temporal response

In general, the BOLD response to a stimulus shows two distinct phases: the main positive BOLD response conventionally used in fMRI experiments, followed by a post-stimulus undershoot. An initial dip occurring before the positive response has proven elusive to detect (Buxton, 2001). During prolonged stimulation, BOLD signal and CBF generally reach plateau values after 5 – 6 sec (DeYoe et al., 1994). The post-stimulus undershoot is not present in the CBF signal, or at least not with sufficient magnitude to explain the size of the BOLD post-stimulus undershoot. A common view of the post-stimulus undershoot is that it is caused by a delayed return of CBV to baseline (Mandeville et al., 1998). In fact, experimental results in anesthetized rodent models have shown that the CBV response contains a component that evolves slowly during and after a stimulus, causing a mismatch between blood flow and blood volume with the proper amplitude and time course to explain the BOLD post-stimulus undershoot (Mandeville et al., 1998, 1999; Mandeville and Marota, 1999).

Even though the BOLD temporal impulse response function is slow compared with the underlying neural response, rapid stimulus designs have been developed that allow exploration of many cognitive processes, by increasing the available temporal resolution. These designs are called event-related designs (ERD), and generally consist of rapidly presented interleaved trials of multiple event types of short duration. For periodic ER designs, an optimum interstimulus interval (ISI) exists below which detection power and estimation efficiency greatly decrease with ISI (Dale, 1999; Bandettini and Cox, 2000). Burock and colleagues found that an overall increase

in BOLD detection activity per unit time could be achieved by randomization of the ISIs (Burock et al., 1998).

1.4.7 Spatial resolution

The SNR provides the fundamental limitation to the spatial resolution in magnetic resonance since the signal available from each volume element decreases as the voxel size is reduced. Because SNR can be increased by averaging only as the square root of time, the required averaging time for a target SNR scales in proportion to the linear dimension of a voxel to the sixth power. Other factors limiting the achievable spatial resolution in EPI include T_2^* relaxation, spin diffusion, and image distortions.

The contribution of the relaxation linewidth will be insignificant if the bandwidth is sufficiently large that the T_2^* broadening is less than one pixel.

Diffusion of spins in the presence of a magnetic field gradient results in magnetization dephasing. As a consequence, diffusion can cause signal attenuation and additional linewidth broadening. For typical imaging times the Brownian motion will set the resolution to a maximum of 10 μm, but in living subjects this limit is at least one order of magnitude higher due to bulk motion and brain pulsation.

Complex local distortions have the effect of inducing artifacts in the image and this leads to an inevitable resolution loss. In addition, the diffusional motion of spins across regions of variable susceptibility causes additional transverse relaxation and consequential signal attenuation. These effects associated with susceptibility inhomogeneity will increase as B_0, increases.

Additionally, the spatial characteristics of the vasculature in each brain area, will further limit the maximum achievable resolution.

The maximum fMRI spatial resolution is still unknown. In the years leading to the work presented in this thesis, many groups had reported columnar resolution using different fMRI techniques in different preparations (Menon et al., 1997; Menon et al., 1999; Duong et al., 2000; Kim et al., 2000; Duong et al., 2001; Cheng et al., 2001), but it is unclear how to evaluate most of these studies. Lacking any anatomical reference, these studies identify voxels according to the size of the signal change associated with a condition, and then claim that the pattern is "patchy" (Kim et al., 2000) or otherwise suggestive of columnar features. Several of these studies (Duong et al., 2000; Kim et al., 2000) employed the BOLD "initial dip"; as noted previously, the existence of this effect is still controversial, let alone the robustness of this method for high resolution functional mapping. Cheng and colleagues used the regular BOLD signal to achieve an

in-plane resolution of 0.47 mm in visual cortex, detecting optical dominance columns (ODC) of approximately 1 mm width. Despite claims from the MRI and optical community that BOLD signal does not have the resolution to identify columns, only the BOLD study of Cheng et al. (2001) demonstrated reproducibility of the functional pattern within a session.

1.5 References

Bandettini PA, Cox RW, 2000. Event-related fMRI contrast when using constant interstimulus interval: theory and experiment. Magn Reson Med 43(4): 540-8.

Belliveau JW, Kennedy DN Jr, McKinstry RC, Buchbinder BR, Weisskoff RM, Cohen MS, Vevea JM, Brady TJ, Rosen BR, 1991. Functional mapping of the human visual cortex by magnetic resonance imaging. Science 254(5032): 716-9.

Bloch F, 1946. Nuclear induction. Physiology Review 70: 460-474.

Boxerman JL, Hamberg LM, Rosen BR, Weisskoff RM, 1995. MR contrast due to intravascular magnetic susceptibility perturbations. Magn Reson Med 34(4): 555-566.

Boynton GM, Engel SA, Glover GH, Heeger DJ, 1996. Linear systems analysis of functional magnetic resonance imaging in human V1. J Neurosci 16: 4207-4221.

Burock MA, Buckner RL, Woldorff MG, Rosen BR, Dale AM, 1998. Randomized event-related experimental designs allow for extremely rapid presentation rates using functional MRI. Neuroreport 9(16): 3735-9.

Buxton RB, 2001. The elusive initial dip. Neuroimage 13(6 Pt 1): 953-8.

Cheng K, Waggoner RA, Tanaka K, 2001. Human ocular dominance columns as revealed by high-field functional magnetic resonance imaging. Neuron 32(2): 359-74.

Dale AM, Buckner RL, 1997. Selective averaging of rapidly presented individual trials using fMRI. Hum Brain Mapp 5: 329-40.

Dale AM, 1999. Optimal experimental design for event-related fMRI. Hum Brain Mapp 8(2-3): 109-14.

DeYoe EA, Bandettini P, Neitz J, Miller D, Winans P, 1994. Functional magnetic resonance imaging (FMRI) of the human brain. J Neurosci Methods 54(2): 171-87. Review.

Duong TQ, Kim DS, Ugurbil K, Kim SG, 2000. Spatiotemporal dynamics of the BOLD fMRI signals: toward mapping submillimeter cortical columns using the early negative response. Magn Reson Med 44(2): 231-42.

Duong TQ, Kim DS, Ugurbil K, Kim SG, 2001. Localized cerebral blood flow response at submillimeter columnar resolution. Proc Natl Acad Sci U S A 98(19): 10904-9.

Edelstein WA, Glover GH, Hardy CJ, Redington RW, 1986. The intrinsic signal-to-noise ratio in NMR imaging. Magn Reson Med 3(4): 604-18.

Fox PT, Raichle ME, 1986. Focal physiological uncoupling of cerebral blood flow and oxidative metabolism flow and oxidative metabolism during somatosensory stimulation in human subjects. Proc Natl Acad Sci U S A 83(4): 1140-1144.

Friston KJ, Holmes AP, Worsley KJ, Poline JP, Frith CD, Frackowiak RSJ, 1995. Statistical Parametric Maps in Functional Imaging: A General Linear Approach. Hum Brain Mapp 2: 189-210.

Friston KJ, Josephs O, Rees G, Turner R, 1998. Nonlinear event-related responses in fMRI. Magn Reson Med 39(1): 41-52.

Fulton JF, 1928. Observations upon the vascularity of the human occipital lobe during visual activity. Brain 51: 310-320.

Grubb RL Jr, Raichle ME, Eichling JO, Ter-Pogossian MM, 1974. The effects of changes in PaCO2 on cerebral blood volume, blood flow, and vascular mean transit time. Stroke 5(5): 630-9.

Hamberg LM, Boccalini P, Stranjalis G, Hunter GJ, Huang Z, Halpern E, Weisskoff RM, Moskowitz MA, Rosen BR, 1996. Continuous assessment of relative cerebral blood volume in transient ischemia using steady state susceptibility-contrast MRI. Magn Reson Med 35(2): 168-73.

Hill L, 1896. The physiology and pathology of the cerebral circulation: an experimental research. London: J & A Churchill.

Hounsfield GN, 1973. Computerized transverse axial scanning (tomography): Part I. Description of system. British J Radiol 46: 1016-1022.

Ingvar DH, Lassen NA, 1962. Regional blood flow of the cerebral cortex determined by Krypton85 Acta Physiol: Scand. 54: 325-88.

Ingvar DH, Risberg J, 1965. Influence of mental activity upon regional cerebral blood flow in man. A preliminary study. Acta Neurol Scand Suppl 14: 183-6.

Kennan RP, Scanley BE, Innis RB, Gore JC, 1998. Physiological basis for BOLD MR signal changes due to neuronal stimulation: separation of blood volume and magnetic susceptibility effects. Magn Reson Med 40: 840-846.

Kety SS, Schmidt CF, 1948. The nitrous oxide method for the quantitative determination of cerebral blood flow in man: theory, procedure and normal values. J Clin Invest 27(4): 476-83.

Kety SS, 1951. The theory and applications of the exchange of inert gas at the lungs and tissues. Pharmacol Rev 3: 1-14.

Kim DS, Duong TQ, Kim SG, 2000. High-resolution mapping of iso-orientation columns by fMRI. Nat Neurosci 3(2): 164-9.

Kwong KK, Belliveau JW, Chesler DA, Goldberg IE, Weisskoff RM, Poncelet BP, Kennedy DN, Hoppel BE, Cohen MS, Turner R, et al., 1992. Dynamic magnetic resonance imaging of human brain activity during primary sensory stimulation. Proc Natl Acad Sci U S A 89(12): 5675-9.

Landau WM, Freygang WH, Rowland LP, Sokoioff L, Kety SS, 1955. The local circulation of the living brain; values in the unanesthetized and anesthetized cat. Trans Amer Neurol Assn 80: 125-9.

Lauterbur P, 1973. Image formation by induced local interactions: Examples employing nuclear magnetic resonance. Nature 242: 190-191.

Leite FP, Tsao D, Vanduffel W, Fize D, Wald L, Dale A, Kwong K, Orban GA, Rosen BR, Tootell RB, Mandeville JB, 2002a. Repeated fMRI using Iron Oxide Contrast Agent in Awake, Behaving Macaques at 3 Tesla. NeuroImage 16(2): 283-94.

Leite FP, Tsao D, Vanduffel W, Fize D, Wald L, Dale A, Kwong K, Orban GA, Rosen BR, Tootell RB, Mandeville JB, 2002b. Spatio–Temporal Analysis of BOLD and CBV fMRI in Awake, Behaving Macaques at 3 Tesla. Proceedings of the 10th ISMRM Meeting.

Leite FP, Mandeville JB, 2003. Event-Related BOLD vs IRON. Proceedings of the 11th ISMRM Meeting.

Leite FP, Vanduffel W, Tootell RB, Mandeville JB, 2004. Point-Image fMRI Experiments in Awake, Behaving Macaques Proceedings of the 12th ISMRM Meeting.

Leite FP, Vanduffel W, Rosen BR, Mandeville JB, 2005. Comparing Spatial Resolution of IRON and BOLD in Awake Macaques. Proceedings of the 13th ISMRM Meeting.

Leite FP, Mandeville JB, 2006a. Characterization of Event-related Designs using BOLD and IRON fMRI. NeuroImage 29(3): 901-9.

Leite FP, Greve D, Vanduffel W, Mandeville JB, 2006b. Temporal Autocorrelation of Noise for BOLD and IRON fMRI. Proceedings of the 14th ISMRM Meeting.

Leite FP, Vanduffel W, Tootell RB, Rosen BR, Mandeville JB, 2006c. Point-Image fMRI Experiments in Awake, Behaving Macaque Monkeys. Proceedings of the 12th Annual Meeting of the Organization of Human Brain Mapping.

Mandeville JB, Marota JJ, Kosofsky BE, Keltner JR, Weissleder R, Rosen BR, Weisskoff RM, 1998. Dynamic functional imaging of relative cerebral blood volume during rat forepaw stimulation. Magn Reson Med 39(4): 615-24.

Mandeville JB, Marota JJA, Ayata C, Zaharchuk G, Moskowitz MA, Rosen BR, Weisskoff RM, 1999. Evidence of a Cerebrovascular Post-arteriole Windkessel with Delayed Compliance. J Cereb Blood Flow Metab 19: 679-689.

Mandeville JB, Marota JJ, 1999. Vascular filters of functional MRI: spatial localization using BOLD and CBV contrast. Magn Reson Med 42(3): 591-8.

Menon RS, Ogawa S, Strupp JP, Ugurbil K, 1997. Ocular dominance in human V1 demonstrated by functional magnetic resonance imaging. J Neurophysiol 77(5): 2780-7.

Menon RS, Goodyear BG, 1999. Submillimeter functional localization in human striate cortex using BOLD contrast at 4 Tesla: implications for the vascular point-spread function. Magn Reson Med 41(2): 230-5.

Mosso A, 1881. Ueber den Kreislauf des Blutes im Menschlichen Gehirn. Leipzig: Verlag von Veit & Co.

Ogawa S, Lee TM, Kay AR, Tank DW, 1990. Brain magnetic resonance imaging with contrast dependent on blood oxygenation. Proc Natl Acad Sci U S A 87: 9868-9872.

Ogawa S, Tank DW, Menon R, Ellermann JM, Kim SG, Merkle H, Ugurbil K, 1992. Intrinsic signal changes accompanying sensory stimulation: functional brain mapping with magnetic resonance imaging. Proc Natl Acad Sci U S A 89(13): 5951-5.

Ogawa S, Lee TM, Barrere B, 1993. The sensitivity of magnetic resonance image signals of a rat brain to changes in the cerebral venous blood oxygenation. Magn Reson Med 29(2): 205-10.

Pauling, L and Coryell CD, 1936. The magnetic properties and structure of hemoglobin, oxyhemoglobin and carbonmonoxyhemoglobin. Proc Natl Acad Sci U S A 22: 210-216.

Purcell EM, Torry HC, Pound RV, 1946. Resonance absorption by nuclear magnetic moments in a solid. Physiological Review 69, 37.

Roy CS, Sherrington CS, 1890. On the regulation of the blood-supply of the brain. J Physiol 11: 85-108.

Sokoloff L, 1977. Relation between physiological function and energy metabolism in the central nervous system. J Neurochemistry 29: 13-26.

Ter-Pogossian MM, Phelps ME, Hoffman EJ, Mullani NA, 1975. A positron-emission tomography for nuclear emission tomography for nuclear imaging (PET). Radiology 114: 89-98.

van Bruggen N, Busch E, Palmer JT, Williams SP, de Crespigny AJ, 1998. High-resolution functional magnetic resonance imaging of the rat brain: mapping changes in cerebral blood volume using iron oxide contrast media. J Cereb Blood Flow Metab 18: 1178-83.

Vanduffel W, Fize D, Mandeville JB, Nelissen K, Van Hecke P, Rosen BR, Tootell RBH, Orban GA, 2001. Visual Motion Processing Investigated using Contrast-enhanced fMRI in Awake Behaving Monkeys. Neuron 32(4): 565-77.

Vazquez AL, Noll DC, 1998. Nonlinear aspects of the BOLD response in functional MRI. Neuroimage 7(2): 108-18.

Chapter 2

Spatio-Temporal Characteristics of IRON and BOLD fMRI

2.0 Preface

Prior to our series of studies, the IRON method had been employed for fMRI in anesthetized rodents, and this technique demonstrated an increase in CNR relative to BOLD fMRI in these models (Kennan et al., 1998; Mandeville et al., 1998), as well as a slower temporal response (Mandeville et al., 1998, 1999). There are numerous reasons to want to repeat, and to extend, these measurement in an awake primate model. Firstly, all anesthetics increase basal blood oxygenation by decreasing $CMRO_2$ more than CBF; thus, BOLD sensitivity is compromised in the anesthetized state due to a decreased basal concentration of deoxygenated hemoglobin. Hence, it is important to quantify the increase in detection power provided by the IRON method in an awake animal model. Secondly, there are instances in the literature – the BOLD "initial dip" is a prominent example – where inconsistencies in results are attributed to differences in species or anesthetic condition. Thirdly, stimulus paradigms employed in this chapter and in the next chapter could be hard to replicate using electrical stimuli in anesthetized rodents. Studies in those models found that responses were not stationary (repeatable) without long inter-stimulus intervals. Moreover, retinotopic projections of point stimuli as reported in Chapter 4 have not been reported in anesthetized animals.

Just prior to our publication of these results, two studies reported results in awake primates using exogenous contrast agent. The first report was a "quick and dirty" publication that essentially demonstrated that signal changes could be detected using an exogenous contrast agent (Dubowitz et al., 1998). This publication provided no useful information about CNR or temporal response for IRON fMRI, and this group has only published one subsequent fMRI study in awake primates. The second study (Vanduffel et al., 2001) was performed in collaboration with our laboratory. While robust fMRI results were obtained using the IRON method in these studies at 1.5 Tesla, meaningful comparisons with BOLD signal were prevented by the poor quality of BOLD results at this field strength. For this group using a 1.5 Tesla scanner, the use of exogenous agent was the "make or break" factor that enabled their studies.

With the aid of Wim Vanduffel, who has relocated to our laboratory, we embarked on a series of studies to compare the detection power, temporal profile, and gross spatial localization of responses to visual stimuli applied to the awake, behaving non-human primate.

2.1 Introduction

The awake, behaving macaque is an important model of the human brain for neuroscience, physiology, and the development of neuroimaging methodologies. The use of alert animals expands the range of experimental paradigms, and such studies eliminate the significant complications and uncertain interpretation associated with anesthesia. Results obtained in awake non-human primates also require less extrapolation to studies of the alert human brain, and to the extensive literature on the organization of macaque brain that has been derived from invasive methods. As a complimentary non-invasive imaging tool, fMRI serves as a powerful whole-brain survey technique that can be performed repeatedly in individual animals.

Functional MRI based on blood oxygen level depend (BOLD) signal has become a routine tool of human neuroscience, and several groups have previously reported fMRI results in anesthetized or awake non-human primates using BOLD contrast (Stefanacci et al., 1998; Dubowitz et al., 1998; Logothetis et al., 1999; Hayashi et al., 1999; Disbrow et al., 2000; Logothetis et al., 2001; Vanduffel et al., 2001). However, the low sensitivity of the BOLD method at common magnetic field strengths presents a challenge for the detection of subtle changes in local perfusion, and sensitivity is one factor that limits high spatial resolution.

In animal models, exogenous MRI contrast agents with long blood half lives provide an attractive alternative to BOLD signal. In particular, dextran-coated iron oxide agents (Weissleder et al., 1990; Josephson et al., 1990) have found utility in a wide variety of animal research, and are now are being tested in human clinical trials (Sharma et al., 1999; Taylor et al., 1999; Enochs et al., 1999). For functional brain mapping in anesthetized rodents, these agents have demonstrated significant advantages over BOLD signal in terms of functional sensitivity at 2 and 4.7 Tesla (Mandeville et al., 1998; Kennan et al., 1998; van Bruggen et al., 1998; Chen et al., 2001). Furthermore, such contrast agent studies are uniquely suited for spatial-temporal comparisons of the physiology of cerebral blood volume (CBV) in relation to BOLD signal, which depends upon blood volume, blood flow, and oxygen utilization. Rodent studies using electrical forepaw stimulation have shown that the temporal evolution of CBV differs markedly from BOLD signal (Mandeville et al., 1998) and cerebral blood flow (Mandeville et al., 1999b).

Due to the difficulties of obtaining robust BOLD responses in the presence of motion artifacts in awake primates, as described by others (Stefanacci et al., 1998; Logothetis et al., 1999), two

recent studies have explored the viability of contrast agents for fMRI studies in alert primates. Dubowitz et al. (2001) found that a low dose of an iron oxide agent enabled a modest improvement in functional sensitivity relative to BOLD signal at 1.5 Tesla. Vanduffel et. al. (Vanduffel et al., 2000; Mandeville et al., 2001b; Vanduffel et al., 2001) demonstrated that contrast agent enabled a robust mapping of motion-sensitive regions throughout visual cortex at this same field strength, and that this method provided better sensitivity and apparent localization than BOLD signal.

We report results from a series of experiments in awake, behaving macaques using repeated injections of iron oxide contrast agent at doses that are effective for functional brain imaging. We characterized the temporal relationship of functional signals weighted by deoxyhemoglobin and blood volume using a variety of stimulus designs, and we compared the functional sensitivity of contrast-enhanced fMRI in relation to BOLD signal at 3 Tesla for short, prolonged, and rapidly presented stimuli. These results, and the macaques' apparent tolerance of repeated injections of iron oxide, show that this method is both viable and highly advantageous for functional brain imaging in awake primates.

2.2 Methods

2.2.1 Animal model

All experiments were performed at the Massachusetts General Hospital according to NIH and European animal care guidelines, following the general procedures as employed at a different laboratory (Vanduffel et al., 2001). Briefly, plastic headsets were surgically implanted onto the skulls of two male rhesus monkeys (monkeys "M-A" and "M-B", 2.5-3 kg) during anesthesia. Operations were performed under isoflurane (1.5%) / N_2O (50%) / O_2 (50%). Antibiotics (50 mg/kg i.m., Kefzol, Lilly, Brussels) and analgesics (4 mg/kg i.m. Dolzam, Zambon, Brussels) were given daily for 3-7 days following each surgery.

After recovery, monkeys were adapted to physical head restraint while seated on their haunches in the "sphinx" position inside a plastic box. Animals were trained to perform a high acuity fixation task while visual stimuli were presented in the background. When a small vertical fixation bar (5 x 18 min arc) switched to a horizonal orientation, a monkey could obtain a reward of apple juice by quickly placing a hand to interrupt a light path. Incorrect responses were penalized by a delay before presentation of the next horizontal bar. All responses were recorded and monitored on-line to determine performance accuracy and the monkeys' willingness to continue. Despite the fact that the monkeys' response scores were consistently high, direct eye

monitoring showed repeated saccades from the fixation point, so retinotopic activation patterns presumably contain some contamination from spurious eye movement.

For all studies that employed the monocrystalline iron oxide nanoparticle (MION) contrast agent, the MION solution was injected into the femoral vein below the knee just prior to each scanning session; no additional MION was added during the duration of a scan. MION was synthesized at the Massachusetts General Hospital (Weissleder et al., 1990; Shen et al., 1993) and is widely distributed throughout the MRI community. MION was injected in the original production buffer of sodium citrate without saline dilution. An iron dose of 8-10 mg/kg was injected in a volume of 1.8-2 ml using a MION solution with a concentration of 11.92 mg iron per ml.

2.2.2 Visual Stimulation

Visual stimuli were projected from an LCD projector (Sharp model XG-NV6XU) onto a screen which was positioned 29.5 cm in front of the monkey's eyes. The visual stimulus was a pinwheel checkerboard in which black and white segments were alternated at 8 Hz. This stimulus, with a mean luminance of 1795 cd/m^2, was compared to a baseline condition of a spatially uniform gray screen with a luminance of 12 cd/m^2. The stimulus covered a visual field of 37 x 48 degrees, and the fixation bar (0.8 x 0.2 degrees) was presented at the center of the visual field at all times.

Four stimulus paradigms, each lasting 4.5 minutes, were employed. Each paradigm included 30 seconds of baseline at the beginning of the run, and then used the following timing during the remaining four minutes: 1) 2 cycles of 60 sec of stimulus followed by 60 sec of baseline, 2) 4 cycles of 4 sec of stimulus followed by 56 sec of baseline, 3) 8 cycles of 4 sec of stimulus followed by 26 sec of baseline, and 4) 16 cycles of 4 sec of stimulus followed by 8 sec of baseline, with an additional 48 sec of baseline at the end.

For the 60 sec stimulus paradigm, we acquired 22 BOLD runs in 3 sessions and 11 MION runs in 2 sessions for monkey M-A. For monkey M-B, we acquired 34 BOLD runs in 7 sessions and 16 MION runs in 3 sessions. Runs with different stimulus paradigms were cycled during each session, so the numbers of runs were similar for the other paradigms. Scanning sessions typically lasted 3 hours.

2.2.3 Magnetic Resonance Imaging

Experiments were performed in a 3 Tesla Siemens Allegra scanner (Siemens Medical System, Erlangen, Germany) using a custom surface coil for radio frequency excitation and reception of signal. All functional imaging employed single shot multislice echo planar imaging

with an isotropic resolution of 1.5 mm. 20 slices were acquired using a repetition time of 2 sec and a 90 degree flip angle for the visual paradigm that alternated 60 sec of stimulus with 60 sec of baseline. For all other visual paradigms, 4 slices through primary visual cortex were acquired using a repetition time of 500 msec and a flip angle of 45 degrees. All BOLD studies employed a gradient echo time of 30 ms, and all MION studies used a gradient echo time of 20 msec (the minimum achievable value for the selected resolution and sequence).

In addition to functional imaging, T_1-weighted EPI images were acquired in each session in order to facilitate registration of brains across magnet sessions by improving the anatomical detail relative to BOLD images. Additionally, data was acquired in each session to enable the calculation of T_2^* maps by obtaining 9 gradient echo times from 20 to 60 msec at 5 msec intervals. This data was collected at the beginning of each BOLD session, and at both the beginning and end of each MION session.

2.2.4 Data Analysis

Despite physical fixation of the monkeys' heads in the restraint device, apparent brain motion and small distortions resulted from changes in the magnetic field associated with body motion. Therefore, motion correction was applied to all data sets using the Analysis of Functional NeuroImages (AFNI) motion correction algorithm (Cox and Hyde, 1997). For each animal, all images acquired in all sessions were then registered into a common space in order to enable spatio-temporal comparisons of BOLD and MION signals, and to enable comparison of T_2^* and R_2^* ($1/ T_2^*$) maps between BOLD and MION sessions. In order to minimize imperfections in registration, all data were spatially smoothed after registration using an isotropic gaussian filter with a full width at half maximum of 3 mm.

R_2^* and T_2^* maps were computed from the multi-echo data assuming monoexponential relaxation of MRI signal: $S(TE) = S(0) \exp(-TE/T_2^*)$. The blood iron concentration was monitored through the transverse relaxation rate due to MION in the blood: $R_2^{*MION} = R_2^* - \overline{R_2^{*BOLD}}$, where R_2^* is the relaxation rate determined from the multi-echo data and the BOLD relaxation rate refers to the average value of the total relaxation rate across BOLD sessions at each voxel. The iron blood half life ($T_{1/2}$) was then estimated from a monoexponential decay function across the duration of each experiment: $R_2^{*MION}(t) = R_2^{*MION}(0) \exp(-0.69\, t / T_{1/2})$.

When averaging MION signal changes across sessions, it is necessary in principle to account for the different blood concentrations of iron oxide. One way to properly account for inter-session effects of dose is to convert signal to percent CBV change, as done in rodent experiments when contrast agent is injected inside the magnet (e.g., Mandeville et al., 1998). Because contrast agent

was injected outside the magnet in these experiments for logistical reasons, we used a global normalization factor for each session to generate a corrected change in transverse relaxation rate: $\Delta R_2^{*CORR}(t) = \{R_2^{*MION,AVERAGE}/R_2^{*MION,SESSION}\}\Delta R_2^{*SESSION}(t)$, where the relaxation rates were determined across a large brain volume during each session as described above, and the average relaxation rate is the average across sessions. Relative to voxel-wise calculations of percent changes in CBV, the global correction is less susceptible to inter-session differences in the magnetic field shim and imperfections in cross-session alignment. Nevertheless, percent CBV calculations can be expected to be accurate across relatively large regions of interest, as used for the generation of our time course figures.

Analysis of functional data employed general linear model methods (Friston et al., 1995; Boynton et al., 1996), in which a hemodynamic impulse response function (IRF) is convolved with the stimulus paradigm to generate a maximum likelihood estimation of the stimulus-linked vascular response. We determined separate BOLD and MION IRFs from a region of interest analysis applied to each of the respective data sets. To characterize the temporal response, a 1 cm^3 region of interest was selected from primary visual cortex using the registered data sets. In each case, the IRF for subsequent analysis was assembled from a series of exponential basis functions, $h(t) = \sum_k {a_k}/{\tau_k} \exp(-t/\tau_k)$. In this basis, convolution with a step function generates a hemodynamic response $H(t) = \sum_k a_k (1 - \exp(-t/\tau_k))$ following stimulus onset, and $H(t) = \sum_k a_k \exp(-t/\tau_k)$ following stimulus cessation. Thus, this formulation provides flexibility and the advantage of simplicity, in that the dominant low frequency time constants can be measured directly from the data. The amplitudes of the basis functions for each IRF were fit within the general linear model after inclusion of a constant term and a linear drift. The data for all four stimulation paradigms were fit simultaneously in order to provide an optimal estimate of the IRF.

After describing the temporal response, the statistical power of the BOLD and MION methods were measured using standard linear model methods (Friston et al., 1995) and the IRFs as determined from the region of interest analyses. Specifically, if N data points (**d**) as a function of time (t) are a simple linear summation of n basis functions (**B**) times parameters (**P**) within a given error (**e**), $d_t = \sum_n B_{tj} P_j + e_t$, then the contrast-to-noise ratio (CNR) for a simple two-state comparison can be calculated as a T-statistic: $T = \frac{P_1}{\left[{\sigma^2}/{N_F} C_{1,1} \right]^{1/2}}$. In this equation, **C** is

the covariance matrix, $\mathbf{C} = (\mathbf{B}^T\mathbf{B})^{-1}$, N_F is the number of degrees of freedom (N-n), and the stimulus reference vector is the first basis function corresponding to parameter P_1. The variance is calculated between the data and the fit as $\sigma^2 = \sum_N \left(d_t - \sum_n B_{tj}P_j\right)^2$, including basis functions describing the stimulus response, mean value of signal, and signal drift (slope).

Because the number of runs for each stimulus paradigm and MRI contrast type varied across sessions, we compared statistical scores by creating maps of the average values and standard errors of T-scores across all runs and all sessions in each animal.

2.3 Results

2.3.1 Transverse relaxation rates and MION blood half life

Within large brain volumes in monkeys M-A and M-B that were selected to avoid susceptibility artifacts, the average R_2^* value (mean ± SEM) prior to injection of MION was 20.9 ± 0.2 sec^{-1} (T_2^* = 48 msec). However, numerous regions around the edge of the brain exhibited T_2^* values less than 20 msec. An echo time of 30 msec was selected for BOLD experiments as a compromise between functional sensitivity and susceptibility artifacts across the brain. Because adequate sensitivity can be obtained at any echo time by adjusting the dose of iron oxide agent, MION experiments employed the minimum obtainable echo time of 20 msec for our EPI sequence and resolution.

Using the average value of the relaxation rate in BOLD experiments as a reference value for zero dose of contrast agent, the mean change in relaxation rate due to the presence of MION was 24.1 ± 0.6 sec^{-1} across the brain at the beginning of these experiments. During experiments lasting 2.9 ± 0.3 hours, the average value of the MION-induced relaxation rate was 21.1 ± 1.1 sec-1, and the calculated MION blood half life was 8.4 ± 1.4 hours.

2.3.2 Response Scores

Monkeys attended to the fixation cue and responded when the cue switched to a horizontal position. Monkey M-A correctly responded to 92 ± 10% (mean ± standard deviation) of the cues during BOLD experiments, and 85 ± 5% of the cues during MION experiments. Monkey M-B correctly responded to 89 ± 13% and 92 ± 5% of the cues during BOLD and MION experiments, respectively. The average duration of all BOLD sessions was 2.2 ± 0.4 hours, and the average duration of MION sessions was 2.9 ± 0.7 hours. Neither session duration nor response scores were significantly different ($p > 0.05$) between BOLD and MION sessions.

2.3.3 Temporal Response

Fig. 2.1a shows the shapes of the BOLD and MION responses due to a sustained stimulus after averaging across both animals and all magnet sessions. Error bars in all figures represent standard errors of the mean across scanning sessions. The curves in the figure are single exponential fits to the data using one time constant for both the rise and decay of signal. A single exponential time constant of 13.5 sec provided a good description of the low frequency MION response. A time constant of 4.5 sec adequately described the low frequency BOLD response, except for the post-stimulus region, which showed an undershoot with a time constant similar to the MION response. In order to better describe the post-stimulus undershoot, the exponential basis for the BOLD IRF included both the 4.5 and 13.5 sec time constants. Because the single MION time constant did not provide a good description of briefly presented stimuli, and because changes in blood volume can be expected to contain an arterial time constant that is similar to the measured BOLD value, both the 4.5 and 13.5 sec time constants were also included in the exponential basis for the MION IRF.

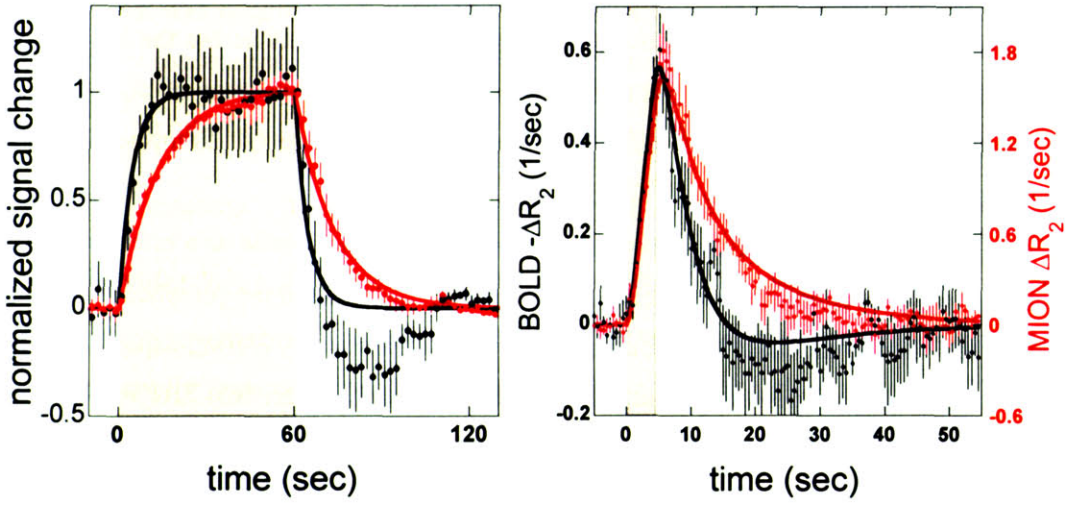

Fig. 2.1a) Normalized BOLD (black) and MION (red, reversed sign) signal changes as a function of time due to 60 sec of visual stimulation (gray shaded interval). The lines are monexponential fits to the data using time constants of 4.5 sec (BOLD) and 13.5 sec (MION). b) Measured impulse response functions for BOLD (black) and MION (red, reversed sign) signal using a 4 sec stimulus (gray shaded interval). Solid lines indicate the linear model estimation of the response obtained by simultaneously fitting all stimulation paradigms, using the dominant time constants determined from prolonged stimulation (a).

When only 2 time constants were used to fit each IRF, a delay was required between the onset of a stimulus and the onset of the hemodynamic response in order to describe the rapidly sampled data with TR = 500 msec. In the exponential basis {4.5, 13.5} using a 1.5 sec delay, the best-fit IRF for the BOLD and MION data were {1.67, -0.67} and {0.20, 0.80}. These parameters represent the asymptotic contributions from two processes with different kinetics (see Methods).

The delay between the stimulus design and the IRF convolution can be removed by incorporating a third time constant (the delay of 1.5 sec) into the exponential basis for the IRF. The inclusion of a third exponential improved the description of the response onset immediately after stimulation. In the exponential basis described by time constants {1.5, 4.5, 13.5}, the optimal BOLD IRF was found to be {-0.89, 3.09, -1.20}, and the best fit for the MION IRF was {-0.21, 0.41, 0.80}. This basis was used for fits in Figs. 2.1-2.3 and for all statistical analyses.

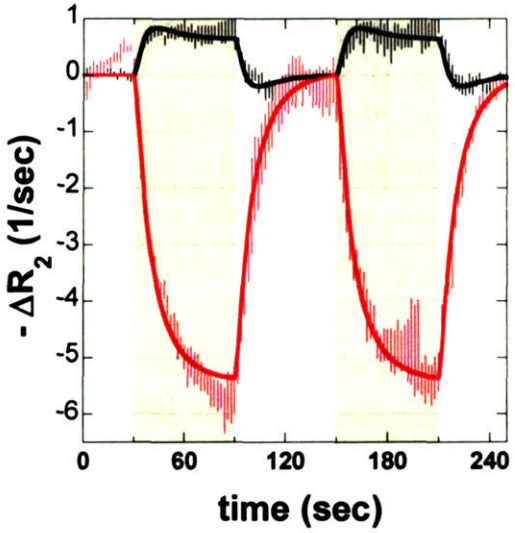

Fig. 2.2 Relaxation rate changes for BOLD (black) and MION (red) contrast, together with the corresponding linear model fits, during two cycles of the 60 sec of stimulus (gray shaded intervals) followed by 60 sec of baseline. At the end of the stimulus interval, MION relaxation rate changes were more than 7 times greater than BOLD changes. Peak MION signal change corresponds to a 25% increase in cerebral blood plasma volume.

The average BOLD and MION responses for the 4 sec stimuli, together with the respective IRF fits, are shown in Fig. 2.1b. Fig. 2.2 shows data and fits for the long block stimuli of 60 sec duration. In each case, a post-stimulus undershoot was associated with a slow post-stimulus decrease of blood volume. The enhancement in signal change was found to be a strong function of stimulus duration. For the 4 sec stimuli, the peak change in MION relaxation rate exceeded the BOLD change by a factor of 3 (Fig. 2.1b), but the enhancement increased to a factor of 7 for a stimulus of 60 sec duration (Fig. 2.2). Using the average value of the transverse relaxation due to MION to normalize the signal changes in this region of interest (R_2^{*MION} = 22.3 sec^{-1}), peak changes in cerebral blood volume averaged 8 % for the 4 sec stimuli (Fig. 2.1b) and 25 % for the 60 sec stimuli (Fig. 2.2).

In a time-invariant linear system, the slower MION response should be manifest as a low-pass filter on higher stimulation frequencies. Fig. 2.3 shows responses to repeated presentations of 4 sec of stimulus followed by 8 sec of baseline. This inter-stimulus interval is just sufficient for BOLD signal to return to baseline following each stimulus, whereas blood volume remains

elevated throughout the duration of the stimulus cycle. With these parameters, BOLD cyclic relaxation rate changes were about 50% as large as those for a long block stimulus, whereas the stimulus-induced fluctuations in the MION relaxation rate were only 20% as large as those for the longer stimulus of Fig. 2.2.

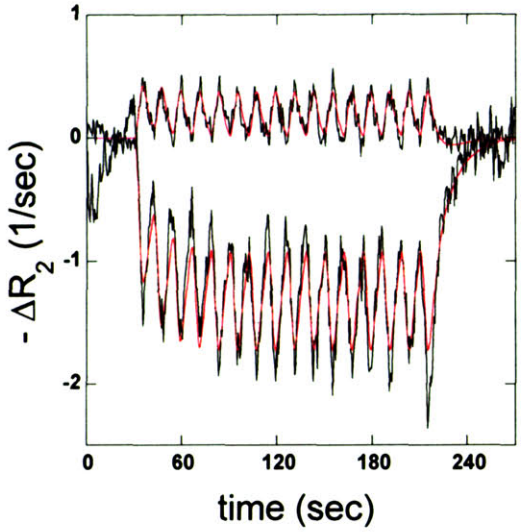

Fig. 2.3 Relaxation rate changes measured for BOLD (above y origin) and MION (below y origin) contrast during 16 cycles of 4 sec of stimulus followed by 8 sec of baseline. Black traces indicate data, and red traces show the linear model fit to the data. Whereas BOLD signal recovers to the baseline following each cycle, the slower MION response does not recover. In this rapidly presented stimulus paradigm, MION relaxation rate changes are slightly more than twice as large as BOLD changes.

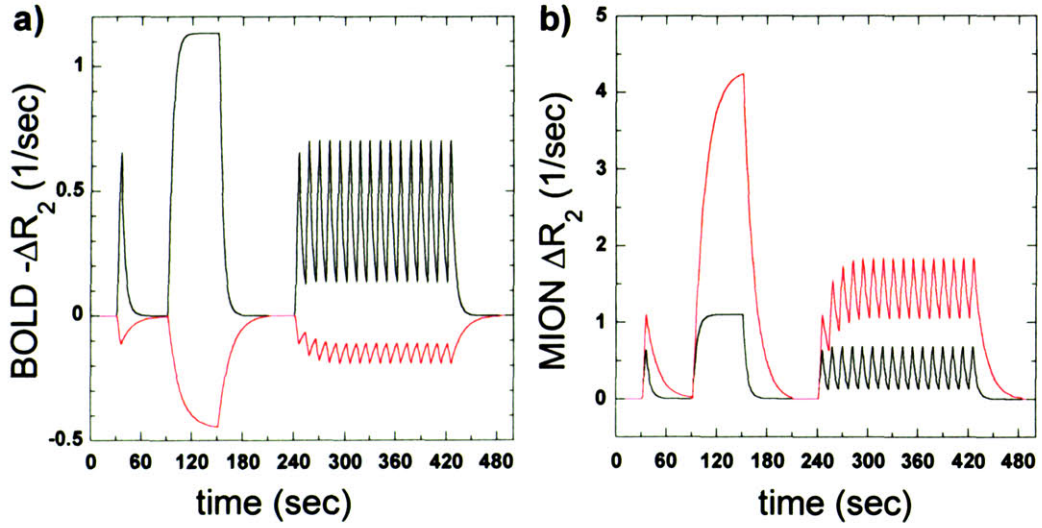

Fig. 2.4 A general linear model fit separated data obtained using BOLD (left) and MION (right) into a fast time response (black, 4.5 sec time constant) and a slow response (red, 13.5 sec time constant). Fits to the data are shown for stimuli of 4 sec (first response), 60 sec (second response), and a train of rapidly presented responses (4 sec on, 8 sec off). The total response (not shown) is the sum of the fast and slow components.

Insight into the underlying physiology of each method can be obtained from the 2-exponential decomposition of the impulse response function. For BOLD signal, the two time constants are most simply identified as the responses of blood oxygenation and blood volume. For the MION method, the time constants presumably are related to arterial and venous dilations. The exponential decomposition of the MION signal found that the slow time constant contained 80% of the strength during prolonged stimulation. The exponential decomposition of the BOLD signal suggests that changes in CBV reduce the BOLD effect by 40% during prolonged stimulation.

Fig. 2.4 shows the fast and slow components of the BOLD and CBV responses for each stimulus type, using a single scaling factor as determined by simultaneously fitting all the data (note that Figs. 2.1-2.3 use a separate scaling for each run, following the usual analysis procedure). By comparison of Fig. 2.4 with the data in Fig. 2.1-2.3, a single scaling factor well describes the BOLD data for each stimulus paradigm. The MION data is well described for the short and long stimuli, but the response to the rapidly presented stimuli is overestimated somewhat by the linear model analysis. CBV-weighted signal suffers a larger reduction in relative sensitivity than BOLD signal for short stimuli or event-related designs as compared to block stimuli, due to the slower response of CBV. Because the slow CBV response produces a negative BOLD offset that compensates the positive offset for rapidly presented stimuli, the dramatic baseline shift seen for the MION response in Fig. 2.3 is not evident in the BOLD data or the fitted response.

2.3.4 Functional Sensitivity and Spatial Localization

The use of exogenous contrast agent provided a large improvement in functional sensitivity, which depended upon both the stimulus paradigm and the spatial location within visual cortex. Fig. 2.5 shows the average BOLD and MION functional maps in monkey M-A for a single 4.5 minute run using the 60 sec stimulus paradigm. The maps are based upon the average T-scores across runs and scan sessions, and p-values were corrected for multiple comparisons. The underlying grayscale images are the spatially smoothed echo planar images from which the functional maps were derived. The general pattern of brain activation is similar for the two methods, but the overall sensitivity of the MION method is much higher.

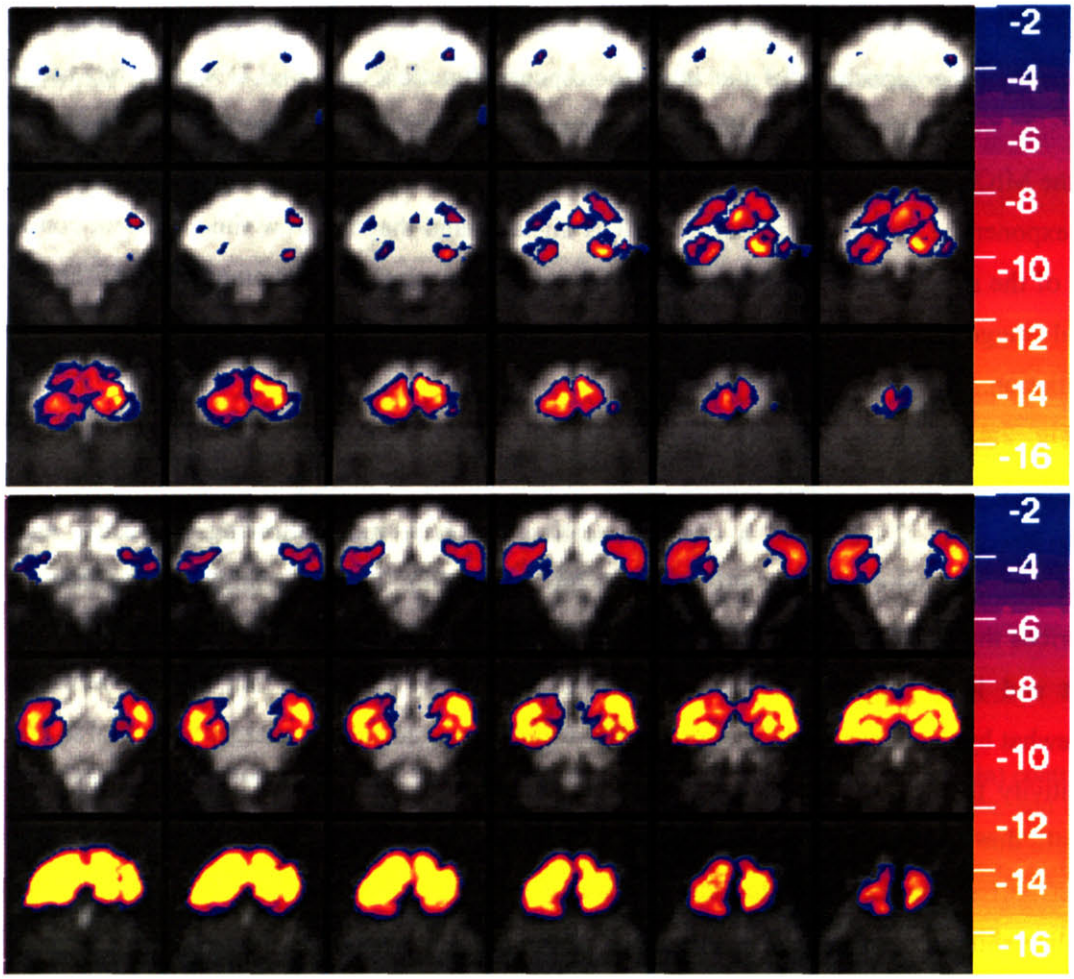

Fig. 2.5 Representative (average) functional brain maps obtained in an awake, behaving primate (M-A) during single 4.5 minute runs using either BOLD (top) or MION (bottom) contrast. The color scale shows the log of p-values from a T test after correcting for multiple comparisons, and the grayscale shows echo planar images from each data set. The stimulus consisted of 2 cycles of 60 sec of a flashing checkerboard followed by 60 sec of baseline.

Fig. 2.6 reveals several apparent differences in the functional maps for the two methods. The first panel shows statistical scores accumulated across 8 runs for 4 slices from the best BOLD functional data set in either animal. Strong BOLD signal changes occurred in the straight sinus at each level, with generally smaller significance levels for the sagittal sinus. These vessel artifacts were absent in the MION maps, since this dose of contrast agent eliminates intravascular signal changes that are associated with changes in blood oxygenation. However, the BOLD maps also show activation in tissue regions, identified as areas with good signal in the MION images. These areas (e.g., last slice in Fig. 2.6) form a bridge between the sinuses and areas identified as activated using the MION method. Presumably, this indicates a loss of BOLD functional resolution due to venous drainage from activated tissue.

Fig. 2.6b is a map of the ratio of MION CNR to BOLD CNR values for the last 3 slices in Fig. 2.5. These slices represent the most posterior aspect of primary visual cortex, where the calcarine fissure is prominent. Within a 6 mm strip centered on the calcarine fissure, BOLD significance levels were actually higher than those for the MION method, presumably as a result of the high blood volume fraction in this area near the sagittal sinus.

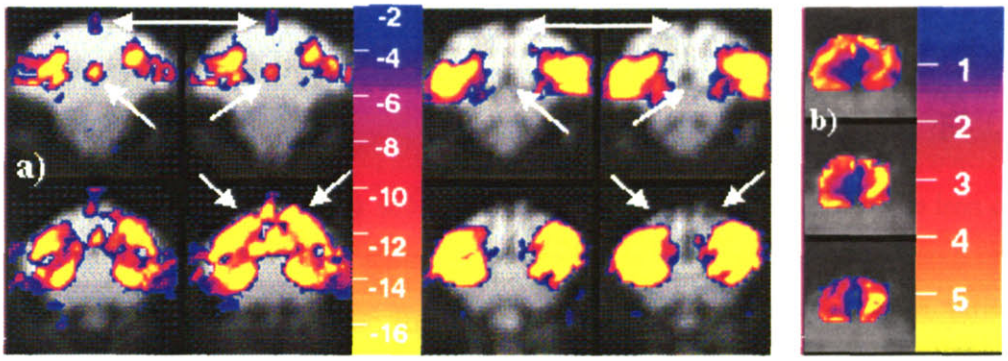

Fig. 2.6 a) Slices 3,4,9, and 10 from Fig. 2.5 after averaging across runs. BOLD functional maps (left, 8 runs) show contributions from the straight sinus and the superior sagittal sinus, which are not in evidence in the MION functional maps (right, 3 runs). Moreover, BOLD signal changes appear in tissue that bridges the venous sinuses and areas identified as activated by the MION technique. b) The ratio of MION CNR to BOLD CNR is shown as color overlay on the last 3 slices in Fig. 2.5. BOLD sensitivity exceeds that for the MION method within a 6 mm strip centered on the calcarine fissure, presumably due to the high blood volume fraction in this area near the sagittal sinus.

In order to assess the degree of similarity in brain activation as assessed by the BOLD and MION methods, and to compare the functional sensitivities of the two methods, Fig. 2.7 provides scatter plots of relaxation rate changes and contrast-to-noise ratios. Changes in BOLD and MION relaxation rates are compared throughout visual cortex for both animals for all voxels that show significant signal changes across runs with either method (Fig. 2.7a) and both methods (Fig. 2.7b). Signal changes in large vessels appear along the line $\Delta R_2^{*MION} = 0$ in Fig. 2.7a. In those voxels that are activated by both methods, the dominant correlation is a linear coupling of relaxation rate changes along a line that is approximately $\Delta R_2^{*MION} = 6\ \Delta R_2^{*BOLD}$ using this dose of contrast agent.

Fig. 2.7c compares the functional sensitivity of the two methods for all voxels in Fig. 2.7b. Low values of BOLD CNR can result from small changes in local neuronal activity or from low values of the resting blood volume fraction. The latter case accounts for voxels that exhibited a CNR enhancement greater than half an order of magnitude using exogenous agent, since the MION method has little CNR dependence on the resting state blood volume fraction (Mandeville and Marota, 1999). The highest values of BOLD CNR were predominantly associated with large resting blood volume fractions, and stimulus-induced BOLD signal changes in such areas were comparable to those obtained using the MION method.

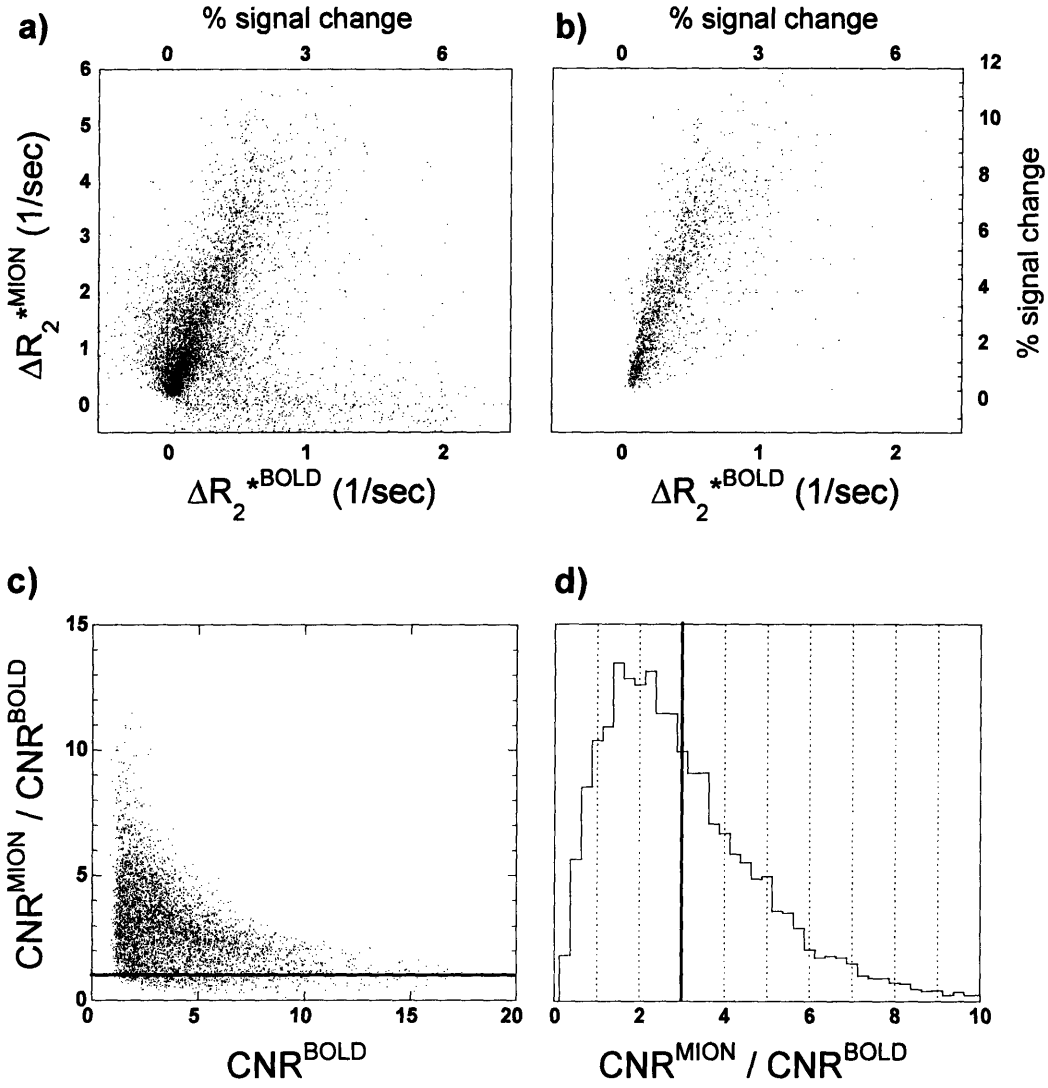

Fig. 2.7 a) A scatter plot of all voxels in primate brain that were activated by either the BOLD or the MION methods after registering across sessions and averaging across monkeys. b) Those voxels that were activated by both methods. Changes in relaxation rates were related in an approximately linear way for most voxels, but a significant fraction did not adhere to this relationship. c) The sensitivity enhancement for all voxels in panel "b" as a function of the BOLD contrast-to-noise ratio. d) A histogram of the ratio of functional sensitivities of the two methods. The MION method increased the functional contrast-to-noise ratio by a mean factor of 3, and a most likely factor of 2.

This figure demonstrates a very practical advantage of exogenous agent at 3 Tesla in awake primates. Most voxels that were identified as activated using BOLD signal were also selected by the MION method with equal or better statistical power, whereas voxels that had low BOLD CNR values were generally those that exhibited the greatest relative signal increases due to the use of iron oxide. Fig. 2.7d shows the one-dimensional distribution of CNR ratio averaged across animals and magnet sessions. The average increase in functional sensitivity in monkeys M-A and M-B was 3.0 and 3.3, respectively, using stimuli of 60 sec duration.

For shorter stimuli or more rapid presentation rates, the increase in functional sensitivity was smaller. When short stimuli (4 sec) were presented with a long inter-stimulus interval (26 sec), the average sensitivity of the MION method was only 1.7 times greater than that of the BOLD method (M-A: 1.5, M-B: 1.9). Fig. 2.3 demonstrates that short, rapidly presented stimuli may experience even greater reduction of MION sensitivity. For this particular stimulus paradigm, however, MION provided better than a factor of 2 improvement over the BOLD method, due to the inclusion of baseline samples at the beginning and end of the run.

2.4 Discussion

This study investigated the viability and quantified the advantages of employing an iron oxide contrast agent with a long blood half life to enhance functional brain imaging for repeated studies in awake, behaving primates. The viability of this approach was assessed by a series of experiments in two animals using MION contrast agent. The sensitivity and temporal response were compared to the common BOLD technique at a field strength of 3 Tesla using a variety of stimulus timings. Whereas the MION method works well in awake primates even at 1.5 Tesla (Vanduffel et al., 2001), the use of a 3 Tesla scanner in this study elevated BOLD signal to a sufficient level for quantitative spatio-temporal comparisons with the MION signal. Significantly, MION injection did not produce adverse behavioral effects, as assessed by response scores and session duration, and no obvious long term health problems have been encountered. In accordance with results obtained in anesthetized rodent models, the use of iron oxide greatly improved the quality and consistency of functional brain maps by increasing the magnitude of signal changes.

2.4.1 Temporal Response

This study employed a short stimulus to determine the impulse response function, a long stimulus to evaluate the asymptotic response, and a rapidly modulated stimulus to simulate an event-related design. Results showed that BOLD and CBV temporal responses differed significantly in the awake macaque, supporting the view arising from MRI studies in anesthetized rodents (Mandeville et al., 1999b; Mandeville et al., 1999a).

By decomposing the BOLD kinetics into two dominant processes, it was estimated that CBV changes reduce BOLD signal by about 40% during prolonged stimulation, in agreement with other empirical estimates based upon the use of exogenous contrast agent (35%, (Kennan et al., 1998)), (36%, (Mandeville et al., 1999a)), (46%, (Scheffler et al., 1999)). Due to intravascular contributions to BOLD signal (T_2^* changes in the blood), this estimate is expected to be somewhat dependent upon the magnetic field strength. By decomposing the MION kinetics into

two dominant processes, 80% of the strength during prolonged stimulation was attributed to a process that evolved more slowly than BOLD signal, and thus more slowly than blood flow and arterial dilation. However, if the rapid component of CBV change also contains a contribution from the elastic dilation of capillaries and veins (Mandeville et al., 1999b), then arterial dilation contributes less than 20% of total blood volume changes during prolonged stimulation.

As in the anesthetized rodent, the temporal characteristics of the signal implicate venous blood volume as a source of the BOLD post-stimulus undershoot, which may also have a neuronal contribution that modulates blood flow (Hoge et al., 1999). Of course, the underlying temporal dynamics of neuronal activity can be expected to influence the temporal response of CBV as well as BOLD signal. However, the general shape of the CBV response was quite consistent across brain structures in this study, and a very similar response was obtained by Vanduffel et al. (2001) despite the use of different stimuli.

Whatever the exact mechanism of the temporal smoothing applied to the response of cerebral blood plasma volume, this study demonstrates that CBV-weighted fMRI is amenable to a general linear model analysis. The slow response of CBV relative to BOLD signal implies that CBV is particularly advantageous for long stimuli in terms of detection sensitivity, since short or rapidly presented stimuli may not reach a maximum response.

2.4.2 Functional sensitivity and Spatial Localization

Previous studies in anesthetized rodents using iron oxide contrast agents have demonstrated a large increase in functional sensitivity relative to BOLD signal (Mandeville et al., 1998; Kennan et al., 1998). The sensitivity enhancement is a strong function of the local blood volume fraction due to the different "vascular filters" of the BOLD and MION methods (Mandeville and Marota, 1999; Mandeville et al., 2001a). This study confirmed these results in the absence of anesthesia in a primate species. The use of MION contrast agent increased functional sensitivity relative to BOLD signal at 3 Tesla by a mean factor of 3 across macaque visual cortex for a long stimulus. The dose of contrast agent, local blood volume fraction, magnetic field strength, resting state blood oxygenation, and duration and separation of stimuli are among the factors which influence the degree by which exogenous contrast agent boosts the size of absolute signal changes relative to the BOLD method.

The dose of contrast agent alters the transverse relaxation rate of MRI signal as $R_2^{*TOTAL} = R_2^{*endogenous} + R_2^{*MION}$, where R_2^{*MION} depends upon dose in a nearly linear way (Kennan et al., 1994; Boxerman et al., 1995). The sensitivity for functional imaging should depend roughly upon the function $TE\ R_2^{*MION} \exp(-TE\ R_2^{*MION})$, where R_2^{*MION} represents the value across a large brain

volume in order to account for regional variations in the parenchymal blood volume fraction. In this study, we chose the minimum obtainable echo time of 20 msec for our single shot EPI sequence in order to minimize susceptibility artifacts. The selected iron dose (TE $R_2^{*MION} \sim 0.4$) was on the low side of the sensitivity curve (theoretical maximum at TE $R_2^{*MION} = 1$) in order to reduce the injected iron and to maintain an acceptable signal-to-noise ratio, while still delivering about 70% of the CNR advantage. These results suggest that 10 mg/kg is a suitable iron dose using an echo time of about 20 msec for this agent in monkeys, results that are comparable with previous rat studies. Since the induced magnetization of MION saturates as a function of field strength (Shen et al., 1993), the optimal MION dose should be roughly independent of field above 1.5 Tesla.

Resting state venous blood oxygenation is the analogue of iron dose for the BOLD method. Because all anesthetics decrease venous oxygenation (Michenfelder, 1988), which depends upon the ratio of oxygen utilization to blood flow, BOLD imaging can be expected to have a slightly higher sensitivity in the awake state than in the presence of anesthesia for the same fractional change in blood flow. The anesthesia-induced reduction of BOLD sensitivity should be most pronounced for the inhalational vasodilators like halothane, isoflourane, and desflourane, which decrease metabolic rate but increase cerebral blood flow above the non-anesthetized state. This suggests that the advantages of the MION method should be somewhat greater in the anesthetized state relative to awake studies. Nevertheless, the three-fold increase in sensitivity provided by MION in the awake macaque at 3 Tesla is not far out of line with results from anesthetized rodents (Mandeville et al., 1998; Mandeville et al., 2001a; Chen et al., 2001) after scaling for differences in magnetic field strength.

Based upon these results at 3 Tesla, we expect that a similar choice of experimental parameters at 1.5 Tesla should increase sensitivity relative to the BOLD method by a factor of approximately 6. Vanduffel et al. (2001) found that a slightly lower MION dose boosted absolute signal changes by a factor of 5 relative to BOLD signal in motion-sensitive visual regions during prolonged stimulation. This would correspond to a 5-fold increase in sensitivity, in good agreement with projections based upon our 3 Tesla data, if we assume that injection of MION leaves the noise unaltered. Dubowitz et al. (2001) reported a 3-fold increase in percentage signal changes and a 2-fold reduction of baseline signal, corresponding to a CNR increase of about 1.5. This lower value is presumably due to the short stimulus duration, lower dose of contrast agent, and longer echo time used in that study.

Although the spatial patterns of brain activation observed using the BOLD and MION methods were quite similar, differences were also apparent. Large venous sinuses showed

changes in BOLD signal, whereas MION signal was extinguished in such areas by the large dose of contrast agent. While such obvious BOLD vascular artifacts usually will not be misidentified as activated tissue, some tissue regions also exhibited BOLD but not MION signal changes, a result presumably indicating downstream dilution of deoxyhemoglobin and degradation of BOLD functional resolution. It is much more difficult to assess whether local blood volume changes can occur without changes in deoxyhemoglobin at the spatial resolution used in this study, since the much higher sensitivity of the MION method reveals activation that may be below the BOLD threshold.

Finally, it is important to note that intra-subject and inter-subject comparisons using repeated injections of a contrast agent like MION need to monitor the blood dose of agent during each session in order to correct for cross-session differences in the blood concentration of iron. This consideration becomes important if different doses are used, or whenever the dose of agent administered during one session does not have time to clear the bloodstream before the subsequent imaging session. Cross-session comparisons either can rely upon percent calculations in CBV or global normalization of relaxation rates, as described in the methods, with the latter being better suited for studies that cannot, for logistical reasons, obtain both pre-injection and post-injection baselines of signal within the same session. Cross-session statistical comparisons, on the other hand, can be biased by differences in iron dose in a way that cannot be corrected retrospectively. To prevent systematic differences in statistical power from biasing group average results, blood iron concentrations should be as consistent as possible across sessions, and ideally one should use doses near the optimal dose (iron-induced signal attenuation of e^{-1}), since that choice minimizes the dependence of statistical power on iron dose.

2.4.3 Iron Accumulation and Management

In human studies, dextran-coated ultrasmall superparamagnetic iron oxides (USPIOs) similar to MION have shown very low toxicity at doses up to 4 mg-Fe/kg (Taylor et al., 1999). Agents currently in clinical trials include AMI-227 (Advanced Magnetics Inc., Cambridge, MA, USA) for imaging liver or splenic lesions (Sharma et al., 1999) and NC100150 (Nycomed Imaging, Oslo, Norway) for coronary angiography (Taylor et al., 1999).

In repeated primate experiments using high iron doses for brain imaging as reported here, the primary concerns are 1) the development of an immune response to dextran, and 2) the gradual accumulation of iron in excess of body requirements. There was no evidence of allergic reaction during these studies, and the total injected iron dose during these series is considered insufficient to cause acute or long term adverse effects. In humans, the normal level of total body iron is

roughly 60 mg/kg, the maximum natural rate of iron excretion in a non-menstruating adult is about 10 mg/kg/year, and the liver is the repository for 90% of excess iron (Leggett et al., 2000; Barton et al., 2000). Thus, we estimate that total iron doses of 40-60 mg/kg in the two animals increased body iron stores by a factor of about 2. While iron metabolism is imperfectly understood, the results of chronic iron overload have been studied for decades due to genetic diseases that elevate liver and total body iron stores by an order of magnitude relative to normal levels for many years (Edwards et al., 2000; Olivieri and Brittenham, 1997).

For continued studies that deposit much more contrast agent, iron monitoring and management should form an important part of the protocol. Monitoring can be achieved by sampling blood transferrin saturation and total blood iron concentration (Olivieri and Brittenham, 1997). MRI provides the highest sensitivity for non-invasive assessment of liver iron, with a detection threshold of 2 to 3 times normal liver iron levels (Guyader and Gandon, 2000; Bonkovsky et al., 1999). Phlebotomy, the standard treatment for hemochromatosis, removes about 4 mg/kg iron per week by withdrawing about 7 ml blood per kg (Barton et al., 2000). Additional iron can be removed by desferoxamine chelation, which preferentially targets stored iron in liver parenchyma and other tissues, with no effect on hemoglobin iron and little affinity for transferrin-bound iron (Herschko et al., 2000). This method can be used to minimize or reverse iron overload without worry of causing iron deficiency. However, long term use of very high doses of desferoxamine can produce adverse effects and should be avoided (Herschko et al., 2000; Olivieri and Brittenham, 1997). For the treatment of the genetic disorder thalassemia major, a suggested goal for desferoxamine chelation therapy is maintenance of total body iron stores within a factor of about 5 times normal levels (Olivieri and Brittenham, 1997).

The experience from the human population suggests that repeated fMRI studies using iron oxide contrast agent can be performed in this primate model until total body stores increase by several factors without worry of significant health complications. However, subcutaneous injections of an iron chelator should be considered as a method to prevent iron stores from reaching unacceptable levels. Vanduffel et al. have now injected as much as 166 mg/kg iron into a single monkey (personal communication) and measured normal blood iron levels after desferoxamine treatment ("desferal", Novartis Pharma AG, Basle, Switzerland). No significant adverse behavioral effects have been observed in those monkeys after more than one year from the first MION injection.

2.5 Conclusions

Our results demonstrate that functional MRI can be performed reliably on awake, behaving macaques at a field strength of 3 Tesla using a commercial horizontal bore MRI system. Although BOLD activation maps of reasonable quality were obtained with sufficient averaging, the use of MION contrast agent significantly increased stimulus-correlated signal changes, thereby improving the quality and reliability of results. We did not observe any obvious adverse effects on the monkeys' health due to MION injection. However, we expect that iron monitoring and management will be necessary for a long-term program of repeated fMRI studies using iron oxide in these animals.

2.6 References

Barton JC, McDonnell SM, Adams PC, Brissot P, Powell LW, Edwards CQ, Cook JD, Kowdley KV, 2000. Management of hemochromatosis. In: Hemochromatosis: Genetics, pathophysiology, diagnosis, and treatment. (Barton JC, Edwards CQ, ed), pp 329-338. Cambridge, U.K.: Cambridge University Press.

Bonkovsky HL, Rubin RB, Cable EE, Davidoff A, Pels Rijcken TH, Stark DD, 1999. Hepatic Iron Concentration: nonivasive estimation by means of MR Imaging techniques. Radiology 212: 227-234.

Boxerman JL, Hamberg LM, Rosen BR, Weisskoff RM, 1995. MR contrast due to intravascular magnetic susceptibility perturbations. Magn Reson Med 34: 555-566.

Boynton GM, Engel SA, Glover GH, Heeger DJ, 1996. Linear systems analysis of functional magnetic resonance imaging in human V1. J Neurosci 16: 4207-4221.

Chen YI, Mandeville JB, Nguyen TV, Talele A, Cavagna F, Jenkins BG, 2001. Improved Mapping of Pharmacologically Induced Neuronal Activation using the IRON Technique with Superparamagnetic Iron Blood Pool Agents. J Magn Reson Imaging 14: 517-524.

Cox RW, Hyde JS, 1997. Software tools for analysis and visualization of FMRI data. NMR in Biomedicine 10: 171-178.

Disbrow EA, Slutsky DA, Roberts TP, Krubitzer LA, 2000. Functional MRI at 1.5 tesla: a comparison of the blood oxygenation level-dependent signal and electrophysiology. Proc Natl Acad Sci U S A 97: 9718-23.

Dubowitz DJ, Bernheim KA, Chen D-Y, Bradley Jr. WG, Andersen RA, 2001. Enhancing fMRI contrast in awake-behaving primates using intravascular magnetite dextran nanoparticles. NeuroReport 12: 2335-2340.

Dubowitz DJ, Chen DY, Atkinson DJ, Grieve KL, Gillikin B, Bradley WGJ, Andersen RA, 1998. Functional magnetic resonance imaging in macaque cortex. Neuroreport 9: 2213-2218.

Edwards CQ, Griffen LM, Bulaj ZJ, Ajioka RS, Kushner JP, 2000. Estimate of the frequency of morbid complications of hemochromatosis. In: Hemochromatosis: Genetics, pathophysiology, diagnosis, and treatment. (Barton JC, Edwards CQ, ed), pp 312-317. Cambridge, U.K.: Cambridge University Press.

Enochs WS, Harsh G, Hochberg F, Weissleder R, 1999. Improved delineation of human brain tumors on MR images using a long-circulating, superparamagnetic iron oxide agent. J Magn Reson Imaging 9: 228-232.

Friston KJ, Holmes AP, Worsley KJ, Poline JP, Frith CD, Frackowiak RSJ, 1995. Statistical Parametric Maps in Functional Imaging: A General Linear Approach. Human Brain Mapping 2: 189-210.

Guyader D, Gandon Y, 2000. Computed tomography and magnetic resonance imaging in the diagnosis of hemochromatosis. In: Hemochromatosis: Genetics, pathophysiology, diagnosis, and treatment. (Barton JC, Edwards CQ, ed), pp 219-225. Cambridge, U.K.: Cambridge University Press.

Hayashi T, Konishi S, Hasegawa I, Miyashita Y, 1999. Short communication: mapping of somatosensory cortices with functional magnetic resonance imaging in anaesthetized macaque monkeys. Eur J Neurosci 11: 4451-6.

Herschko C, Link G, Konijn AM, 2000. Chelation therapy in iron overload. In: Hemochromatosis: Genetics, pathophysiology, diagnosis, and treatment. (Barton JC, Edwards CQ, ed), pp 339-354. Cambridge, U.K.: Cambridge University Press.

Hoge RD, Atkinson J, Gill B, Crelier GR, Marrett S, Pike GB, 1999. Stimulus-dependent BOLD and perfusion dynamics in human V1. NeuroImage 9: 573-585.

Josephson L, Groman EV, Menz E, Luis JM, Bengele H, 1990. A Functionalized Superparamagnetic Iron Oxide Colloid as a Receptor Directed MR Contrast Agent. Magn Reson Imag 8: 637.

Kennan RP, Scanley BE, Innis RB, Gore JC, 1998. Physiological basis for BOLD MR signal changes due to neuronal stimulation: separation of blood volume and magnetic susceptibility effects. Magn Reson Med 40: 840-846.

Kennan RP, Zhong J, Gore JC, 1994. Intravascular Susceptibility Contrast Mechanisms in Tissues. Mag Reson Med 31: 9-21.

Leggett RW, Barton JC, Eckerman KF, 2000. Mathematical models of metal metabolism in hemochromatosis. In: Hemochromatosis: Genetics, pathophysiology, diagnosis, and treatment. (Barton JC, Edwards CQ, ed), pp 170-176. Cambridge, U.K.: Cambridge University Press.

Logothetis NK, Guggenberger H, Peled S, Pauls J, 1999. Functional imaging of the monkey brain. Nat Neurosci 2: 555-562.

Logothetis NK, Pauls J, Augath M, Trinath T, Oeltermann A, 2001. Neurophysiological investigation of the basis of the fMRI signal. Nature 12: 150-157.

Mandeville JB, Jenkins BG, Kosofsky BE, Moskowitz MA, Rosen BR, Marota JJA, 2001a. Regional Sensitivity and Coupling of BOLD and CBV Changes during Stimulation of Rat Brain. Magn Reson Med 45: 443-447.

Mandeville JB, Marota JJA, 1999. Vascular Filters of Functional MRI: Spatial Localization using BOLD and CBV Contrast. Magn Reson Med 42: 591-598.

Mandeville JB, Marota JJA, Ayata C, Moskowitz MA, Weisskoff RM, Rosen BR, 1999a. An MRI Measurement of the Temporal Evolution of Relative CMRO2 During Rat Forepaw Stimulation. Magn Reson Med 42: 944-951.

Mandeville JB, Marota JJA, Ayata C, Zaharchuk G, Moskowitz MA, Rosen BR, Weisskoff RM, 1999b. Evidence of a Cerebrovascular Post-arteriole Windkessel with Delayed Compliance. J Cereb Blood Flow Metab 19: 679-689.

Mandeville JB, Marota JJA, Kosofsky BE, Keltner JR, Weissleder R, Rosen BR, Weisskoff RM, 1998. Dynamic Functional Imaging of Relative Cerebral Blood Volume During Rat Forepaw Stimulation. Magn Reson Med 39: 615-624.

Mandeville JB, Vanduffel W, Fize D, Nelissen K, Rosen BR, Tootell RB, Van Hecke P, Orban GA, 2001b. Enhanced fMRI using Iron Oxide Contrast agent in Awake, Behaving Primates. In: Int. Soc. Magn. Reson. Med. ,Glasgow, Scotland, U.K., p 1334.

Michenfelder JD, 1988. Anesthesia and the brain. Churchill Livingstone, New York.

Olivieri NF, Brittenham GM, 1997. Iron-chelating therapy and the treatment of thalassemia. Blood 89: 739-761.

Scheffler K, Seifritz E, Haselhorst R, Bilecen D, 1999. Titration of the BOLD effect: separation and quantitation of blood volume and oxygenation changes in the human cerebral cortex during neuronal activation and ferumoxide infusion. Magn Reson Med 42: 829-36.

Sharma R, Saini S, Ros PR, Hahn PF, Small WC, de Lange EE, Stillman AE, Edelman RR, Runge VM, Outwater EK, Morris M, Lucas M, 1999. Safety profile of ultrasmall superparamagnetic iron oxide ferumoxtran-10: phase II clinical trial data. J Magn Reson Imaging 9: 291-294.

Shen T, Weissleder R, Papisov M, A Bogdanov J, Brady TJ, 1993. Monocrystalline Iron Oxide Nanocompounds (MION): Physiochemical Properties. Magn Reson Med 29: 599-604.

Stefanacci L, Reber P, Costanza J, Wong E, Buxton R, Zola S, Squire L, Albright T, 1998. fMRI of monkey visual cortex. Neuron 20: 1051-1057.

Taylor AM, Panting JR, Keegan J, Gatehouse PD, Amin D, Jhooti P, Yang GZ, McGill S, Burman ED, Francis JM, Firmin DN, Pennell DJ, 1999. Safety and preliminary findings with the intravascular contrast agent NC100150 injection for MR coronary angiography. J Magn Reson Imaging 9: 220-227.

van Bruggen N, Busch E, Palmer JT, Williams SP, de Crespigny AJ, 1998. High-resolution functional magnetic resonance imaging of the rat brain: mapping changes in cerebral blood volume using iron oxide contrast media. J Cereb Blood Flow Metab 18: 1178-83.

Vanduffel W, Fize D, Mandeville JB, Nelissen K, Van Hecke P, Rosen BR, Tootell RBH, Orban GA, 2001. Visual Motion Processing Investigated using Contrast-enhanced fMRI in Awake Behaving Monkeys. Neuron 32: 565-577.

Vanduffel WJM, Beatse E, Nelissen K, Tootell RBH, Todd JT, Orban GA, 2000. Areas involved in extracting structure from motion: an fMRI study in the awake fixating monkey. In: Soc. Neurosci. Abstr. , New Orleans, LA, p 593.

Weissleder R, Elizondo G, Wittenberg K, 1990. Ultrasmall superparamagnetic iron oxide. Characterization of a new class of contrast agents for MR imaging. Radiology 175: 489-493.

Chapter 3

Characterization of Event-Related Designs using IRON and BOLD fMRI

3.0 Preface

An important contribution to the success of fMRI in recent years has been the development of event-related designs. In these type of designs, rapid presentation of a given number of different event types opens the door to a more dynamic study of brain activation with fMRI, and allows measurement of regional hemodynamic changes due to a single sensory or cognitive event, as well as differential comparisons of different responses (for review, see Rosen et al., 1998).

In chapter 2 we found that IRON contrast significantly increases detection power with respect to BOLD contrast, particularly in block designs. The gain in sensitivity decreases for rapid stimulus presentations, due to the slower IRON impulse response function. In this chapter we try to find strategies to recover this loss in sensitivity, by searching for distributions of interstimulus intervals that maximize detection power without significantly raising design predictability.

Building on previous work by Dale and colleagues that utilized random distributions of ISIs as a way to maximize estimation efficiency (Burock et al., 1998; Dale, 1999), in this chapter we evaluated efficiency, a quantity that is directly proportional to averaging time, for BOLD and IRON contrasts in event-related designs of varying ISIs chosen from different distributions: fixed, random, and pseudo-random. In addition, we introduced a quantitative way to measure the predictability of a design, starting from the fact that a completely predictable design will have zero entropy.

3.1 Introduction

Event-related (ER) designs generally consist of rapidly presented interleaved trials of multiple event types of short duration. These designs are extremely useful in the exploration of cognitive processes, as they provide a reduction in behavioral confounds like neural habituation and anticipation, enable tagging of different stimulus types through subject interaction, and allow comparisons between fMRI and other modalities, such as EEG and MEG, that use very short stimulus durations for temporal averaging (Rosen et al., 1998; D'Esposito et al., 1999; Josephs and Henson, 1999). The use of ER designs has greatly increased the range of available stimulus

paradigms, even though hemodynamic impulse response functions (IRFs) are slow compared with the underlying neuronal response. ER designs have been extensively characterized with the BOLD method (Buckner et al., 1996; Cohen, 1997; Josephs et al., 1997; Zarahn et al., 1997; Friston et al., 1998a) and with perfusion-based methods (Yang et al., 2000; Liu et al., 2002).

Previous comparisons between BOLD and IRON fMRI methods in rats (Mandeville et al., 1998 and 1999) and awake, behaving no non-human primates (Vanduffel et al., 2001; Leite et al., 2002) showed the IRON method greatly improves the sensitivity of detection of activation and the apparent accuracy of spatial localization. One drawback of the IRON method is its intrinsically slower temporal response, raising the obvious question of its performance in event-related designs.

In this study we assessed the utility of the IRON technique in ER designs to test the hypothesis that due to its inherent slower temporal response, the IRON method should benefit more than the BOLD method by randomization, or semi-randomization, of interstimulus intervals (ISIs) in a stimulus design. We introduce an objective measure of predictability, the Shannon Entropy, and show that, together with detection efficiency, this quantity provides a means to evaluate tradeoffs for any distribution of ISI values. Simulations were used to quantify relative detection efficiency of various fixed and randomized designs under the assumption of temporal linearity between stimulus and response, and experiments in awake non-human primates were conducted to test the validity of our predictions.

A preliminary report of this work was presented previously (Leite et al., 2003).

3.2 Background

3.2.1 General Linear Model

In our simulations and data analysis, we assume a linear time-invariant model for the observed fMRI response (Friston et al., 1995; Boynton et al., 1996; Dale and Buckner, 1997), such that the fMRI signal is described using a general linear model (GLM) with impulse response estimators of the hemodynamic response, as described by equations 3.3 or 3.4 in the Appendix. The system is characterized by biased IRFs that can vary according to the physiology of the measurement technique. Hemodynamic IRFs for both BOLD and IRON methods were determined in a previous work (Leite et al., 2002) and are shown in Fig. 3.1a.

3.2.2 Detection Power and Estimation Efficiency

In the limit where the shape of the hemodynamic IRF does not vary, estimation efficiency and detection power are equivalent quantities, simply designated efficiency or detection

efficiency (see Appendix). Detection efficiency equals the square of the contrast-to-noise ratio (CNR), and increases linearly with the averaging time.

Block designs maximize detection efficiency (Friston et al., 1999). For periodic ER designs an optimum ISI exists below which detection power and estimation efficiency greatly decrease with ISI (Dale, 1999; Bandettini and Cox, 2000), and scanning times must be lengthened accordingly. An overall increase in detection efficiency per unit time can be achieved by randomizing the ISIs (Dale and Buckner, 1997; Burock et al., 1998; Dale, 1999; Friston et al., 1999). Certain semi-random designs combine the benefits of block designs with respect to detection power (Friston et al., 1999; Liu et al., 2001; Birn et al., 2002). For example, one can design these paradigms such that the stimuli agglomerate in a finite number of clusters, and within each of these clusters the ISIs are short and random. In this manner, one will obtain a non-uniform distribution of ISIs, with higher probabilities for shorter and larger ISIs within the window considered, which will afford a considerable gain in detection efficiency.

3.2.3 Entropy as a Measure of Predictability

In addition to achieving high CNR or high sensitivity, it is important to devise stimulus paradigms with low predictability. Noting that a decrease in predictability is equivalent to an increase in randomness, the Shannon entropy (Cover and Thomas, 1991) can be used to quantify predictability. Alternative ways have been suggested by Liu and colleagues, who initially used an empirical measure of predictability (Liu et al., 2001), and later introduced conditional entropy as a more objective measure (Liu and Frank, 2004).

The Shannon entropy is defined as a measure of the uncertainty about the identity of objects in an ensemble (Cover and Thomas, 1991). For instance, consider the random variable X that describes the interstimulus intervals. Consecutive ISIs X_1, X_2, ..., X_n, can assume any state within a particular space with probability P(X = x) For the Shannon entropy H(X) will give the uncertainty in X:

$$H(X) = -\sum_{x_i \in \Omega_X} P(X = x_i) \log_a P(X = x_i). \tag{3.1}$$

Specifying the basis of the logarithm assigns units to the uncertainty: if a equals the number of possible states, then H(X) will vary between 0 and 1.

The Shannon Entropy can be employed as a useful measure to set an upper limit on subject predictability P:

$$P_{max} = 1 - H(X). \tag{3.2}$$

A fixed ISI design has maximum predictability and zero entropy. Maximum entropy (minimum predictability) is achieved for a uniform probability distribution where $P(X = x_i)$ is constant and equals $1/ISI_{max}$.

The Shannon entropy is a global measure of entropy, in contrast with the local character of the conditional entropy. According to the Asymptotic Equipartition Property (Cover and Thomas, 1991), the probability of observing one sequence $X_1, X_2, \ldots, X_n$ is almost always the same as any other, and the exact sequence observed is not as important as H(X). Nevertheless, a calculation of the conditional entropy requires a precise knowledge of the local succession of events, i.e., the conditional entropy simply corresponds to a particular realization of the Shannon entropy.

3.3 Methods

3.3.1 Simulations

ISI distributions for ER paradigms can be generated in a multitude of ways, including binary shift register (Buracas et al., 2002), nonstationary probabilities that evolve in time (Friston et al., 1999), or stationary distributions; this study employed the latter method. While entropy can be calculated directly from a given distribution, detection efficiency depends upon the IRF and can only be determined from simulations. Synthetic data sets were generated by convolving previously measured BOLD and IRON hemodynamic IRFs (Leite et al., 2002) with different types of stimulus paradigms. Four types of stimulus designs were generated with $ISI_{av} = \{4, 12, 20\}$ sec:

a. Fixed probability distribution with zero probability, given by $\delta(ISI - ISI_{av})$.

b. Random uniform distribution with $ISI \in \{0, \ldots, 2ISI_{av}\}$ in steps of 1 sec.

c. Semi-random distributions (Fig. 3.1b):

   i. Notch probability distribution, symmetrical around ISI_{av}.

   ii. Exponential probability distribution, approximately zero at $2ISI_{av}$.

For random or semi-random designs, the probability distribution derived from a run of finite duration is a poor approximation to the true probability distribution that generated that particular run. This implies that a very large number of stimulus paradigms of finite length have to be generated from the same probability distribution, and the resulting distributions accumulated across all runs to yield a better approximation. The final entropy is then calculated from the final ISI distribution and normalized by the theoretical maximum entropy for an equivalent uniform distribution. Likewise, the detection efficiency for each design type is averaged across all runs generated from the same probability distribution.

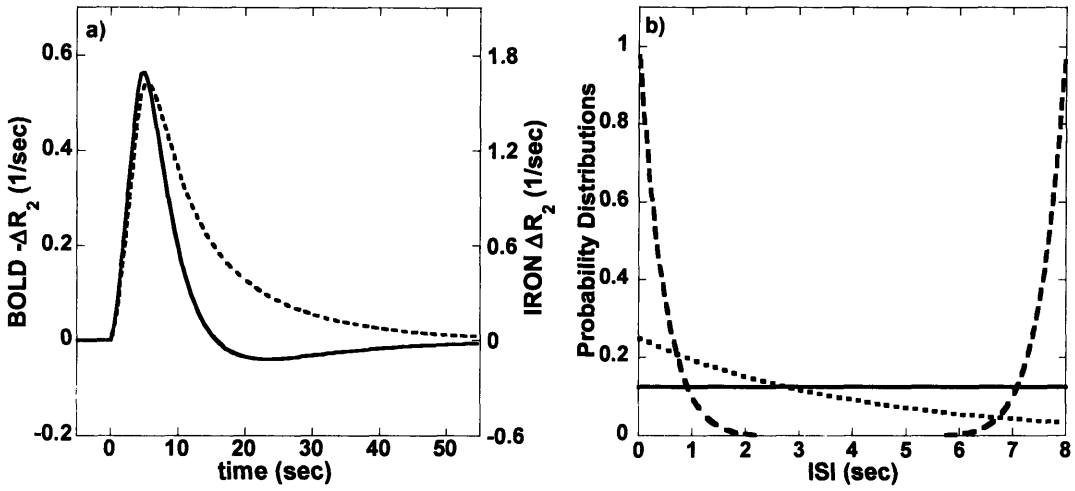

Fig 3.1. Input to simulations. a) Hemodynamic impulse response functions for BOLD (solid line) and IRON (dashed line) signal, as measured previously (Leite et al., 2002). b) Sample distributions of interstimulus intervals for an average ISI of 4 sec: uniform random distribution (solid line), exponential distribution (dotted line), and notch distribution (dashed line). The exponential distribution's ISI window was equal to 3.8 times the average ISI.

Three nuisance terms were added to the design matrix to model the baseline when performing the analysis of real and simulated data (but not when simulated data were generated). In order to avoid increases in detection power due to shifts in baseline, which bias single-event efficiencies relative to multi-event paradigms, the design matrix and data were filtered using an inclusion matrix **I** (see Appendix and Fig. 3.4) to ignore time points at the beginning and end of runs, where long-range effects of the hemodynamic tail produce a baseline offset.

3.3.2 Animal Model

All experiments were performed at the Massachusetts General Hospital according to NIH and Institutional animal care guidelines, following the general procedures as described previously (Leite et al., 2002).

Five monkeys were trained to perform a high acuity fixation task while visual stimuli were presented in the background. Infrared eye tracking (DQW1_10 Version 1.10L, ISCAN, Inc. 1990-2004) was performed. Horizontal and vertical pupil positions were recorded at 120 Hz, and water rewards were discontinued every time the pupil positions were consistently outside a pre-defined box centered at the fixation point. The box dimensions were chosen just large enough (smaller than $1° \times 1°$) to tolerate noise from the eye-tracker apparatus. On average, monkeys fixated accurately within defined tolerances about 80% of the time.

For all studies that employed the monocrystalline iron oxide nanoparticle (MION) contrast agent (Weissleder et al., 1990; Shen et al., 1993), the MION solution was injected in the femoral

vein below the knee just prior to each scanning session. An iron dose of 8 - 10 mg/kg was injected in each IRON session.

3.3.3 Visual Stimulation

The visual stimulus (8 Hz alternating black and white pinwheel checkerboard versus uniform gray screen), was projected from an LCD projector onto a screen which was positioned approximately 55 cm in front of the monkey's eyes. The stimulus covered a visual field of approximately $21° \times 24°$, and the fixation point ($0.2° \times 0.2°$) was present in the center of the screen at all times.

Five stimulus paradigms, each lasting 5 min, were acquired for each average ISI, making a total of 15 different stimulus paradigms. Each paradigm included 30 sec of baseline at the beginning and end. In every case the ON duration was 4 sec. Of the five paradigms, one was a fixed paradigm, and the remaining four were different random paradigms, each with an average ISI equal to ISI of the fixed paradigm. The random paradigms were the four paradigms achieving the highest detection efficiencies out of 10000 simulated trials.

In each scanning session we tried to acquire at least one run with each paradigm. Included in this study are the results from seven BOLD sessions and ten IRON sessions, corresponding to the same total number of runs. Scanning sessions typically lasted 2 – 3 hours.

3.3.4 Magnetic Resonance Imaging

Experiments were performed in a 3 Tesla Siemens Allegra scanner (Siemens Medical System, Erlangen, Germany) using a custom surface coil for the radio frequency excitation and reception of signal. All functional imaging employed a single shot multislice echo planar imaging with an isotropic resolution of 1.5 mm. 25 slices were acquired using a repetition time of 1.5 sec and 90° flip angle. All BOLD and IRON studies employed a gradient echo time of 21 msec (the minimum achievable value for the selected resolution and sequence).

In addition to functional imaging, data were acquired in each IRON session to enable the calculation of T_2^* maps by obtaining 9 gradient echo times from 21 to 66 msec at 5 msec intervals. These data were collected in the beginning and end of each IRON session, and were used to monitor IRON dose (Leite et al., 2002).

3.3.5 Data Analysis

Monkeys' body motion outside the field of view induced changes in the magnetic field that caused image distortions. The distortions were of two types: apparent translations of the brain (despite physical fixation of the head) and deformations. We were able to correct for the

translations by applying motion correction to all data sets using the Analysis of Functional NeuroImages (AFNI) motion correction algorithm (Cox and Hyde, 1997). Moreover, all data were spatially smoothed using a 2-dimensional Gaussian filter with a full-width at half-maximum of 3 mm.

The statistical power of the BOLD and IRON methods were measured using general linear model methods (see Appendix), and the IRFs determined from a previous study (Leite et al., 2002), as shown in Fig. 3.1a.

Because perfect registration between subjects was difficult to achieve and session duration varied according to the monkey's willingness to work, we opted to analyze each session separately and normalize detection efficiency to the 20 sec fixed ISI paradigm. All runs were concatenated together and a session region of interest (ROI) was defined as all voxels with p-values below the Bonferroni-corrected p-value (false positive rate of 0.01 corrected for 25 slices with 64 by 64 pixels each). Runs of each type (fixed or random presentations for a given ISI) were concatenated together, and the corresponding detection efficiency within the ROI was determined and normalized by the efficiency of the fix paradigm with 20 sec ISI. Finally, these normalized values were averaged across sessions, and values falling outside a 95% confidence interval were excluded from subsequent analysis.

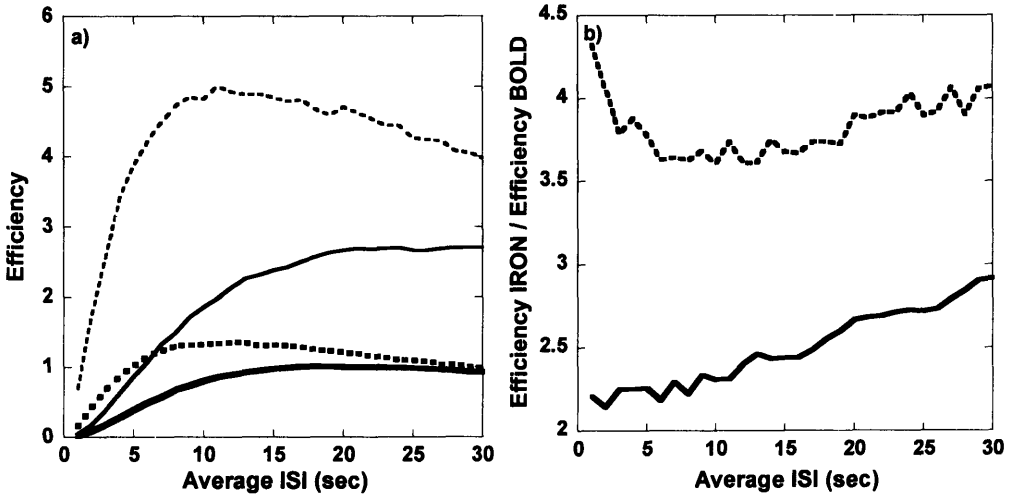

Fig. 3.2. Simulation Results. a) Plot of detection efficiency versus average ISI. Solid lines represent fixed designs, and dashed lines represent random designs. BOLD curves are thicker than IRON curves. b) Plot of the ratio of detection efficiency of IRON signal to detection efficiency of BOLD signal, as a function of the average ISI. Randomization of the ISIs improves detection efficiency for both BOLD and IRON methods as the average ISI decreases, but the improvement is more pronounced for the IRON method.

3.4 Results

3.4.1 Simulations

Fig. 3.2 shows the predicted effects of the different BOLD and IRON response shapes on detection efficiency. Detection efficiency decreases for fixed designs as the average ISI decreases, a result shown previously using BOLD signal (Bandettini and Cox, 2000). The same is observed using IRON for fixed designs. Randomization of the designs improves sensitivity at short ISIs for BOLD (Birn et al., 2002) and IRON methods, but it is predicted to be more favorable with the slower IRON response. This is easily observed from the behavior of the ratio of detection efficiency for IRON over BOLD as a function of the average ISI. For fixed designs this ratio decreases steadily as ISI decreases, but for randomized designs the ratio is always higher and increases as ISI gets smaller then 10 seconds.

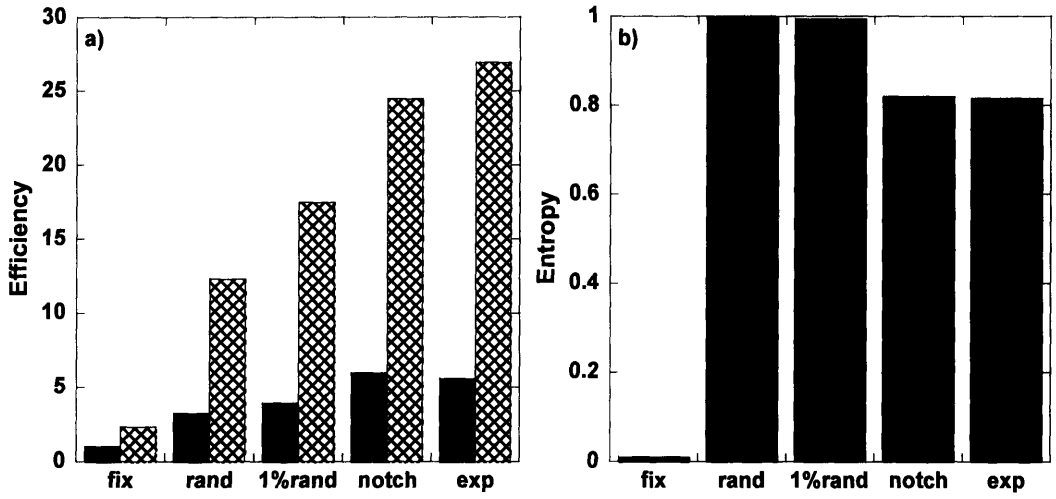

Fig. 3.3 Simulation results. a) Detection efficiency for BOLD (black) and IRON (diagonal grid) signal increases as one moves from fixed designs, to random designs, and to semi-random designs. b) The opposite trend is observed for entropy. While entropy and efficiency are generally inversely correlated, they are in fact independent parameters.

The average gain in efficiency of IRON with respect to BOLD for random designs is close to 3.8. Ordering the random designs as a function of increasing efficiency and selecting the 1% bin with best efficiency further increases the efficiency of both methods. Fig. 3.3 shows that for our choice of conditions, the gain in detection efficiency of the best 1% relative to the average gain is on the order of 40% for IRON and 20% for BOLD, and the gain in efficiency of IRON with respect to BOLD goes up to 4.5 for the best 1% bin. To ascertain if this selection has a negative effect in the predictability of the designs, we calculated the Shannon Entropy. The resulting normalized Shannon entropy was larger than 0.99, even for the 1% bin of runs with best detection

efficiency. Hence, randomized designs that maximize detection efficiency are still almost completely unpredictable.

Notch semi-random designs further enhance the detection efficiency of both methods, but a small concomitant increase in predictability also occurs, with entropy remaining close to 80% of the maximum theoretical value. With respect to fixed designs, the increase in efficiency was 10.8 for IRON and 5.9 for BOLD. When the entropy of an exponential ISI distribution was matched to the notch distribution, efficiencies were slightly smaller than the notch distribution for BOLD signal and slightly larger for IRON signal, again showing that entropy and detection efficiency are independent parameters, although stimulus designs often involve a tradeoff of these quantities.

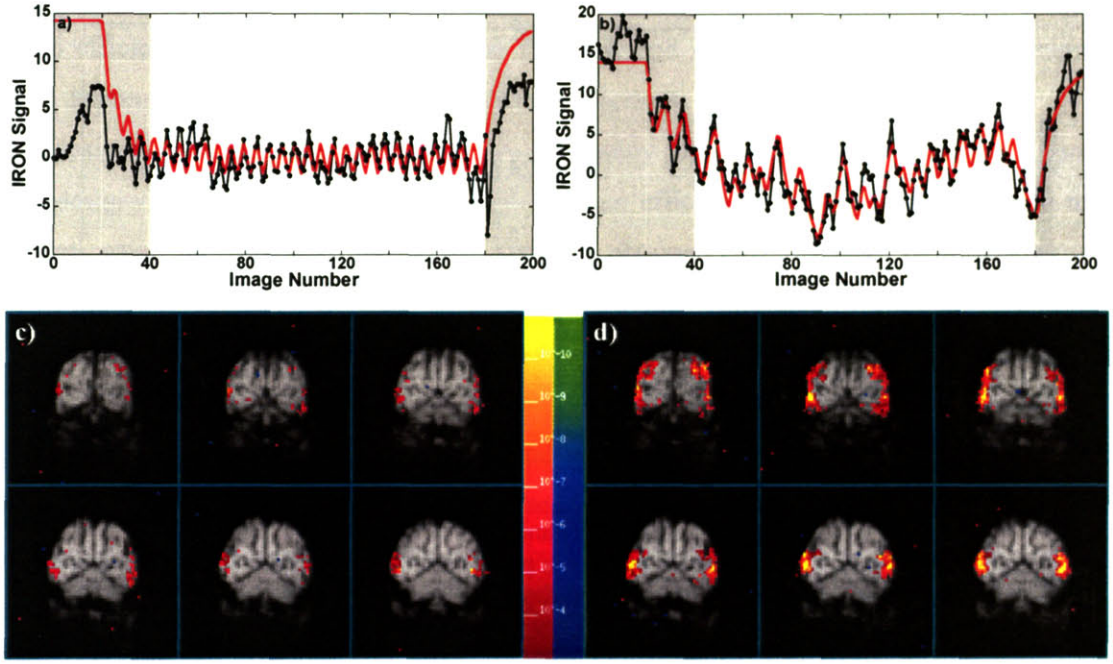

Fig. 3.4. Experimental results with IRON technique, for ISI_{av} = 4 sec. Representative temporal data (black) and GLM fit (red) after removal of baseline drift for a) fixed (average of 2 runs) and b) random designs (single run). Gray shaded regions were excluded by the filter matrix (Appendix). The corresponding activation maps are presented in c) and d). Maps show p-values and the scale is the same for both maps.

3.4.2 Experiments

Representative examples of IRON spatiotemporal data for fixed and random designs are presented in Fig. 3.4. The greater contrast observed in the randomized signal is reflected in the activation map by the higher number of voxels that reach significance. The same trend was observed with BOLD contrast, but as expected, the BOLD technique was found to be less sensitive overall than the IRON technique, even for these rapid ER paradigms. On average, the IRON method detected twice the number of activated voxels that were detected with the BOLD method across all conditions.

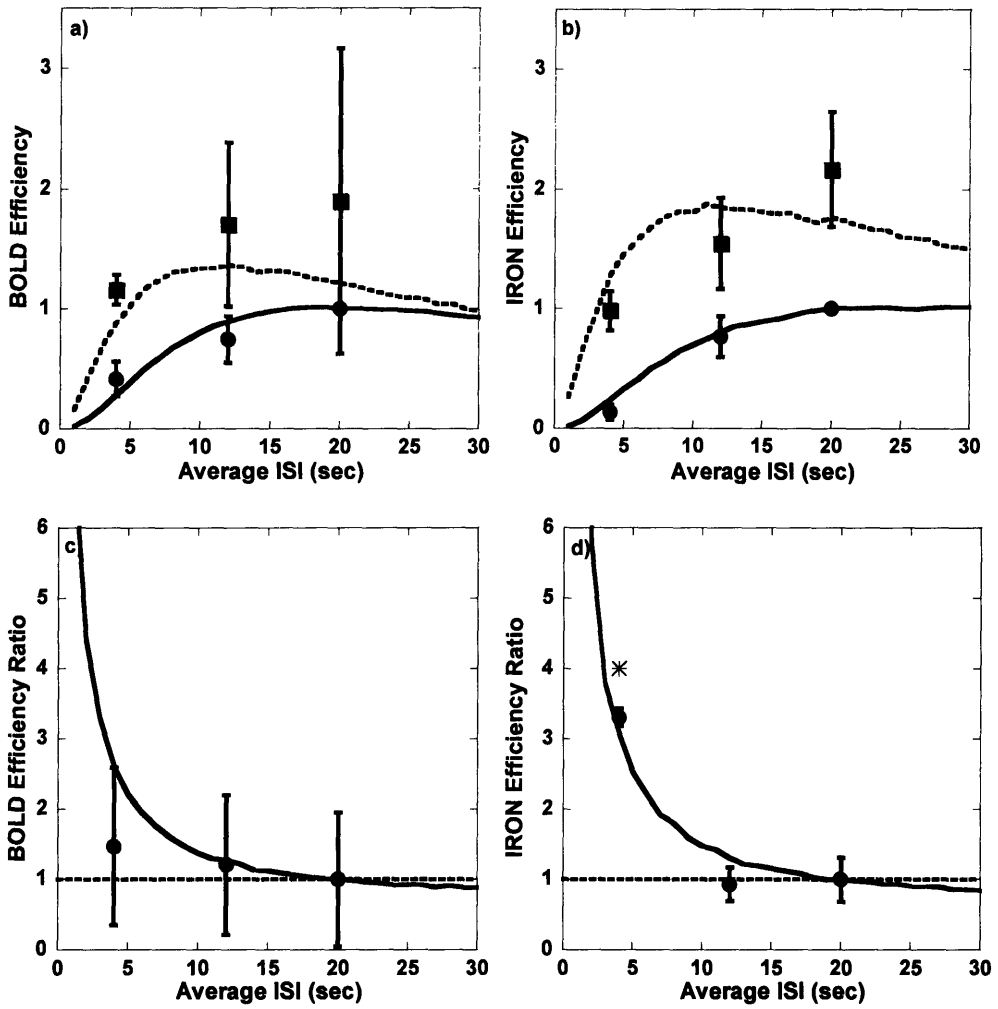

Fig. 3.5. Comparison of simulation results (lines) and experimental results (points), as a function of the average ISI. In a) BOLD, and b) IRON, square data points and dashed lines indicate random designs, and circular data points and solid lines represent fixed designs. Plots of the efficiency ratio of random designs to fixed designs as a function of the average ISI are presented in c) BOLD and d) IRON. All results are normalized with respect to the fixed value of efficiency (upper row) or efficiency ratio (bottom row) at 20 sec ISI.

Fig. 3.5 shows a comparison between the experimental results (mean±sem, averaged across magnet sessions) and simulated predictions. For both BOLD and IRON experiments the experimental results are in good agreement with the simulations, generally within one standard deviation from the theoretical curves. All points were normalized to the efficiency of the fixed design with ISI = 20 sec. The bottom row of Fig. 3.5 presents graphs of the efficiency ratio between random and fixed designs as a function of average ISI for BOLD and IRON. All results were normalized to the efficiency ratio at ISI = 20 sec. For the BOLD technique, none of the results were significantly different from one. For the IRON technique, the gain of the random

designs with respect to the fixed designs at the shortest average ISI was four times the gain achieved for the larger average ISIs tested, and this result achieves statistical significance.

3.5 Discussion

ER designs attempt to mitigate confounds arising from neural habituation and expectancy by using interleaved stimuli of short duration with unpredictable order and interval. Despite many desirable psychophysical characteristics, ER techniques suffer degradation in detection efficiency because the IRF acts as a low pass filter attenuating the size of the differential fMRI responses for rapidly presented stimuli. Because the temporal response of blood plasma is slower than the deoxyhemoglobin response, we hypothesized that IRON detection power would benefit more from random or certain semi-random designs. Simulations quantified the relative gain in detection efficiency under the assumption of linearity, and experiments in awake non-human primates demonstrated good agreement with these predictions.

ER designs with fixed ISI have both low efficiency and maximum predictability. Semi-random designs can be evaluated as a tradeoff between efficiency and predictability, such that significant gains in detection efficiency can be obtained by relaxing requirements on predictability as noted previously (Liu et al., 2001; Liu and Frank, 2004). Simulations suggest that large improvements in sensitivity can be achieved for both BOLD and IRON methods by moving from random designs to semi-random designs, albeit with modest reductions in entropy.

A good agreement between experiments and simulations was found for both BOLD and IRON methods. It was once again evident that the IRON method affords better sensitivity at this field strength for any design type. Relative to fixed designs, randomization of ISIs appeared to clearly enhance sensitivity for BOLD and IRON methods. Nonetheless, probably due to a relatively large intersession variance, only the randomized IRON paradigms at the shortest average ISI obtained significantly elevated efficiency relative to the corresponding fixed design. For very short ISIs, the IRON method should suffer less from sensitivity losses than the BOLD method, provided some sort of ISI randomization is employed.

While a systematic study of regional IRFs has not been performed in this model, regional variations appear to be small compared to the pronounced difference between BOLD and IRON IRFs. For this reason, and to reduce sensitivity to motion artifact, this study employed fixed IRF shapes to characterize and evaluate BOLD and IRON stimulus designs. However, results clearly emphasize the importance of the IRF shape in ER studies, and further work is warranted to explore regional variations in hemodynamics using unbiased estimators of the IRF (Burock and Dale, 2000).

The relationship between stimulus duration and the BOLD response has been extensively studied (Friston et al., 1998b; Vasquez and Noll, 1998; Glover, 1999; Birn et al., 2001; Boynton and Finney, 2003; Pfeuffer et al., 2003). Generally, responses to long duration stimuli can be predicted approximately as time-shifted summations of the responses to shorter stimuli of about 4 sec or longer in duration, whereas very brief stimuli produce larger responses than predicted from a linear model. The nonlinearity in BOLD signal can arise from nonlinearities between the stimulus and the neural response, the neural response and the hemodynamics, or both. Studies simultaneously measuring electrical activity and hemodynamic responses to stimuli, have shown that different metrics of the neural response vary with the hemodynamic response in an approximately linear manner over a restricted dynamic range (Ngai et al., 1999; Logothetis et al., 2001; Sheth et al., 2003; Hewson-Stoate et al., 2005), whereas a wider dynamic range reveals a power law (Devor et al., 2003; Sheth et al., 2004) or inverse sigmoidal (Jones et al., 2004) relationship between electrical activity and the hemodynamic response.

BOLD nonlinearities can also be exclusive to the complex hemodynamics producing this signal. CBF, as measured by arterial spin labeling, has been found to be more linear in the temporal domain than BOLD signal in certain brain regions, consistent with the notion that a major source of BOLD nonlinearity is the finite headroom for changes in deoxyhemoglobin concentration (Mechelli et al., 2001; Miller et al., 2001), an issue that does not arise for measurements of CBF or CBV. Indeed, optical studies have shown that integrated field potentials have a concordance with CBV greater than with oxygen-related signals (Nemoto et al., 2004). Although no IRON fMRI studies have explicitly investigated neural response linearity, the general linear model has proven to accurately describe data in a wide variety of stimulus paradigms (Leite et al., 2002). The present study again reinforces the utility of the linear approximation for BOLD and IRON techniques.

3.6 Appendix

3.6.1 General Linear Model (GLM) with finite impulse response (FIR) estimators

The forward model for the fMRI signal, y, in the linear regime is given by

$$\mathbf{y} = \mathbf{Xh} + \mathbf{n}. \tag{3.3}$$

$\mathbf{y}$ is a $N \times 1$ vector, $\mathbf{X}$ is a $N \times k$ stimulus convolution matrix (including $N \times 1$ matrix with nuisance model functions), $\mathbf{h}$ is a $k \times 1$ vector with the impulse response function coefficients (including 1 nuisance coefficients), and $\mathbf{n}$ is a $N \times 1$ noise vector. As is generally assumed, the covariance of the noise process is given by $\mathbf{C}_n = \sigma^2 \mathbf{I}$, where $\mathbf{I}$ is the identity matrix and σ^2 is the

variance. This formalism has been described in detail elsewhere (Friston et al., 1995; Dale, 1999; Liu et al., 2001).

Filtering of the fMRI signal is sometimes advantageous: if $\mathbf{X} \rightarrow \mathbf{IX}$ then $\mathbf{y} \rightarrow \mathbf{Iy}$, and the inverse model is given by

$$\mathbf{h} = \left[(\mathbf{IX})^T(\mathbf{IX})\right]^{-1}(\mathbf{IX})^T\mathbf{Iy}. \tag{3.4}$$

In this paper we chose **I**, or inclusion matrix, to exclude the initial and final parts of the signal vector, where the average signal goes from zero to a new steady-state due to long range contributions from the tail of the IRF. This strategy eliminates regimes where the most important contribution for CNR comes from a DC offset between baseline and stimulus periods. In this way, comparisons of a single condition to the baseline state accurately represent 2-event paradigms of long duration.

3.6.2 Detection Power and Estimation Efficiency

Detection power is defined as the capability to differentiate between the null hypothesis (no signal is present), and the alternative hypothesis (a signal is present), as determined by an F-statistic with N' – k degrees of freedom, where N' is the trace of **I**:

$$F = (N'-k)\frac{(\mathbf{ch})^T\left[\mathbf{c}\left((\mathbf{IX})^T(\mathbf{IX})\right)^{-1}\mathbf{c}^T\right]^{-1}(\mathbf{ch})}{\sigma^2}. \tag{3.5}$$

The contrast **c** is a vector that specifies which conditions are being compared or tested against baseline.

ER designs are a helpful tool in the identification of nuances in the shape of hemodynamic response functions. This task is facilitated by employing unbiased IRFs, but these functions are much less robust against motion, and are not a particularly good choice in the present study. The measure of the ability to estimate the hemodynamic IRF in the absence of a priori assumptions about its shape is called estimation efficiency, and is inversely proportional to the variance of $\hat{\mathbf{h}}$. Estimation efficiency is not dependent on the shape of the IRF (Dale, 1999) and is therefore not addressed in this study.

In the limit where the shape of the hemodynamic IRF does not vary, only the estimates of the activation amplitudes are important, and estimation efficiency and detection power are equivalent quantities (Birn et al., 2002), simply designated as efficiency or detection efficiency in this manuscript. Also, in this case, the F-test is just the square of the T-test, or in other words, detection efficiency equals the square of the contrast-to-noise ratio. While CNR varies with the square root of time, detection efficiency is linear with time, i.e., the efficiency per unit of time

with which a design reveals activation is inversely proportional to the duration of scanning required to achieve a fixed statistical power.

3.7 References

Bandettini PA, Cox RW, 2000. Event-related fMRI contrast when using constant interstimulus interval: theory and experiment. Magn Reson Med 43(4): 540-8.

Birn RM, Saad ZS, Bandettini PA, 2001. Spatial heterogeneity of the nonlinear dynamics in the FMRI BOLD response. Neuroimage 14(4): 817-26.

Birn RM, Cox RW, Bandettini PA, 2002. Detection versus estimation in event-related fMRI: choosing the optimal stimulus timing. Neuroimage 15(1): 252-64.

Boynton GM, Engel SA, Glover GH, Heeger DJ, 1996. Linear systems analysis of functional magnetic resonance imaging in human V1. J Neurosci 16: 4207-4221.

Boynton GM, Finney EM, 2003. Orientation-specific adaptation in human visual cortex. J Neurosci 23(25): 8781-7.

Buckner RL, Bandettini PA, O'Craven KM, Savoy RL, Petersen SE, Raichle ME, Rosen BR, 1996. Detection of cortical activation during averaged single trials of a cognitive task using functional magnetic resonance imaging. Proc Natl Acad Sci U S A 93(25): 14878-83.

Buracas GT, Boynton GM, 2002. Efficient design of event-related fMRI experiments using M-sequences. Neuroimage 16(3 Pt 1):801-13.

Burock MA, Buckner RL, Woldorff MG, Rosen BR, Dale AM, 1998. Randomized event-related experimental designs allow for extremely rapid presentation rates using functional MRI. Neuroreport 9(16): 3735-9.

Burock MA, Dale AM, 2000. Estimation and detection of event-related fMRI signals with temporally correlated noise: a statistically efficient and unbiased approach. Hum Brain Mapp 11(4): 249-60.

Cohen MS, 1997. Parametric analysis of fMRI data using linear systems methods. Neuroimage 6(2): 93-103.

Cover TM, Thomas JA, 1991. Elements of Information theory. Wiley, USA.

Cox RW, Hyde JS, 1997. Software tools for analysis and visualization of FMRI data. NMR in Biomedicine 10: 171-178.

Dale AM, Buckner RL, 1997. Selective averaging of rapidly presented individual trials using fMRI. Hum Brain Mapp 5: 329-40.

Dale AM, 1999. Optimal experimental design for event-related fMRI. Hum Brain Mapp 8(2-3): 109-14.

Devor A, Dunn AK, Andermann ML, Ulbert I, Boas DA, Dale AM, 2003. Coupling of total hemoglobin concentration, oxygenation, and neural activity in rat somatosensory cortex. Neuron 39(2): 353-9.

D'Esposito M, Zarahn E, Aguirre GK, 1999. Event-related functional MRI: implications for cognitive psychology. Psychol Bull 125(1): 155-64.

Friston KJ, Holmes AP, Worsley KJ, Poline JP, Frith CD, Frackowiak RSJ, 1995. Statistical Parametric Maps in Functional Imaging: A General Linear Approach. Hum Brain Mapp 2: 189-210.

Friston KJ, Fletcher P, Josephs O, Holmes A, Rugg MD, Turner R, 1998a. Event-related fMRI: characterizing differential responses. Neuroimage 7(1): 30-40.

Friston KJ, Josephs O, Rees G, Turner R, 1998b. Nonlinear event-related responses in fMRI. Magn Reson Med 39(1): 41-52.

Friston KJ, Zarahn E, Josephs O, Henson RN, Dale AM, 1999. Stochastic designs in event-related fMRI. Neuroimage 10(5): 607-19.

Glover GH, 1999. Deconvolution of impulse response in event-related BOLD fMRI. Neuroimage 9(4): 416-29.

Hewson-Stoate N, Jones M, Martindale J, Berwick J, Mayhew J, 2005. Further nonlinearities in neurovascular coupling in rodent barrel cortex. Neuroimage 24(2): 565-74.

Jones M, Hewson-Stoate N, Martindale J, Redgrave P, Mayhew J, 2004. Nonlinear coupling of neural activity and CBF in rodent barrel cortex. Neuroimage 22(2): 956-65.

Josephs O, Turner R, Friston KJ, 1997. Event-related fMRI. Hum Brain Mapp 5: 243-48.

Josephs O, Henson RN, 1999. Event-related functional magnetic resonance imaging: modelling, inference and optimization. Philos Trans R Soc Lond B Biol Sci 354(1387): 1215-28.

Leite FP, Tsao D, Vanduffel W, Fize D, Sasaki Y, Wald LL, Dale AM, Kwong KK, Orban GA, Rosen BR, Tootell RB, Mandeville JB, 2002. Repeated fMRI using iron oxide contrast agent in awake, behaving macaques at 3 Tesla. Neuroimage 16(2): 283-94.

Leite FP, Mandeville JB, 2003. Event-related BOLD vs IRON. Proceedings of the 11th ISMRM Meeting, Toronto, Canada, p. 213.

Liu TT, Frank LR, Wong EC, Buxton RB, 2001. Detection power, estimation efficiency, and predictability in event-related fMRI. Neuroimage 13(4): 759-73.

Liu TT, Wong EC, Frank LR, Buxton RB, 2002. Analysis and design of perfusion-based event-related fMRI experiments. Neuroimage 16(1): 269-82.

Liu TT, Frank LR, 2004. Efficiency, power, and entropy in event-related FMRI with multiple trial types. Part I: theory. Neuroimage 21(1): 387-400.

Logothetis NK, Pauls J, Augath M, Trinath T, Oeltermann A, 2001. Neurophysiological investigation of the basis of the fMRI signal. Nature 412(6843): 150-7.

Mandeville JB, Marota JJ, Kosofsky BE, Keltner JR, Weissleder R, Rosen BR, Weisskoff RM, 1998. Dynamic functional imaging of relative cerebral blood volume during rat forepaw stimulation. Magn Reson Med 39(4): 615-24.

Mandeville JB, Marota JJ, Ayata C, Zaharchuk G, Moskowitz MA, Rosen BR, Weisskoff RM, 1999. Evidence of a cerebrovascular postarteriole windkessel with delayed compliance. J Cereb Blood Flow Metab 19(6): 679-89.

Mechelli A, Price CJ, Friston KJ, 2001. Nonlinear coupling between evoked rCBF and BOLD signals: a simulation study of hemodynamic responses. Neuroimage 14(4): 862-72.

Miller KL, Luh WM, Liu TT, Martinez A, Obata T, Wong EC, Frank LR, Buxton RB, 2001. Nonlinear temporal dynamics of the cerebral blood flow response. Hum Brain Mapp 13(1): 1-12.

Nemoto M, Sheth S, Guiou M, Pouratian N, Chen JW, Toga AW, 2004. Functional signal- and paradigm-dependent linear relationships between synaptic activity and hemodynamic responses in rat somatosensory cortex. J Neurosci 24(15): 3850-61.

Ngai AC, Jolley MA, D'Ambrosio R, Meno JR, Winn HR, 1999. Frequency-dependent changes in cerebral blood flow and evoked potentials during somatosensory stimulation in the rat. Brain Res 837(1-2): 221-8.

Pfeuffer J, McCullough JC, Van de Moortele PF, Ugurbil K, Hu X, 2003. Spatial dependence of the nonlinear BOLD response at short stimulus duration. Neuroimage 18(4): 990-1000.

Rosen BR, Buckner RL, Dale AM, 1998. Event-related functional MRI: past, present, and future. Proc Natl Acad Sci USA 95(3): 773-80.

Shen T, Weissleder R, Papisov M, Bogdanov A Jr, Brady TJ 1993. Monocrystalline Iron Oxide Nanocompounds (MION): Physiochemical Properties. Magn Reson Med 29: 599-604.

Sheth S, Nemoto M, Guiou M, Walker M, Pouratian N, Toga AW, 2003. Evaluation of coupling between optical intrinsic signals and neuronal activity in rat somatosensory cortex. Neuroimage 19(3): 884-94.

Sheth SA, Nemoto M, Guiou M, Walker M, Pouratian N, Toga AW, 2004. Linear and nonlinear relationships between neuronal activity, oxygen metabolism, and hemodynamic responses. Neuron 42(2): 347-55.

Vanduffel W, Fize D, Mandeville JB, Nelissen K, Van Hecke P, Rosen BR, Tootell RB, Orban GA, 2001. Visual motion processing investigated using contrast agent-enhanced fMRI in awake behaving monkeys. Neuron 32(4): 565-77.

Vazquez AL, Noll DC, 1998. Nonlinear aspects of the BOLD response in functional MRI. Neuroimage 7(2): 108-18.

Weissleder R, Elizondo G, Wittenberg K, 1990. Ultrasmall superparamagnetic iron oxide. Characterization of a new class of contrast agents for MR imaging. Radiology 175: 489-49.

Yang Y, Engelien W, Pan H, Xu S, Silbersweig DA, Stern E, 2000. A CBF-based event-related brain activation paradigm: characterization of impulse-response function and comparison to BOLD. Neuroimage 12(3): 287-97.

Zarahn E, Aguirre G, D'Esposito M, 1997. A trial-based experimental design for fMRI. Neuroimage 6(2): 122-38.

Chapter 4

Retinotopic Spatial Resolution of IRON and BOLD fMRI

4.0 Preface

What is the fMRI point spread function? We still don't know but we are getting closer by directly measuring the spread of the fMRI response to point-image stimuli.

Using a visual stimulus containing four spots located in the periphery of the visual field, where the V1 cortical magnification factor is smaller, we tried in vain to obtain activation maps in one monkey, Edgar, using BOLD contrast at 3 Tesla. One day we put Edgar in the 7 Tesla, and got this activation map:

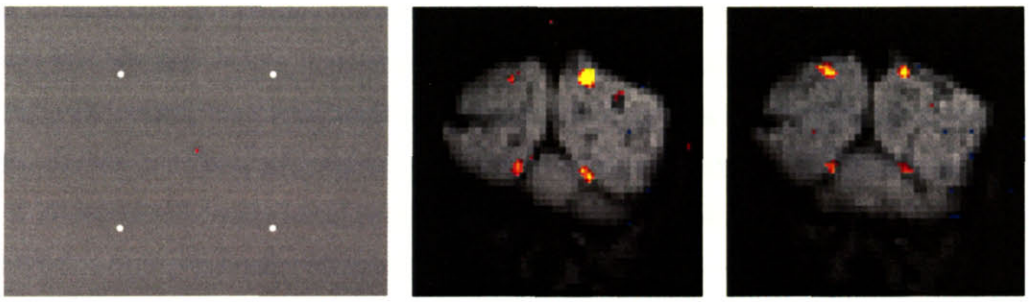

Figure 4.0. a) Typical stimulus. b) The anterior border of this slice was located approximately 7.5 mm anterior to the occipital notch.

Due to the improved sensitivity of the 7 Tesla magnet we could finally detect activation. These activation maps are now extremely reproducible, and we routinely obtain such maps using BOLD and IRON contrasts at 3 Tesla. Varying the diameter of the spots, we can estimate the PSF by extrapolating to infinitesimal small spot size. Nevertheless, the measured PSF is the result of the convolution of the real vascular PSF with additional blurring mechanisms: T_2^* decay or EPI phase encoding blurring, blurring due to motion-induced magnetic field distortions, and image resolution. Blurring coming from fluctuations in eye fixation effectively increase the cortical point image size. By estimating the relative contribution of these blurring mechanisms, we estimated the ultimate PSF that could be obtained in the absence of measurement errors.

4.1 Introduction

Precise and unconstrained measures of point spread functions (PSF) for IRON and BOLD contrast fMRI are still lacking. For imaging methods like fMRI that can detect different aspects of the vascular response to neuronal activation, the maximum achievable resolution will ultimately be limited by the anatomical and physiological spatial characteristics of the response measured. Additionally, the available signal-to-noise (SNR) and contrast-to-noise (CNR) ratios will set practical limits on the obtainable functional resolution, and factors like T_2^* decay, image distortions, among others, may induce blurring of the PSF.

The functional relationship between changes in brain function and metabolism was postulated in the late 19th century (e.g, Roy and Sherrington, 1890). A quantitative regional coupling between changes in blood flow and glucose metabolism was demonstrated by Sokoloff and colleagues (Sokoloff, 1981). However, the precise spatial resolution of any technique depends upon both the physics of the method and the physiological regulation of the measured variables. The latter has been a topic of ongoing controversy. Woolsey et al. (1996) showed that capillary tufts in layer IV of rodent whisker barrel were mainly coincident with barrels, and that this spatial matching optimized the local interactions between the functional neural unit and the capillary plexus. Harrison et al. (2002), based on their studies in the chinchilla, went further to suggest that a causal relationship between the metabolic demands of local neural activity and both the density of the capillary network and the placement of control structures exists. Furthermore, a great number of studies have recently shown that different metrics of the neural response correlate with different aspects of the hemodynamic response either in a linear fashion (Ngai et al., 1999; Logothetis et al., 2001; Sheth et al., 2003; Hewson-Stoate et al., 2005), following a power law (Devor et al., 2003; Sheth et al., 2004b) or an inverse sigmoidal (Jones et al., 2004), depending on the dynamic range considered.

The optimal hemodynamic response to detect neural activity is still under debate. During the 1990s, the most strongly advocate viewpoint, based upon flawed optical methods (Malonek and Grinvald, 1996), was that an "initial dip" in oxygenation due to increased oxygen utilization preceded the hyperoxia due to a hyperemic response of CBF. Refined methods for separating the chromophores of oxygenated and deoxygenated hemoglobin suggested that this feature of the BOLD response either vanished completely (Lindauer et al., 2001) or nearly (Jones et al., 2001), relative to the positive BOLD response.

As the existence and magnitude of the "initial dip" have been called into question, the spatial specificity of the CBV response to function activation has received renewed attention. Some groups have claimed that CBV related optical signals have a higher fidelity to the integral over

time of evoked potentials than oxygenation derived signals (Nemoto et al., 2004) and that total Hb images provided smaller activation areas than oxy- or deoxyhemoglobin signals (Siegel et al., 2003; Culver et al., 2005), while others have found that the spatial extent of the change in deoxyhemoglobin is smaller than that of oxyhemoglobin, total hemoglobin, CBF and $CMRO_2$ (Thompson et al., 2003; Dunn et al., 2005; Thompson et al., 2005). Nevertheless, both CBV and early oxygenation responses may extend beyond the anatomical boundaries of the active functional units (Grinvald et al., 1994; Sheth et al., 2004a; Devor et al., 2005). Presumably, the hemodynamic response is a spatiotemporal convolution of the neural activation: a positive hemodynamic response in one region might include contributions from neighboring regions, although the spatial spread of the hemodynamic response is not well know. Devor and colleagues (2005) demonstrated that oxy- and total hemoglobin hemodynamic responses can be well approximated by space-time separable functions with an antagonistic center-surround spatial pattern extending over *several millimeters*, and that the surround negative hemodynamic activity did not correspond to observable changes in the neural activity.

Engel and colleagues used common retinotopic stimuli (expanding checkerboard rings and rotating checkerboard wedges) to evaluate the spatial precision of BOLD fMRI at 1.5 T (Engel et al., 1997). They found that the BOLD spatial resolution was consistent with a linespread whose FWHM was 3.5 mm. Recently, preliminary experiments using the same approach but performed at 9.4 T in anesthetized cats, found point spread functions for BOLD and CBF in the range of 1.6 mm and 0.5 mm, respectively (Olman et al., 2004; Park et al., 2004; Park et al., 2005).

In the fMRI field, many groups have claimed to achieve columnar resolution (Menon et al., 1997; Menon et al., 1999; Duong et al., 2000; Kim et al., 2000; Duong et al., 2001; Cheng et al., 2001; Zhao et al., 2005), but only Cheng and Zhao demonstrated reproducibility of the results. Cheng and colleagues used the regular BOLD signal to achieve an in-plane resolution of 0.47 mm in visual cortex, detecting ocular dominance columns of approximately 1 mm width. Zhao and colleagues used IRON contrast at 9.4 T in anesthetized cats to achieve an in-plane resolution of 156 μm, and inferred that CBV regulates at a submillimeter columnar scale. They measured average distances between iso-orientation domains of approximately 1.4 mm and 1.7 mm in two orthogonal directions. Nevertheless, these techniques are limited by the spatial extent of the neuronal structures stimulated.

While the measured PSFs for BOLD and IRON contrast appear to be of the same order of magnitude, experiments in anesthetized macaque monkeys have shown that the spread of functional activity into a visual cortical area corresponding to an artificial scotoma appeared to be markedly greater for IRON than for BOLD contrasts (Schmid et al., 2004).

We have introduced a novel parametric approach, not limited by functional boundaries or vascular topology, with the goal of measuring the point spread functions of BOLD and IRON fMRI in awake, behaving macaque monkeys. We employed point-image stimuli to determine the full width at half maximum of the activated patches in V1, and compared BOLD and IRON point-image activity, and activity observed in the areas of the primary visual cortex that corresponded to holes in a full-field checkerboard stimulus. Our preliminary results in awake, behaving macaque monkeys indicated similar PSFs for BOLD and IRON contrasts, no larger than approximately 2 mm (Leite et al., 2004, 2005).

4.2 Methods

4.2.1 Animal Model

All experiments were performed at the Massachusetts General Hospital according to NIH and Institutional animal care guidelines, following the general procedures as described previously (Leite et al., 2002).

Two monkeys were trained to perform a high acuity fixation task while visual stimuli were presented in the background. Infrared eye tracking (DQW1_10 Version 1.10L, ISCAN, Inc. 1990-2004) was performed at all times. Horizontal and vertical pupil positions were recorded at 120 Hz, and water rewards discontinued if the pupil positions were consistently outside a pre-defined box centered at the fixation point. The box dimensions were chosen just large enough (smaller than $1^\circ \times 1^\circ$) to tolerate noise from the eye-tracker apparatus. On average, monkeys fixated accurately about 90% of the time.

The IRON studies employed a monocrystalline iron oxide nanoparticle (MION) contrast agent (Weissleder et al., 1990; Shen et al., 1993). The MION solution, containing an iron dose of 8 - 10 mg/kg, was injected in the femoral vein below the knee just prior to each scanning session.

4.2.2 Visual Stimulation

The visual stimuli were projected from an LCD projector onto a screen which was positioned approximately 55 cm in front of the monkey's eyes. The stimulus covered a visual field of approximately $21^\circ \times 24^\circ$, and the fixation point ($0.2^\circ \times 0.2^\circ$) was presented in the center of the screen at all times.

Three different stimuli were shown in block designs, each condition lasting 32 secs. The stimuli were alternating black and white spots on a gray background, alternating black and white full-field checkerboard, and gray holes on an alternating black and white full-field checkerboard, as shown in Fig. 4.1. The diameter of the spots and holes was varied across blocks, runs and

sessions, from 0.2° to 8° of visual angle, and the spots and holes were shown at eccentricities of 5°, 8° or 11°, along the 45° azimuth line in each visual quadrant. The flickering frequency was 3 Hz.

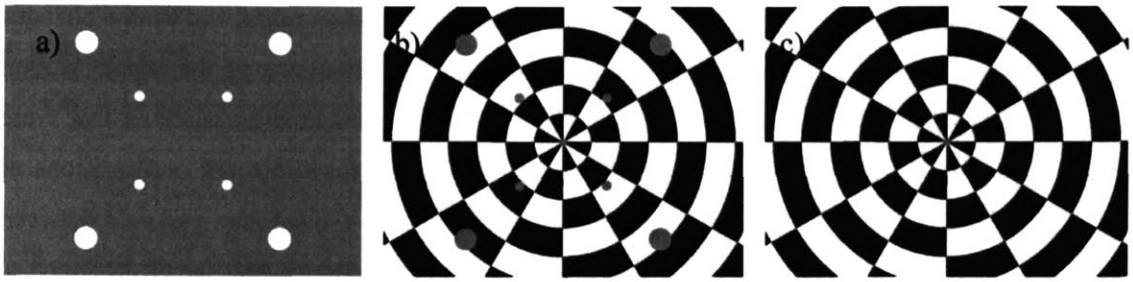

Fig. 4.1 Typical visual stimuli employed: a) alternating black and white spots on a gray background, and b) gray holes on a black and white alternating full-field checkerboard, and c) full-field checkerboard. The flickering frequency was 3 Hz. Baseline was an isoluminant gray screen. Both spots and holes were positioned in each quadrant of the visual field along the 45° azimuth line, and, in this case, at 5° and 11° degrees eccentricity. The eccentricity of the outer spots was chosen such that the activated cells would lie in the periphery of V1 where the receptive fields are smaller. The inner spots were scaled such that the area of the activated patches in V1 would be approximately equal to the area for the outer spots. Spot angular apertures between 0.2° and 8° of visual angle were used. A fixation point was present in the center of the screen at all times.

4.2.3 Magnetic Resonance Imaging

Experiments were performed in a 3 Tesla Siemens Allegra scanner (Siemens Medical System, Erlangen, Germany) using a custom surface coil for the radio frequency excitation and reception of signal. All functional imaging employed a single shot multislice echo planar imaging with an isotropic resolution of 1.25 mm. 15 slices were acquired using a repetition time of 1 sec and 90° flip angle. All BOLD and IRON studies employed a gradient echo time of 24 msec (the minimum achievable value for the selected resolution and sequence). In general, GE-EPI sequences were used, but a small number of experiments employed SE-EPI for comparison. Only IRON contrast was used with SE-EPI, due to IRON's better sensitivity even for the long echo times used.

In addition to functional imaging, data were acquired in each IRON session to enable the calculation of T_2^* maps by obtaining 9 gradient echo times from 24 to 64 msec at 5 msec intervals. These data were collected in the beginning and end of each IRON session, and were used to monitor IRON dose (Leite et al., 2002).

4.2.4 Data Analysis

We assumed the observed fMRI response is linear and time-invariant (Friston et al., 1995; Boynton et al., 1996; Dale and Buckner, 1997; Leite et al., 2002; Lu et al., 2005; Leite et al., 2006). Therefore, the fMRI signal was described using a general linear model (GLM) with

impulse response estimators of the hemodynamic response, as described in Leite et al. (2006). Hemodynamic IRFs for both BOLD and IRON methods were determined in a previous work (Leite et al., 2002).

Monkeys' body motion outside the field of view (FOV) induced temporal and spatial changes in the magnetic field that caused apparent translations and deformations of the brain. Motion correction using the AFNI algorithm (Cox and Hyde, 1997) eliminated translations that were uniform across the volume (e.g., due to drifts in scanner temperature) but not deformations or slice-specific translations. As an additional correction for motion, the residual variance between the target volume and each volume in the functional run was incorporated into the GLM analysis. The eye-tracker traces in x and y were included into the GLM analysis as explanatory variables.

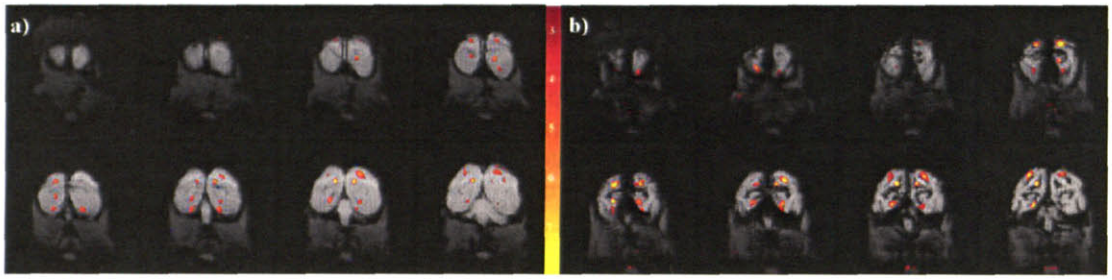

Fig. 4.2 Typical activation maps in consecutive posterior coronal slices of the monkeys' visual cortex obtained with spots' stimulus pattern, for a) IRON and b) BOLD contrasts. The activation maps are $-\log_{10}$(p-value) maps and the color scale is the same for both methods of contrast. The stimulus spots presented at 11° eccentricity correspond to the activity patches situated in the inner V1 surface, consistent with a stimulus eccentricity greater than 9°. The activated patches for the 5° eccentricity spots can be seen in the outer V1 surface in the most posterior slices: for example, the two bottom spots in slice 2 of IRON are the upper field representation of the 5° stimulus spots, while the two spots at the top of slice 4 are the lower visual field representation of these spots. These maps were obtained by concatenating the best fixation runs across diameters up to 1.8°.

Runs in each sessions were concatenated together, and a region of interest (ROI) that corresponded to the spots' activation patches in V1 was defined as all voxels with p-values below the Bonferroni-corrected p-value (a false positive rate of 10^{-4} was corrected for 15 slices with 64 by 64 pixels each). Separate activation maps for spots, holes and full-field were obtained, for every angular aperture used. The CNR was determined as the T-statistic for signal change using each spot size. The full width at half maximum (FWHM) of activation for each spot size was determined by fitting a Gaussian function to the CNR distribution for each spot size, such that $\mathrm{FWHM} = 2\sigma\sqrt{2\ln 2}$, where σ is the Gaussian standard deviation. Within each session, the FWHM values were fit as a linear function of the spot size diameter to obtain an asymptotic prediction of the FWHM for a point stimulus.

Additional blurring factors were accounted for and deconvolved from the measured PSF for each method of contrast, thus determining an upper bound for the "true" PSFs for BOLD and IRON fMRI.

4.3 Results

Fig. 4.1a shows a typical point-image stimulus, used to parametrically measure the PSF, and in Fig. 4.2 the corresponding activation maps in consecutive coronal slices of the monkey's visual cortex, using BOLD and IRON contrasts, are presented. The activation maps are very similar for both methods of contrast. The stimulus spots presented at 11° eccentricity correspond to the activity patches situated in the inner V1 surface, consistent with a stimulus eccentricity greater than 9°. The activated patches for the 5° eccentricity spots can be seen in the outer V1 surface in the most posterior slices. V2 spots start to be seen in more anterior slices in both BOLD and IRON maps. These maps were obtained by concatenating the best fixation runs up to a diameter of 1.8° of visual angle, and where extremely reproducible.

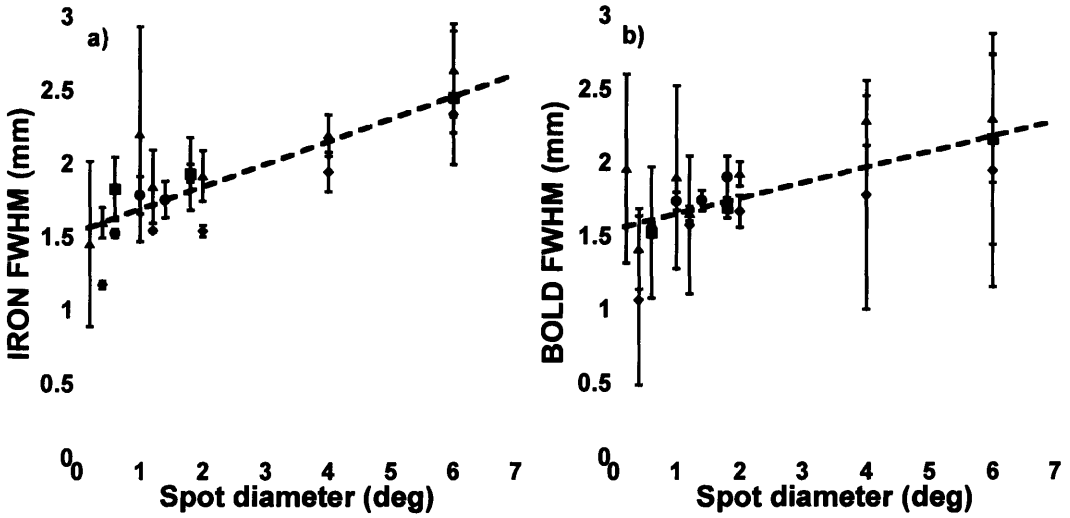

Fig. 4.3 Plots of FWHM vs diameter of spots, d, for all sessions in two monkeys for a) IRON and b) BOLD. Linear fits to the data give a) FWHM(d) = 0.1534d + 1.5173 with R^2 = 0.7 and b) FWHM(d) = 0.1058d + 1.5247 with R^2 = 0.5. The trends are similar for BOLD and IRON contrasts and differences are not statistically significant. The different symbols represent different groups of experiments. In each group, the eccentricity and diameter of spots were kept the same, and experiments were realized in the same monkey and across a short period of time, typically a few weeks.

The average FWHM of the retinotopic projections of the point stimuli on the visual cortex was determined by fitting a Gaussian distribution to each V1 spot in the CNR maps. As observed in Fig. 4.3, the area of the activation patches in the V1 increased linearly with the stimulus spot diameter. Linear fits to the data determined slopes of 0.15 and 0.11 for IRON and BOLD respectively, and a nearly identical offset of 1.5 mm for both methods. The trends observed in

IRON sessions were similar to BOLD sessions, but a greater number of spot sizes could be used in a typical IRON session, due to the better sensitivity of IRON contrast.

Monkey	Ecc (deg)	Spot *d* (deg)	Num of sessions	Slope		Intercept		R^2	
				IRON	BOLD	IRON	BOLD	IRON	BOLD
A	5, 11	0.6, 1, 1.4, 1.8	2 IRON 2 BOLD	0.30	0.27	1.37	1.40	0.84	0.91
A	8	0.4, 1.2, 2, 4, 6	2 IRON 2 BOLD	0.19	0.13	1.16	1.24	0.97	0.73
B	5, 11	0.6, 1.8, 6	3 IRON 4 BOLD	0.12	0.12	1.72	1.45	0.99	0.99
B	8	0.2, 0.4, 1, 1.2, 2, 4, 6	3 IRON 3 BOLD	0.16	0.12	1.61	1.65	0.76	0.62

Table 4.1 Individual results for each group of experiments performed to measure the spots' FWHM, divided according to monkey and type of stimulus used. Typically the same number of BOLD and IRON sessions was performed. The slopes obtained for IRON contrast are slightly larger than for BOLD contrast, while the intercepts are not statistically different between the two methods of contrast. They are, on average, smaller for monkey A than for monkey B, perhaps due to the better quality of fixation of monkey A. Averaging the intercepts across the groups of experiments in the table, we get 1.465 ± 0.2 mm and 1.435 ± 0.115 mm.

The results for each different type of session are presented in Table 4.1. Linear fits showed high correlation coefficients in each case. In a given group, the characteristics of the particular stimulus and block design used were kept constant, and the same monkey was always scanned. The results obtained were similar for both methods of contrast and across groups of experiments. Averaged slopes were 0.19 ± 0.03 mm for IRON contrast, and 0.16 ± 0.03 mm for BOLD contrast. Averaged intercepts were 1.47± 0.10 mm for IRON contrast and 1.44 ± 0.07 mm for BOLD. The intercepts were, on average, smaller for monkey A than monkey B, likely due to monkey A's better fixation quality. IRON contrast experiments using SE-EPI and GE-EPI provided comparable results (not shown), but this similarity might be due to the long acquisition times used for SE-EPI, which induce gradient-echo weighting.

Holes in activation maps were not observed for small angular apertures for either method of contrast. In fact, the average signal at the expected location of the holes (the location of the spots) was larger than the average signal at the same location for spots, and similar to the signal for a full-field stimulus, as observed in Figs. 4.4 and 4.5a for angular apertures smaller than approximately 3° of visual angle. For larger angular apertures, holes still could not be observed directly in a consistent manner, but for both methods of contrast we could detect a decrease in CNR in the region of the holes. We could easily visualize the decrease in CNR in the holes' region by dividing the holes activation maps by the full-field activation maps, as it is shown for IRON contrast in Fig. 4.5b. In this way, we could detect reduced CNR in the expected regions

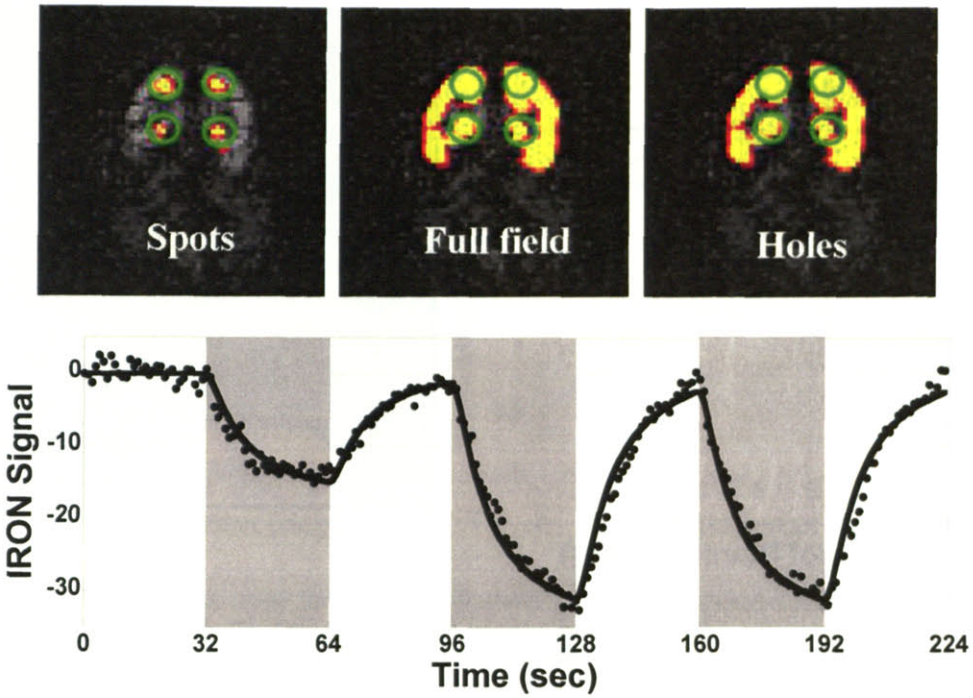

Fig. 4.4 Holes in activation maps were not observed for small angular apertures, smaller than 3° of visual angle, for any of the methods of contrast used. The average signal at the expected location of the holes was larger than the average signal at the same location for spots, and similar to full-field. IRON and BOLD contrast experiments provided equivalent results.

Plots of the PSF variation range before and after deconvolving considered blurring factors (T_2^* decay and pixel size) are presented in Fig. 4.6. The estimated upper bound for the "true" PSF is 0.4 mm and 0.8 mm for IRON and BOLD contrasts, respectively.

4.4 Discussion

Following a parametric approach not limited by the spatial extent of neuronal functional units or by vascular topology, we have found that fMRI in awake monkeys can reliably detect point stimuli as small as 0.2° during a single session. Our present estimate of the maximum spatial fMRI PSF in monkey V1 is no larger than 1.5 mm for IRON and BOLD contrast mechanisms. Hole-image and spot-image experiments provided similar results for BOLD and IRON fMRI in these studies.

A strong positive correlation between the size of the stimulus' spots and the correspondent activated patches in the primary visual cortex was observed, and the FWHM of the patches, comparable for both methods of contrast, was on the order of the image resolution. The results were highly reproducible across sessions.

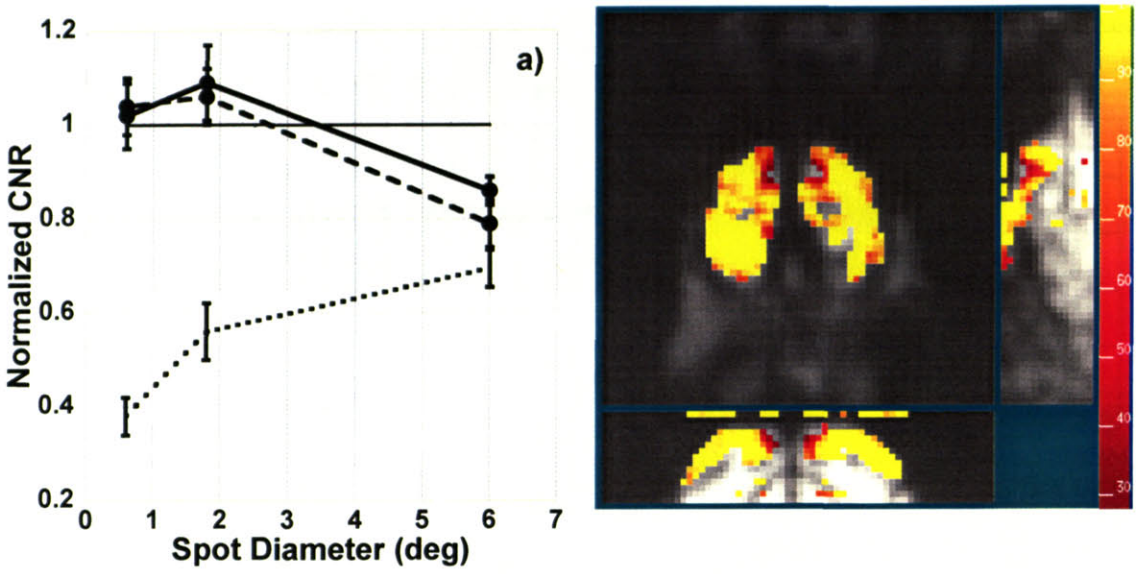

Fig. 4.5 a) Plot of normalized CNR within the spots' ROI vs spot diameter. For both methods of contrast, each CNR curve was normalized by the CNR for the full-field checkerboard, and the thin horizontal line indicates the full-field checkerboard normalized CNR for both BOLD and IRON. The thick solid line shows the normalized CNR for holes with BOLD contrast, while the dashed line is the correspondent line for IRON contrast. The dotted line represents the normalized CNR for spots averaged across contrasts. The trends observed for spots and holes are similar for BOLD and IRON contrasts, and differences are not statistically significant. b) A hole becomes noticeable in an activation map when its radius equals the mean FWHM for the contrast method used. The above figure was obtained using IRON fMRI, and shows the ratio between holes and full-field checkerboard activation maps. Due to image distortion, the holes in the lower part of the images were more difficult to detect.

Additional factors could contribute to a higher effective measurement of the point spread function: motion-induced image distortions, phase encoding blurring due to T_2^* decay, and fixation uncertainty.

On average, measures of the PSF in the readout direction and phase encoding direction were not different. Thus, motion-induced distortions, worse in the phase encoding direction, do not appear to contribute significantly to the blurring of the cortical point image. In fact, we believe that the main problem associated with motion distortions in our data is decreased detection power, because runs containing images that are significantly distorted are completely discarded.

BOLD and IRON contrasts have different blurring due to T_2^* decay, because injection of MION markedly reduces T_2^*. The PSF associated with this source of blurring is approximately given by $\left(T_{ACQ}/\pi T_2^*\right)\delta y$, where T_{ACQ} is the acquisition time and δy is the pixel size. The average relaxation times for BOLD and IRON methods, as reported in a previous work (Leite et al., 2002), were 48 msec and 22 msec, respectively. The acquisition time was approximately 42 msec for both methods of contrast. We estimated the phase encoding blurring to be approximately 0.4 mm for BOLD contrast and 0.8 mm for IRON contrast.

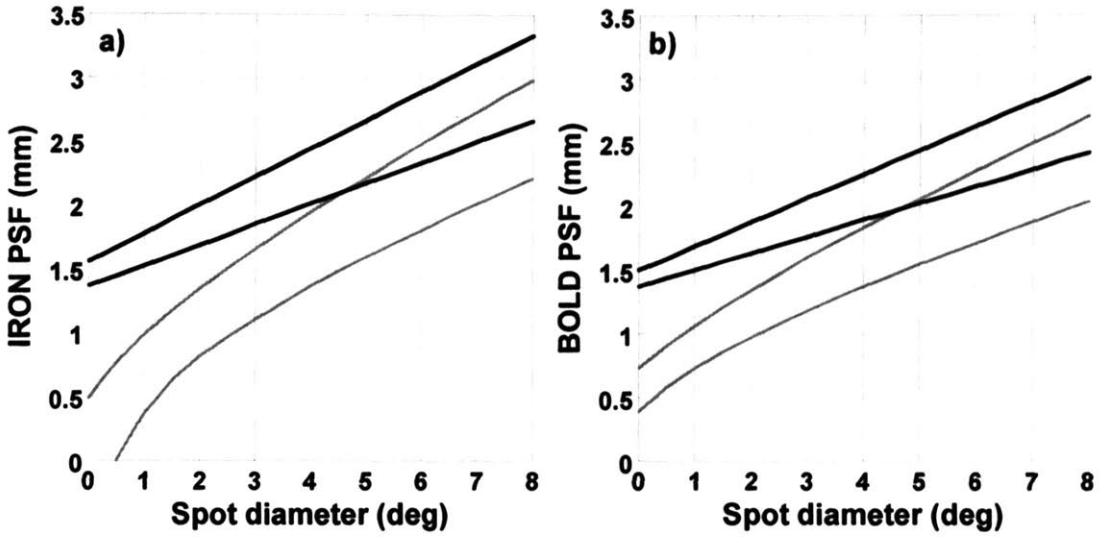

Fig. 4.6 Plots of PSF variation range for each spot diameter for a) IRON contrast and b) BOLD contrast. The measured PSF variation range is shown in black, and the variation range obtained by deconvolution of the measured PSF from the estimated blurring PSF is shown in gray.

The uncertainty associated with eye fixation will blur the retinal image of the spot, thus the cortical point image will be correspondingly larger. In other words, the fixation blurring increases the effective diameter of the stimulus' spots. We estimate that the fixation blurring will add an average uncertainty no larger than 1° to the diameter of the stimulus'spots.

In Fig. 4.6 we plotted the variation range of the corrected FWHM, as obtained by deconvolving the measured FWHM from the blurring functions associated with image resolution and T_2^* decay, versus the diameter of stimulus' spot size. In the same plot is also shown the measured variation range for comparison. From linear fits to the corrected data, the upper bound estimates for the "true" PSFs are approximately 0.8 mm for BOLD contrast and 0.4 mm for IRON contrast. Human data obtained from psychophysics experiments estimates the neuronal PSF to be 0.07 – 0.14 mm (Virsu et al., 1987). Our vascular PSF estimates are still considerably larger than the human reported values.

With respect to detection of holes, we found that the two methods behaved similarly in our awake model. The CNR in the region of the hole was indistinguishable from full-field checkerboard for both methods of contrast if the radius of the hole was smaller that the measured PSF. For radii larger than PSF, decreases in the contrast-to-noise ratio in the hole could be equally detected with IRON and BOLD contrasts.

Different factors could account for the filling in of the holes. For example, image distortions and fixation blurring might contribute to the fMRI activity detected in the holes in the awake animal, but these factors will contribute equally for BOLD and IRON images. Because primary

visual cortex functions as an edge localizer, a possible explanation to our observations could be that for the smallest apertures used, there is neuronal activity in the region of the hole. In agreement with this hypothesis, as the diameter of the holes increase, the activity will be more confined to the edges of the hole, consistent with the drop of signal observed for both methods for larger holes' radii.

Schmid and colleagues (Schmid et al., 2004) have shown that the lack of functional activity induced by an artificial scotoma could be observed with BOLD contrast but not with IRON contrast in isoflurane-anesthetized primates. We suggest that the difference between our results and Shmid's is due to anesthesia. Anesthetics increase basal blood oxygenation by decreasing $CMRO_2$ more than CBF; thus, BOLD sensitivity is compromised in the anesthetized state due to a decreased basal concentration of deoxygenated hemoglobin. As we have seen, CNR decreases in the region of the hole for BOLD and IRON contrasts. If BOLD sensitivity is already compromised due to anesthesia, a further drop in sensitivity would make the hole obvious with BOLD contrast sooner than it would with IRON contrast.

Our measured PSFs are mainly limited by the image resolution. To successfully achieve higher spatial resolution we are moving to multi-shot echo planar sequences, and strategies to reduce image distortions are being developed. The acquisition of undistorted images is also a crucial step in allowing accurate inter-session registration and for obtaining activation maps registered to flattened cortical surfaces (Fischl et al.,1999). While our measures of FWHM are likely different from the point spread functions determined from flat maps, due to the curvature and folding of the visual cortex, our main goal was to show they are comparable, independently on how they are measured.

4.5 References

Boynton GM, Engel SA, Glover GH, Heeger DJ, 1996. Linear systems analysis of functional magnetic resonance imaging in human V1. J Neurosci 16: 4207-4221.

Cheng K, Waggoner RA, Tanaka K, 2001. Human ocular dominance columns as revealed by high-field functional magnetic resonance imaging. Neuron 32(2): 359-74.

Cox RW, Hyde JS, 1997. Software tools for analysis and visualization of FMRI data. NMR in Biomedicine 10: 171-178.

Culver JP, Siegel AM, Franceschini MA, Mandeville JB, Boas DA, 2005. Evidence that cerebral blood volume can provide brain activation maps with better spatial resolution than deoxygenated hemoglobin. Neuroimage 27(4): 947-59.

Dale AM, Buckner RL, 1997. Selective averaging of rapidly presented individual trials using fMRI. Hum Brain Mapp 5: 329-40.

Devor A, Dunn AK, Andermann ML, Ulbert I, Boas DA, Dale AM, 2003. Coupling of total hemoglobin concentration, oxygenation, and neural activity in rat somatosensory cortex. Neuron 39(2): 353-9.

Devor A, Ulbert I, Dunn AK, Narayanan SN, Jones SR, Andermann ML, Boas DA, Dale AM, 2005. Coupling of the cortical hemodynamic response to cortical and thalamic neuronal activity. Proc Natl Acad Sci U S A 102(10): 3822-7.

Dunn AK, Devor A, Dale AM, Boas DA, 2005. Spatial extent of oxygen metabolism and hemodynamic changes during functional activation of the rat somatosensory cortex. Neuroimage 27(2): 279-90.

Duong TQ, Kim DS, Ugurbil K, Kim SG, 2000. Spatiotemporal dynamics of the BOLD fMRI signals: toward mapping submillimeter cortical columns using the early negative response. Magn Reson Med 44(2): 231-42.

Duong TQ, Kim DS, Ugurbil K, Kim SG, 2001. Localized cerebral blood flow response at submillimeter columnar resolution. Proc Natl Acad Sci U S A 98(19): 10904-9.

Engel SA, Glover GH, Wandell BA, 1997. Retinotopic organization in human visual cortex and the spatial precision of functional MRI. Cereb Cortex 7(2): 181-92.

Fischl B, Sereno MI, Dale AM, 1999. Cortical surface-based analysis. II: Inflation, flattening, and a surface-based coordinate system. Neuroimage 9(2): 195-207.

Friston KJ, Holmes AP, Worsley KJ, Poline JP, Frith CD, Frackowiak RSJ, 1995. Statistical Parametric Maps in Functional Imaging: A General Linear Approach. Hum Brain Mapp 2: 189-210.

Grinvald A, Lieke EE, Frostig RD, Hildesheim R, 1994. Cortical point-spread function and long-range lateral interactions revealed by real-time optical imaging of macaque monkey primary visual cortex. J Neurosci 14(5 Pt 1): 2545-68.

Harrison RV, Harel N, Panesar J, Mount RJ, 2002. Blood capillary distribution correlates with hemodynamic-based functional imaging in cerebral cortex. Cereb Cortex 12(3): 225-33.

Hewson-Stoate N, Jones M, Martindale J, Berwick J, Mayhew J, 2005. Further nonlinearities in neurovascular coupling in rodent barrel cortex. Neuroimage 24(2): 565-74.

Kim DS, Duong TQ, Kim SG, 2000. High-resolution mapping of iso-orientation columns by fMRI. Nat Neurosci 3(2): 164-9.

Jones M, Berwick J, Johnston D, Mayhew J, 2001. Concurrent optical imaging spectroscopy and laser-Doppler flowmetry: the relationship between blood flow, oxygenation, and volume in rodent barrel cortex. Neuroimage 13(6 Pt 1): 1002-15.

Jones M, Hewson-Stoate N, Martindale J, Redgrave P, Mayhew J, 2004. Nonlinear coupling of neural activity and CBF in rodent barrel cortex. Neuroimage 22(2): 956-65.

Leite FP, Tsao D, Vanduffel W, Fize D, Sasaki Y, Wald LL, Dale AM, Kwong KK, Orban GA, Rosen BR, Tootell RB, Mandeville JB, 2002. Repeated fMRI using iron oxide contrast agent in awake, behaving macaques at 3 Tesla. Neuroimage 16(2): 283-94.

Leite FP, Vanduffel W, Tootell RB, Mandeville JB, 2004. Point-image experiments in awake, behaving macaques. Proceedings of the 12th ISMRM Meeting.

Leite FP, Vanduffel W, Rosen BR, Mandeville JB, 2005. Comparing spatial resolution of IRON and BOLD in awake macaques. Proceedings of the 13th ISMRM Meeting.

Leite FP, Mandeville JB, 2006. Characterization of event-related designs using BOLD and IRON fMRI. Neuroimage 29(3): 901-9.

Lindauer U, Royl G, Leithner C, Kuhl M, Gold L, Gethmann J, Kohl-Bareis M, Villringer A, Dirnagl U, 2001. No evidence for early decrease in blood oxygenation in rat whisker cortex in response to functional activation. Neuroimage 13(6 Pt 1): 988-1001.

Logothetis NK, Pauls J, Augath M, Trinath T, Oeltermann A, 2001. Neurophysiological investigation of the basis of the fMRI signal. Nature 412(6843): 150-7.

Lu H, Soltysik DA, Ward BD, Hyde JS, 2005. Temporal evolution of the CBV-fMRI signal to rat whisker stimulation of variable duration and intensity: a linearity analysis. Neuroimage 26(2): 432-40.

Menon RS, Ogawa S, Strupp JP, Ugurbil K, 1997. Ocular dominance in human V1 demonstrated by functional magnetic resonance imaging. J Neurophysiol 77(5): 2780-7.

Menon RS, Goodyear BG, 1999. Submillimeter functional localization in human striate cortex using BOLD contrast at 4 Tesla: implications for the vascular point-spread function. Magn Reson Med 41(2): 230-5.

Nemoto M, Sheth S, Guiou M, Pouratian N, Chen JW, Toga AW, 2004. Functional signal- and paradigm-dependent linear relationships between synaptic activity and hemodynamic responses in rat somatosensory cortex. J Neurosci 24(15): 3850-61.

Ngai AC, Jolley MA, D'Ambrosio R, Meno JR, Winn HR, 1999. Frequency-dependent changes in cerebral blood flow and evoked potentials during somatosensory stimulation in the rat. Brain Res 837(1-2): 221-8.

Olman CA, Van de Moortele P-F, Ugurbil K, 2004. Point spread function for gradient echo and spin echo BOLD fMRI at 7 T. Proceedings of the 12th ISMRM Meeting.

Park JC, Ronen I, Toth LJ, Ugurbil K, Kim DS, 2004. Comparison of point spread functions of BOLD abd ASL fMRI at an ultra-high magnetic field, 9.4 T. Proceedings of the 12th ISMRM Meeting.

Park JC, Ronen I, Kim DS, Ugurbil K, 2005. Spatial specificity of high resolution gradient echo (GE) BOLD and spin echo (SE) BOLD fMRI in cat visual cortex at 9.4 T. Proceedings of the 13th ISMRM Meeting.

Roy CS, Sherrington CS, 1890. On the regulation of the blood-supply of the brain. J Physiol 11: 85-108.

Schmid MC, Tolias AS, Augath MA, Logothetis NK, Smirnakis SM, 2004. Spatial Resolution of BOLD versus MION in a macaque fMRI paradigm at 4.7 T. Proceedings of the 10th OHBM Meeting.

Shen T, Weissleder R, Papisov M, Bogdanov A Jr, Brady TJ 1993. Monocrystalline Iron Oxide Nanocompounds (MION): Physiochemical Properties. Magn Reson Med 29: 599-604.

Sheth S, Nemoto M, Guiou M, Walker M, Pouratian N, Toga AW, 2003. Evaluation of coupling between optical intrinsic signals and neuronal activity in rat somatosensory cortex. Neuroimage 19(3): 884-94.

Sheth SA, Nemoto M, Guiou M, Walker M, Pouratian N, Hageman N, Toga AW, 2004a. Columnar specificity of microvascular oxygenation and volume responses: implications for functional brain mapping. J Neurosci 24(3): 634-41.

Sheth SA, Nemoto M, Guiou M, Walker M, Pouratian N, Toga AW, 2004b. Linear and nonlinear relationships between neuronal activity, oxygen metabolism, and hemodynamic responses. Neuron 42(2): 347-55.

Siegel AM, Culver JP, Mandeville JB, Boas DA, 2003. Temporal comparison of functional brain imaging with diffuse optical tomography and fMRI during rat forepaw stimulation. Phys Med Biol 48(10): 1391-403.

Sokoloff L, 1981. Relationships among local functional activity, energy metabolism, and blood flow in the central nervous system. Fed Proc 40(8): 2311-6.

Thompson JK, Peterson MR, Freeman RD, 2003. Single-neuron activity and tissue oxygenation in the cerebral cortex. Science 299(5609): 1070-2.

Thompson JK, Peterson MR, Freeman RD, 2005. Separate spatial scales determine neural activity-dependent changes in tissue oxygen within central visual pathways. J Neurosci 25(39): 9046-58.

Virsu V, Nasanen R, Osmoviita K, 1987. Cortical magnification and peripheral vision. J Opt Soc Am A 4(8): 1568-78.

Weissleder R, Elizondo G, Wittenberg K, 1990. Ultrasmall superparamagnetic iron oxide. Characterization of a new class of contrast agents for MR imaging. Radiology 175: 489-49.

Woolsey TA, Rovainen CM, Cox SB, Henegar MH, Liang GE, Liu D, Moskalenko YE, Sui J, Wei L, 1996. Neuronal units linked to microvascular modules in cerebral cortex: response elements for imaging the brain. Cereb Cortex 6(5): 647-60.

Zhao F, Wang P, Hendrich K, Kim SG, 2005. Spatial specificity of cerebral blood volume-weighted fMRI responses at columnar resolution. Neuroimage 27(2): 416-24.

Chapter 5

Structure of Noise in IRON and BOLD fMRI

5.0 Preface

In this chapter we look at the structure of noise for BOLD and IRON contrasts. So far we have assumed we are capturing all the relevant temporal dynamics using a general linear model that includes the convolution of the stimulus paradigm with the measured impulse response functions, the time course of eye fixation, and the temporal evolution of the motion-induced image distortions. Now, we ask what lurks in the "noise", and if the different physiology of BOLD and IRON methods will reveal different contributions.

Firstly, we determined the noise autocorrelation in previous acquired data for block designs and event-related designs, and examined the spatial distribution of the first order autocorrelation coefficient for BOLD and IRON contrasts. Secondly, we acquired "resting state" data without stimuli, and examined the resulting frequency spectrum. Respiration and low frequency peaks were immediately identified. Modeling of the noise spectrum will likely aid in the identification of additional noise sources.

5.1 Introduction

Non averaged MRI signals are very noisy. Following a common formalism, total noise can be divided into three components:

$$\sigma = \sqrt{\sigma_T^2 + \sigma_S^2 + \sigma_P^2}\,, \tag{5.1}$$

where σ_T is thermal noise arising from subject and scanner electronics, σ_S is systematic noise, which describes other system noise that includes drift and imperfections in RF, gradient and shim subsystems, and σ_P is physiological noise. Physiological noise can arise from fluctuations in $CMRO_2$, CBF, CBV, from cardiac and respiratory functions that cause quasiperiodic oscillations in the vascular system, motion from subtle brain pulsatility, magnetic field modulations associated with motion, and low frequency fluctuations (LFOs) of unknown source (Biswal et al., 1996). The physiological noise is dependent on SNR, increasing with magnetic field strength, and decreasing with increasing image resolution (Triantafyllou et al., 2005 and 2006).

Physiological noise can be subdivided in two components, according to their TE-dependency. As this problem has been studied almost exclusively with BOLD signal, a so-called BOLD

component arises from fluctuations in R_2^*, giving rise to changes in signal. These fluctuations are closely linked to brain physiology, and are caused by the same mechanism that results in activation induced signal changes in BOLD contrast. A non-BOLD component arises from image-to-image signal fluctuations due to cardiac and respiratory functions and scanner imperfections, and is not TE-dependent. Its contribution is, in general, two times smaller than the contribution of the BOLD component.

The magnitude of noise fluctuations varies throughout the brain. Physiological noise is approximately two times stronger in gray matter than white matter, and the main contributor to the total noise. Furthermore, cardiac fluctuations are most prominent in regions with CSF and with large vessels (Hu et al., 1995). During respiration, susceptibility variations in the lungs cause fluctuations in the static magnetic field within brain tissue, which lead to a shift of the image and a shading of intensity in the phase-encoding direction (Raj et al., 2000; Raj et al., 2001; Birn et al., 2006). Respiration can also affect the fMRI time series by changing the arterial level of CO_2, a potent vasodilator. For each pixel, the respiratory noise was shown to account for approximately 10-20% of temporal variance at 1.5 T (Raj et al., 2001), increasing to 20-60% at 4 T (Hu et al., 1995). At 1.5 T, the low frequency fluctuations of unknown source were shown to dominate in gray and white matter (Biswal et al., 1996).

For a typical fMRI run, the frequency spectrum of the signal will show respiratory and cardiac peaks superimposed on a broad baseline of random noise, and a low frequency component of unknown origin. It has been suggested that these low frequency fluctuations may be caused by purely vascular events, like vasomotion (Nilsson and Aalkjaer, 2003) or cerebrovascular waves driven by neuronal pacemakers (Golanov et al., 1994). Lu and colleagues used an iron contrast agent to minimize potential confounds from cardiac pulsations, and observed low-frequency CBV fluctuations which they attributed to the same sources as Golanov and colleagues (Lu et al., 2006). Another possibility is that low-frequency fluctuations in CBF velocity may reflect the dynamic properties of cerebral autoregulation, because these are independent of the fluctuation in arterial blood pressure (Katura et al, 2006).

Nevertheless, a considerable fraction of the variance in the BOLD signal in the frequency range below 0.1 Hz appears to reflect fluctuation of neuronal activity (Raichle and Mintun, 2006). This was first suggested by Biswal and colleagues (Biswal et al., 1997), who demonstrated the presence of synchronous low frequency fluctuations of signal intensities from the resting human brain that have a high degree of temporal correlation both within and across the sensorimotor cortex. Similar results were obtained in the auditory and visual cortices. Furthermore, their results suggested that while variations in blood flow might contribute to functional connectivity maps,

BOLD signal played a dominant role in the mechanism that gives rise to functional connectivity in the human brain. These observations have led researchers to even posit the existence of a "default mode" of brain function (Raichle et al., 2001), defined in terms of the brain oxygen extraction fraction (OEF), which is remarkably uniform in the awake but resting state, despite considerable variation in resting state oxygen consumption and blood flow within gray matter and an almost four-fold difference between gray and white matter in both oxygen consumption and blood flow. Raichle and colleagues observed that all significant deviations from the mean hemisphere OEF were increases, signifying deactivations, and resided almost exclusively in the visual system. These decreases suggested the existence of an organized, baseline default mode of brain function that is suspended during specific goal-directed behaviors. Many studies on the functional connectivity of the resting brain followed. Greicius and colleagues (Greicius et al., 2003) further researched the positive or negative correlations between the posterior cingulate cortex and ventral anterior cingulate cortex, which consistently show greater activity during resting states than during cognitive tasks, and prefrontal regions that show increased activity during a given cognitive task. Fukunaga and colleagues (Fukunaga et al., 2006) have recently suggested that resting state activity represents a metabolic process and does not require a high level of alertness or consciousness. A report showing that the correlation level in the default mode network was significantly increased during sleep, has led researchers to posit a potential role of these fluctuations is homeostasis, possibly including synaptic plasticity (Horowitz et al., 2006).

Interestingly, Zarahn and colleagues (Zarahn et al., 1997) identified temporal autocorrelations in resting state data which were characterized by a frequency domain model that included a 1/f component, as is also observed in the power density of EEG or local field potentials (LFPs) in mammalian cortex (Freeman et al., 2000). This frequency dependency in EEG and LPFs might arise due to the limited speed neuronal communication, such that the period of oscillation of a given neuronal pool would be constrained by its size. In this way, higher frequency oscillations would be confined to a small neuronal space, whereas very large networks could be recruited during slow oscillations (Steriade, 2001; Csicsvari et al., 2003). In fact, synchronous neuronal fluctuations, occurring during rest, have been reported across a broad range of frequencies and spatial scales (Buzsaki and Draguhn, 2004), and may also contribute to the high variability observed in the time course of physiological signals, including those measured with functional imaging techniques. It has equally been suggested that lower-frequency fluctuations may correspond to power modulations of higher-frequency bands, with the first being coherent at larger spatial scales (Bruns et al., 2000; Leopold et al., 2003).

Despite their potential functional significance, the origin of the fMRI fluctuations is still under debate. For instance, subtle changes in a subject's breathing rate or depth, which occur naturally during rest at low frequencies (< 0.1 Hz), have been shown to be significantly correlated with the fMRI signal changes throughout gray matter and near large vessels, and in regions with high blood volume (Birn et al., 2006). In addition, these regions were found to coincide with many of the areas identified as part of the "default mode" network, which led the authors to suggest that the "default mode" is simply due to these subtle respiration changes.

This work examines the noise in fMRI experiments using BOLD and IRON contrasts; specifically, we measured BOLD and IRON signals in response to fixation-only, localized visual stimuli presented in a block design, and extended visual stimuli presented in an event-related fashion. We estimated the temporal correlations in a autoregressive model AR(p) for different experimental paradigms, and determined the power spectral distributions for BOLD and IRON contrasts without visual stimulation (fixation-only). We hypothesize that the main sources of correlated noise are signal dependent physiological noise (Kruger et al., 2001; Kruger and Glover, 2001; Triantafyllou et al., 2005), including image distortions arising from susceptibility changes due to motion correlated with stimulus presentation, and imprecise hemodynamic impulse response functions and/or inaccuracy of the GLM. Some types of noise correlation (e.g., motion) will scale with SNR (Kruger and Glover, 2001; Triantafyllou et al., 2005), whereas other types (e.g., model imperfections) can be expected to scale with CNR, particularly for event-related designs that are particularly sensitive to the form of the model and to linearity, from spending a relatively long time in transitions.

BOLD and IRON signals reflect different physiology: the BOLD signal is dependent on changes in the concentration of deoxyhemoglobin, and is very sensitive to the effects of CO_2; the IRON signal depends on blood volume changes. BOLD and IRON signals have different SNR and CNR, and these are weighed differently by blood volume fractions and large veins leading to different spatial distributions of signal. Furthermore, while both intra- and extravascular water contribute to BOLD signal at common field strengths, the IRON signal is exclusively extravascular.

On the other hand, we have reasons to think differences in noise between BOLD and IRON methods may be small. Many common noise sources, like respiration and motion, make similar contributions to both methods of contrast. Furthermore, the CNR of the two methods has been compared extensively, and it can be roughly predicted from signal changes and the assumption that the noise is the same. This sets a limit on expectations of potential differences in noise (e.g., by a factor << 2). In addition, BOLD and IRON methods are both accurately described by linear

model predictions (Friston et al., 1995; Boynton et al., 1996; Dale et al., 1997; Leite et al., 2002; Lu et al., 2005; Leite and Mandeville, 2006).

We expect signal dependent physiological noise to be the dominant factor explaining any observed differences. Image distortions due to bulk susceptibility changes arising from correlated motion are SNR dependent, and in this case, the noise spatial distribution would likely reflect different underlying physiology. Another possibility includes the relative importance of intravascular (IV) and extravascular (EV) contributions for BOLD and IRON.

A preliminary report of this work has been presented previously (Leite et al., 2006).

5.2 Methods

5.2.1 Animal Model

All experiments were performed at the Massachusetts General Hospital according to NIH and Institutional animal care guidelines, following general procedures as described previously (Leite et al., 2002; Leite and Mandeville, 2006). Two monkeys were trained to perform a high acuity fixation task while visual stimuli were presented in the background, and infrared eye tracking (DQW1_10 Version 1.10L, ISCAN, Inc. 1990-2004) was continuously performed. Horizontal and vertical pupil positions were recorded at 120 Hz, and water rewards discontinued if the pupil positions were consistently outside a pre-defined box (smaller than $1° \times 1°$) centered at the fixation point. On average, monkeys fixated accurately about 90% of the time.

For the IRON studies that employed the monocrystalline iron oxide nanoparticle (MION) contrast agent (Weissleder et al., 1990; Shen et al., 1993), the MION solution, containing 8 - 10 mg/kg of iron, was injected in the femoral vein below the knee just prior to each scanning session.

5.2.2 Visual Stimulation

The visual stimuli were projected from an LCD projector onto a screen which was positioned approximately 55 cm in front of the monkey's eyes. The stimulus covered a visual field of approximately $21° \times 24°$.

Monkeys performed a high acuity fixation task while localized (block design) or full field (even-related design) stimuli were presented in the background. The baseline condition was an isoluminant gray screen, and a fixation point ($0.2° \times 0.2°$) was presented in the center of the screen. The flickering frequency was 3 Hz (block-design) or 8 Hz (event-related design). Typical visual stimuli are shown in Fig. 5.1.

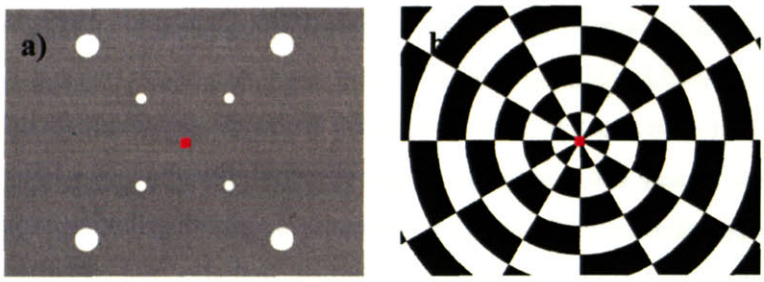

Fig. 5.1 a) Localized visual stimulus. The spots alternated between black and white at 3 Hz. The stimulus was on for 32 sec, off for 32 sec, in a block design fashion. In b) full field checkerboard stimulus was presented in an event-related design, with fixed or randomized interstimulus ISIs of 4 or 12 sec; the stimulus was on for periods of 4 sec, and the flickering frequency was 8 Hz. A fixation point was presented in the center of the screen at all times.

5.2.3 Magnetic Resonance Imaging

Experiments were performed in a 3 Tesla Siemens Allegra scanner (Siemens Medical System, Erlangen, Germany) using a custom surface coil for the radio frequency excitation and reception of signal. All functional imaging employed single-shot multi-slice GE-EPI with an isotropic resolution of 1.25 mm for block designs and 1.5 mm for ER designs. For block design experiments, 15 slices and 352 time points were acquired with TR/TE = 1000/24 msec. For ER experiments, 25 slices and 200 time points were acquired at TR/TE = 1500/24 msec. For the fixation-only experiments, 15 slices and 256 time points were acquired with TR/TE = 1000/24 msec. BOLD and IRON data were acquired in different sessions.

In addition to functional imaging, data with multiple echo times were acquired at the beginning and end of each IRON session to monitor the IRON dose by computing the baseline transverse relaxation rate for each session (Leite et al., 2002).

5.2.4 Data Analysis

Signals were described using a time-invariant general linear model (Friston et al., 1995; Boynton et al., 1996; Dale and Buckner, 1997) where the impulse response estimators of the hemodynamic response (HIRF), as determined in a previous work (Leite et al., 2002), were convolved with the stimulus time course to generate the regressors of interest. The eye-tracker traces in two perpendicular directions, convolved with HIRF, were included in the model as regressors of no-interest. A motion mismatch parameter derived from the motion correction procedure was added to the noise.

Monkeys' body motion outside the field of view (FOV) induces temporal and spatial changes in the magnetic field, causing apparent translations and deformations of the brain. Motion correction using the AFNI algorithm (Cox and Hyde, 1997), or by simply correcting for the phase roll in the y direction between each image and a template image, eliminates translations but not

deformations. The motion mismatch parameter is determined as the standard deviation between the template volume and each individual volume.

Ideally, the signal residuals will behave like white noise. Nevertheless, if the residuals have a different distribution, a thorough research on the noise characteristics might provide one more window into what is happening in the brain.

The simplest model of the temporal correlation structure is the first order autocorrelation model (Bullmore et al., 1996)

$$\varepsilon_i = \rho\varepsilon_{i-1} + \chi_{i1} \tag{5.2}$$

where $|\rho| < 1$ and χ_{i1} represents white noise. The resulting autocorrelation decays exponentially as the lag l increases:

$$\mathrm{cor}(\varepsilon_i, \varepsilon_{i-l}) = \rho^{|l|}. \tag{5.3}$$

This can be extended to autoregressive models of order p, denoted by AR(p), specified by

$$\varepsilon_i = \alpha_1\varepsilon_{i-1} + \alpha_2\varepsilon_{i-2} + \ldots + \alpha_p\varepsilon_{i-p} + \chi_n. \tag{5.4}$$

For these models the autocorrelation structure is more complex, including oscillatory terms and exponential decay (Worsley et al., 2002). The AR(p) parameters can be estimated by equating the sample autocovariances to their approximate expectations, and inserting the spatial-smoothed autocorrelations into the Yule-Walker equations, as described in detail by Worsley and colleagues.

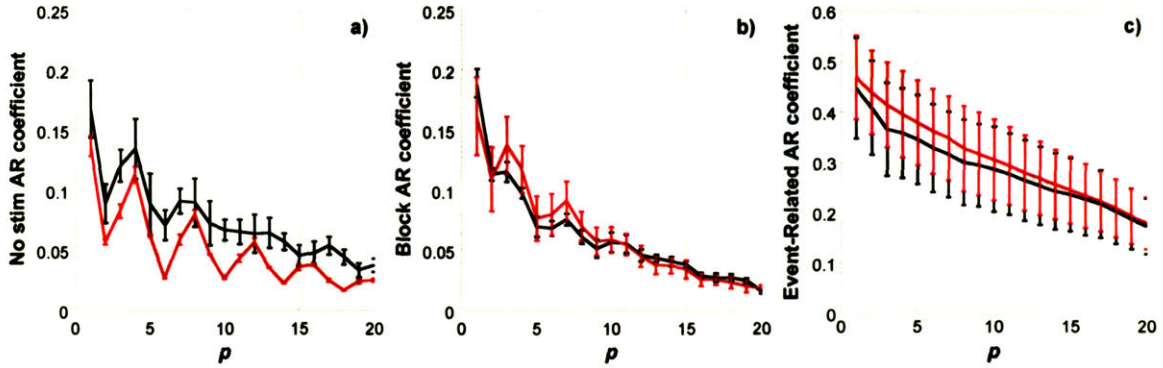

Fig. 5.2 Plots of the estimated autocorrelation coefficients as a function of model order for a) fixation-only, b) block designs and c) event-related designs. In a) the autocorrelation coefficients were averaged across the whole brain, while in b) and c) they were averaged only across the activated brain regions. IRON curves are plotted in red, and BOLD in black. The error bars are the standard deviation of the average estimates across sessions.

For each session, AR(p) parameters were averaged across all runs, and session maps of the estimated AR(p) coefficients were generated for BOLD and IRON contrasts, and then registered across sessions to achieve the required SNR. AR(p) coefficients were determined from 10 block design sessions, 5 BOLD and 5 IRON, in two monkeys; from 6 event-related sessions in 2

monkeys, 3 BOLD and 3 IRON; and from 4 sessions of stimulation-only in one monkey, 2 BOLD and 2 IRON. The spatial AR(1) maps were determined from the fixation-only sessions, therefore their sensitivity is limited by the reduced number of sessions.

Power spectral distributions (PSD) of the residuals for BOLD and IRON contrasts were computed with MatLab, using Welch's averaged, modified periodogram method. The PSD describes how the power of a signal or time series is distributed with frequency. The PSD was computed for each run, averaged across runs, and finally averaged across sessions. The power spectral distributions were determined from the fixation-only sessions, thus these results are limited due to the small number of acquired sessions.

5.3 Results

As observed in Fig. 5.2, the averaged autocorrelation parameters, up to order 20, are very similar for IRON and BOLD contrasts, across all design types. For event-related designs, the coefficients are slightly larger for IRON contrast than for BOLD contrast, and substantially larger than for block designs and fixation-only. For all types of paradigms the standard deviation of the sample autocorrelation in individual runs is roughly $1/\sqrt{n}$, were n is the number of time points in each run. The average sample coefficients were not statistically different within the activated regions with respect to the non-activated regions.

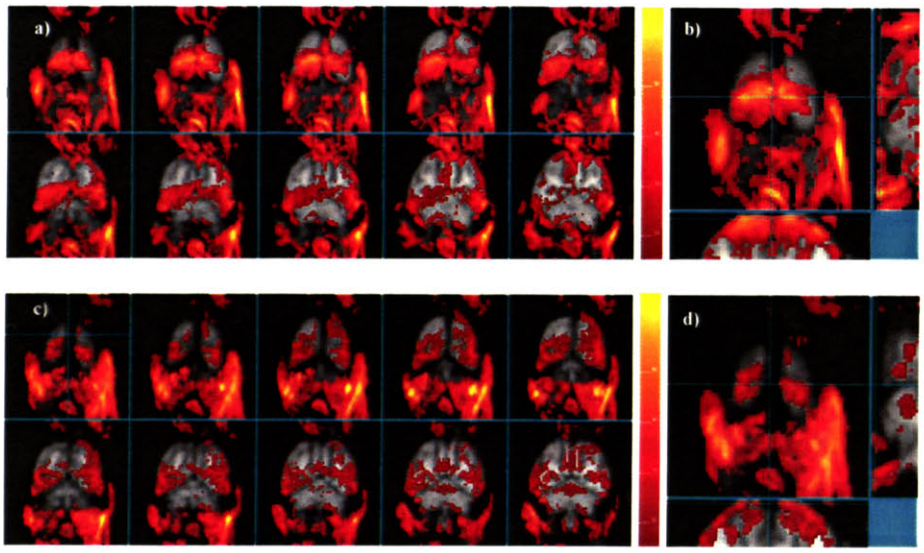

Fig. 5.3 Average maps of AR(1) coefficients for BOLD (a and b) and IRON (c and d). The AR values were multiplied by a factor of 100. The color scale is the same for both methods. For BOLD contrast, the AR coefficients are particularly elevated in areas of high blood volume. For both methods, the regions below the brain showing elevated coefficients correspond to the shoulders.

Averaged spatial distributions of first order AR coefficients for BOLD and IRON contrasts for fixation-only are shown in Fig. 5.3. The spatial distributions were averaged across sessions.

AR(1) coefficients are larger for BOLD contrast, particularly in areas of high blood volume, like sinuses (e.g., sagittal sinus and transverse sinus) and sulci (where the superior cerebral veins, that drain the superior, lateral and medical surfaces of the hemispheres, are mainly located). This was not observed with IRON contrast.

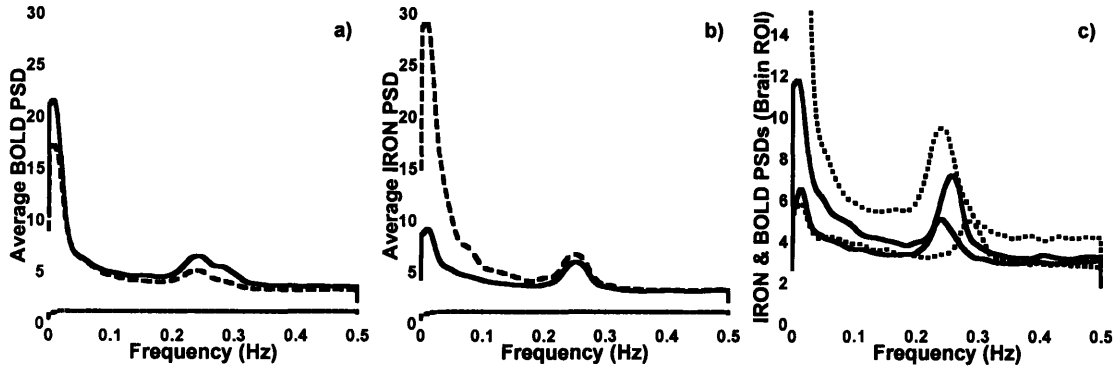

Fig. 5.4 Power spectral distributions of the residuals obtained from spatial smoothed images. In a) IRON contrast and b) BOLD contrast, the solid line shows the PSD averaged over the whole brain in the absence of a stimulus, the short dashed line corresponds to the body ROI, and the long dashed line corresponds to ROIs outside the brain and body. The data presented in a) and b) was averaged across sessions. In c) the brain PSD is shown for each individual session, 2 BOLD sessions (dashed lines) and 2 IRON sessions (solid lines). The sampling frequency was 1 Hz. All the data is normalized to the average noise outside the brain.

Plots of BOLD and IRON power spectral distributions at rest (with fixation-only) are shown in Fig. 5.4. The PSDs were determined from smoothed and non-smoothed images, but plotted only for smoothed sessions, as the main results are identical. The respiratory peak can be immediately identified for both methods of contrast, between 0.2 and 0.3 Hz. As the PSDs plotted are an average of two sessions, double respiratory peaks can be observed when the respiratory rate is different is each session. A low frequency peak can be observed for both methods of contrast and for brain and body ROIs. For a region of interest selected in the background that does not include any part of the monkey's body or ghost image, a constant distribution was observed across all frequencies, with similar amplitude for both methods of contrast.

5.4 Discussion

The noise contribution for BOLD and IRON contrasts appears to be very similar. The autocorrelated coefficients are essentially equal for both methods of contrast across all types of experiments analyzed and more than a factor of two smaller for block designs compared with ER designs. The power spectral distributions for BOLD and IRON, although still limited by the number of sessions, seem to overlap considerably. The main difference between the two methods of contrast appears to be in the spatial distribution of autocorrelated coefficients. For BOLD

contrast, the correlation coefficients are larger in areas of high blood volume, such as sulci, consistent with known BOLD underlying physiology. The same is not true for IRON contrast.

Inaccuracies in the impulse response function shape or in the linearity assumption are amplified in event-related designs due to the rapid rate of stimulus presentation. We believe this is the main noise source contributing to the factor of two difference in AR coefficients between ER designs and block designs. Furthermore, this type of noise grows with increasing sensitivity, hence AR parameters are slightly larger for IRON contrast (Leite and Mandeville, 2006).

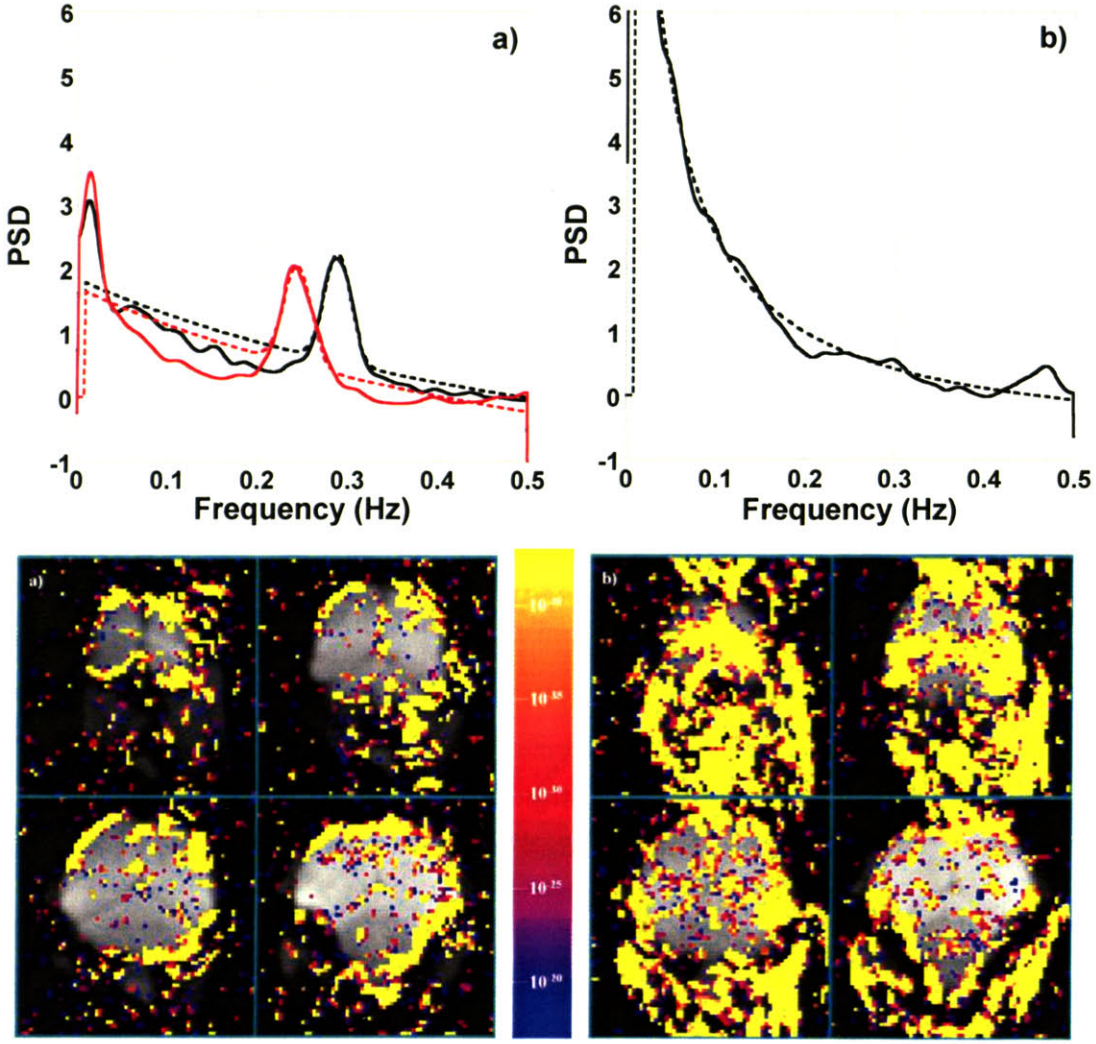

Fig. 5.5 Linear fits to observed point spectral distributions. All the data was normalized by the average background noise. a) Typical BOLD (black) and IRON (red) frequency spectra for a good session. The dashed curves represent the model fits. b) In this IRON session the monkey motion was severe. Spatial distribution maps for c) respiration fluctuations and d) 1/f fluctuations were obtained from the IRON session whose spectrum is shown in a).

The averaged PSDs are similar for both methods of contrast. The respiration peak occurs at approximately 0.3 Hz, and a low frequency peak occurs for frequencies smaller than 0.1 Hz. Low

frequency oscillations are not exclusive to the brain signal, and are also significant in the body signal. With BOLD contrast, brain and body PSDs are extremely similar, but not with IRON contrast. If this signifies that brain signal is less contaminated by body motion with IRON contrast than with BOLD contrast, or that for BOLD contrast there are other processes at low frequencies that sum to body contamination, or that the observed difference is merely an artifact of the low SNR, remains to be seen.

Given the multitude of possible noise sources, spatial information will helps us identify the most significant sources. A simple linear model to explain the noise frequency spectrum might include an offset, a respiration function modeled as a Gaussian function, and a general function inversely proportional to the frequency. In Fig. 5.5a, PSDs for BOLD and IRON contrast obtained from typically good sessions are fitted with the described model. The spatial distributions for the BOLD spectrum in Fig. 5.5a are shown in Figs. 5.5c and 5.5d. As described by Raj and colleagues (Raj et al., 2000, 2001), the effects of respiration are especially apparent in the edges of the image in the phase encoding direction. The effects of the noise source that varies inversely to the frequency appear to be particularly noticeable in regions of high blood volume and in the body of the monkey.

The PSD shown in Fig. 5.5b was derived from a group of runs acquired at the end of an IRON session. Typically, by the end of a session monkeys become restless. Maps may still show activation, but some of the images are severely distorted. In this case, the power spectrum could be fitted extremely well by a general 1/f function. It is fair to assume that the most significant noise source in this case were motion-induced susceptibility perturbations, which will then be characterized by a 1/f function.

5.5 References

Birn RM, Diamond JB, Smith MA, Bandettini PA, 2006. Separating respiratory-variation-related fluctuations from neuronal-activity-related fluctuations in fMRI. Neuroimage 31(4): 1536-48.

Biswal B, DeYoe AE, Hyde JS, 1996. Reduction of physiological fluctuations in fMRI using digital filters. Magn Reson Med 35(1): 107-13.

Biswal BB, Van Kylen J, Hyde JS, 1997. Simultaneous assessment of flow and BOLD signals in resting-state functional connectivity maps. NMR Biomed 10(4-5):165-70.

Boynton GM, Engel SA, Glover GH, Heeger DJ, 1996. Linear systems analysis of functional magnetic resonance imaging in human V1. J Neurosci 16: 4207-4221.

Bruns A, Eckhorn R, Jokeit H, Ebner A, 2000. Amplitude envelope correlation detects coupling among incoherent brain signals. Neuroreport 11(7): 1509-14.

Bullmore E, Brammer M, Williams SC, Rabe-Hesketh S, Janot N, David A, Mellers J, Howard R, Sham P, 1996. Statistical methods of estimation and inference for functional MR image analysis. Magn Reson Med 35(2): 261-77.

Buzsaki G, Draguhn A, 2004. Neuronal oscillations in cortical networks. Science 304(5679): 1926-9.

Cox RW, Hyde JS, 1997. Software tools for analysis and visualization of FMRI data. NMR in Biomedicine 10: 171-178.

Csicsvari J, Jamieson B, Wise KD, Buzsaki G, 2003. Mechanisms of gamma oscillations in the hippocampus of the behaving rat. Neuron 37(2): 311-22.

Dale AM, Buckner RL, 1997. Selective averaging of rapidly presented individual trials using fMRI. Hum Brain Mapp 5: 329-40.

Freeman WJ, Rogers LJ, Holmes MD, Silbergeld DL, 2000. Spatial spectral analysis of human electrocorticograms including the alpha and gamma bands. J Neurosci Methods 95(2): 111-21.

Friston KJ, Holmes AP, Worsley KJ, Poline JP, Frith CD, Frackowiak RSJ, 1995. Statistical Parametric Maps in Functional Imaging: A General Linear Approach. Hum Brain Mapp 2: 189-210.

Fukunaga M, Horovitz SG, de Zwart JA, van Gelderen P, Fulton SC, Balkin TJ, Duyn JH, 2006. Proc Intl Soc Mag Reson Med 14, pp 372.

Greicius MD, Krasnow B, Reiss AL, Menon V. , 2003. Functional connectivity in the resting brain: a network analysis of the default mode hypothesis. Proc Natl Acad Sci U S A. 100(1): 253-8.

Golanov EV, Yamamoto S, Reis DJ, 1994. Spontaneous waves of cerebral blood flow associated with a pattern of electrocortical activity. Am J Physiol 266(1 Pt 2): R204-14.

Horowitz SG, Fukunaga M, de Zwart JA, van Gelderen P, Fulton SC, Balkin TJ, Duyn JH, 2006. BOLD fMRI Resting State Activity and the Network of Default Mode Brain Function. Proc Intl Soc Mag Reson Med 14, pp 531.

Hu X, Le TH, Parrish T, Erhard P, 1995. Retrospective estimation and correction of physiological fluctuation in functional MRI. Magn Reson Med 34(2): 201-12.

Katura T, Tanaka N, Obata A, Sato H, Maki A, 2006. Quantitative evaluation of interrelations between spontaneous low-frequency oscillations in cerebral hemodynamics and systemic cardiovascular dynamics. Neuroimage 31(4): 1592-600.

Kruger G, Glover GH, 2001. Physiological noise in oxygenation-sensitive magnetic resonance imaging. Magn Reson Med 46(4): 631-7.

Kruger G, Kastrup A, Glover GH, 2001. Neuroimaging at 1.5 T and 3.0 T: comparison of oxygenation-sensitive magnetic resonance imaging. Magn Reson Med 45(4): 595-604.

Leite FP, Tsao D, Vanduffel W, Fize D, Sasaki Y, Wald LL, Dale AM, Kwong KK, Orban GA, Rosen BR, Tootell RB, Mandeville JB, 2002. Repeated fMRI using iron oxide contrast agent in awake, behaving macaques at 3 Tesla. Neuroimage 16(2): 283-94.

Leite FP, Mandeville JB, 2006. Characterization of event-related designs using BOLD and IRON fMRI. Neuroimage 29(3): 901-9.

Leite FP, Greve D, Vanduffel W, Mandeville JB, 2006. Temporal Autocorrelation of Noise for BOLD and IRON fMRI. Proc Int Soc Magn Reson Med, page 234.

Leopold DA, Murayama Y, Logothetis NK, 2003. Very slow activity fluctuations in monkey visual cortex: implications for functional brain imaging. Cereb Cortex 13(4): 422-33.

Lu H, Soltysik DA, Ward BD, Hyde JS, 2005. Temporal evolution of the CBV-fMRI signal to rat whisker stimulation of variable duration and intensity: a linearity analysis. Neuroimage 26(2): 432-40.

Lu H, Gitajn L, Rea W, Stein EA, Yang Y, 2006. Resting-state Functional Connectivity in Rat Brain. . Proc Natl Acad Sci U S A. 100(1): 253-8.

Nilsson H, Aalkjaer C, 2003. Vasomotion: mechanisms and physiological importance. Mol Interv 3(2):79-89, 51.

Raichle ME, MacLeod AM, Snyder AZ, Powers WJ, Gusnard DA, Shulman GL, 2001. A default mode of brain function. Proc Natl Acad Sci U S A 98(2): 676-82.

Raichle ME, Mintun MA, 2006. Brain work and brain imaging. Annu Rev Neurosci 29: 449-76.

Raj D, Paley DP, Anderson AW, Kennan RP, Gore JC, 2000. A model for susceptibility artefacts from respiration in functional echo-planar magnetic resonance imaging. Phys Med Biol 45(12): 3809-20.

Raj D, Anderson AW, Gore JC, 2001. Respiratory effects in human functional magnetic resonance imaging due to bulk susceptibility changes. Phys Med Biol 46(12): 3331-40.

Shen T, Weissleder R, Papisov M, Bogdanov A Jr, Brady TJ 1993. Monocrystalline Iron Oxide Nanocompounds (MION): Physiochemical Properties. Magn Reson Med 29: 599-604.

Steriade M, 2001. Impact of network activities on neuronal properties in corticothalamic systems. J Neurophysiol 86(1): 1-39. Review.

Triantafyllou C, Hoge RD, Krueger G, Wiggins CJ, Potthast A, Wiggins GC, Wald LL, 2005. Comparison of physiological noise at 1.5 T, 3 T and 7 T and optimization of fMRI acquisition parameters. Neuroimage 26(1): 243-50.

Triantafyllou C, Hoge RD, Wald LL, 2006. Effect of spatial smoothing on physiological noise in high-resolution fMRI. Neuroimage [Epub ahead of print]

Weissleder R, Elizondo G, Wittenberg K, 1990. Ultrasmall superparamagnetic iron oxide. Characterization of a new class of contrast agents for MR imaging. Radiology 175: 489-49.

Worsley KJ, Liao CH, Aston J, Petre V, Duncan GH, Morales F, Evans AC, 2002. A general statistical analysis for fMRI data. Neuroimage 15(1): 1-15.

Zarahn E, Aguirre GK, D'Esposito M, 1997. Empirical analyses of BOLD fMRI statistics. I. Spatially unsmoothed data collected under null-hypothesis conditions. Neuroimage 5(3): 179-97.

Chapter 6

Multi-Shot EPI with Navigators in the Awake Monkey at 3 Tesla

6.0 Preface

On a bad day, a movie of single shot echo planar images of a monkey brain may make one ask if the monkey is loose inside the scanner. In fact, although his head is securely attached to the experimental apparatus, his body is free to move, and the magnetic field perturbations originated by his occasionally vigorous motion may severely distort the images. These distortions are particularly noticeable in the phase encoding direction, due to its reduced bandwidth compared to the readout direction.

In this chapter we present a first attempt to correct this problem. We developed a multi-shot EPI acquisition with the assumption that this method would diminish distortions but increase artifacts, which we tried to correct by acquiring "navigators" (additional data used to determine and correct off-resonance effects that can corrupt the images). Navigators provide useful information when the artifacts are small, but ultimately this strategy is bound to fail when field perturbations become so large as to also corrupt the navigators. Here, we describe our implementation, our experience with imaging monkeys with this sequence, and regimes where this strategy might be useful.

6.1 Introduction

The challenges of obtaining high spatial resolution functional images in awake and behaving macaque monkeys are somewhat different from imaging strategies in humans. In spite of rigid fixation of the monkey's head to the experimental apparatus, in single-shot echo-planar images (SS-EPI) the brain appears to be moving mostly in the phase encoding direction, sometimes as much as ¼ of the field of view (FOV) in the most posterior coronal slices. The apparent brain motion and additional image deformations are mainly due to temporal and spatial magnetic field perturbations caused primarily by the motion of the monkey's body outside the FOV. This mechanism has been qualitatively described for human fMRI (Yetkin et al., 1996) and is similar to the magnetic susceptibility effects of respiration on echo planar images acquired in human subjects as described by Raj and colleagues (Raj et al., 2000, 2001). These image distortions

cause spatial and temporal blurring of activation on a pixel basis, with a subsequent drop in functional sensitivity, and the appearance of artifactual activations (Hu and Kim, 1994).

The phase evolution of a pixel in a magnetic resonance image is dictated by the local magnetic field it experiences. The longer the acquisition time, the larger the accumulated phase, and the larger the phase difference of spins between different locations in an inhomogeneous magnetic field. These phase differences translate into a faster T_2^* decay and long acquisition times will give rise to severe susceptibility effects.

Different strategies have been employed to reduce acquisition time in fast imaging sequences like EPI or spiral. For instance, partial k-space single-shot EPI acquisitions (Jesmanowicz et al., 1998) not only greatly decrease the readout time, but also have a point spread function (PSF) which is approximately $\sqrt{3}$ narrower than the PSF of full k-space acquisitions. Other methods designed to acquire only a part of the desired k-t space as a way to decrease acquisition time, include keyhole imaging (Jones et al., 1993; van Vaals et al., 1993), reduced-encoding MR imaging with generalized-series reconstruction (RIGR) (Webb et al., 1993), data sharing (Riederer et al., 1988), zero filling (Du et al., 1994), reduced FOV methods (Hu and Parrish, 1994; Madore et al., 1999), and non Fourier approaches (Zientara et al., 1994).

Methods trying to specifically correct for the susceptibility effects of respiration have been implemented in humans. Navigator echoes are specially encoded echoes that can be interleaved into the imaging sequence to accurately track the position and phase of an object of interest within the FOV (Ehman and Felmlee, 1989), and have been used to monitor and compensate for physiological image fluctuations in fMRI derived from cardiac pulsation or respiration (Hu and Kim, 1994). Pfeuffer and colleagues developed a simple correction that used phase information from the center of k-space and a navigator echo to decrease the noise from respiration induced phase and frequency fluctuations (Pfeuffer et al., 2002). Roopchansingh and colleagues developed a technique in which the central part of k-space is collected twice to obtain magnetic field maps simultaneously with image data (Roopchansingh et al., 2003). In addition to correcting geometric distortions that resulted from magnetic field perturbations, this method was used to measure field shifts arising from respiration and jaw motion.

As distortions occur mainly in the phase encoding direction, which has a much smaller bandwidth than the readout direction, a straightforward strategy is to reduce the acquisition time per shot using multi-shot EPI (McKinnon, 1993). Advantages of this imaging approach include greater flexibility between the tradeoffs of imaging time, T_2^* relaxation, gradient power, resolution, image distortion, and signal-to-noise ratio (SNR). Although deformations of image slices are indeed greatly reduced, magnetic field perturbations generally differ during acquisition

of different segments, causing the segments to add incoherently. Therefore, multi-shot EPI (MS-EPI) provides an alternative method to SS-EPI with reduced distortion but increased artifacts. The suitability of MS methods depends upon the scale of the field perturbations.

In the work we implemented a multi-shot EPI strategy with navigators, and we found that we could obtain reasonably good image stability at short echo times, but motion artifacts were too large to be corrected at echo times generally employed for BOLD fMRI. This method may prove useful at short TE.

6.2 Theory

Neglecting relaxation, the 2D echo planar signal is given by

$$S(t) = \int_x \int_y \rho(x,y) e^{-i\Phi(x,y,t)} dxdy, \tag{6.1}$$

with

$$\Phi(x,y,t) = \gamma \int_0^t B(x,y,\tau) d\tau . \tag{6.2}$$

In a homogeneous magnetic field, the phase acquired by a spin at position (x,y) and time t will be given by $\Phi(x,y,t) = 2\pi(k_x(t)x + k_y(t)y)$.

In the presence of magnetic field perturbations, $B(x,y,t) \rightarrow B(x,y,t) + \Delta B(x,y,t)$. The linear form of the field perturbation is given by

$$\Delta B(x,y,t) = \Delta B_0(t) + \Delta G_x(t)x + \Delta G_y(t)y + O(x^2, xy, y^2), \tag{6.3}$$

where $\Delta G_i = \partial(\Delta B(t))/\partial i$. Substituting into the signal equation we get

$$S(t) = \int_x \int_y \rho(x,y) e^{-i2\pi\left[k_x(t)\left(x + \frac{\gamma \Delta G_x(t) t}{2\pi k_x(t)} x\right) + k_y(t)\left(y + \frac{\gamma \Delta B_0(t) t}{2\pi k_y(t)} + \frac{\gamma \Delta G_y(t) t}{2\pi k_y(t)} y\right)\right]} dxdy . \tag{6.4}$$

At each point in k-space, the time variable may be given by $t = TE + nt_y \pm m\delta t$, where TE is the echo time, δt is the dwell time, t_y the time interval between adjacent k_y lines, m the m^{th} line and n the n^{th} line. Let $-N_x/2 \le m \le N_x/2$ and $-N_y/2 \le n \le N_y/2$, where N_x is the number of columns in k-space, and N_y the number of rows. Substituting this time variable into the signal equation, pixels in a distorted 2D echo planar image will be shifted as

$$\rho(x,y) \rightarrow \rho\left(x + \frac{\Delta G_x}{G_x} x, y + \frac{\Delta B_0 t_y}{G_y \tau} + \frac{\Delta G_y t_y}{G_y \tau} y\right), \tag{6.5}$$

where $\overline{G_y \tau}$ is the area of a gradient blip in the phase encoding direction. Because the time required for phase encoding is much longer than the time required for readout, the effects of the static field inhomogeneities will be stronger in the phase encoding direction. Examples of distortions typically observed in single shot echo planar images are shown in Fig. 6.1. The image distortions are usually worse in the most posterior and inferior regions of the brain (nearer the body).

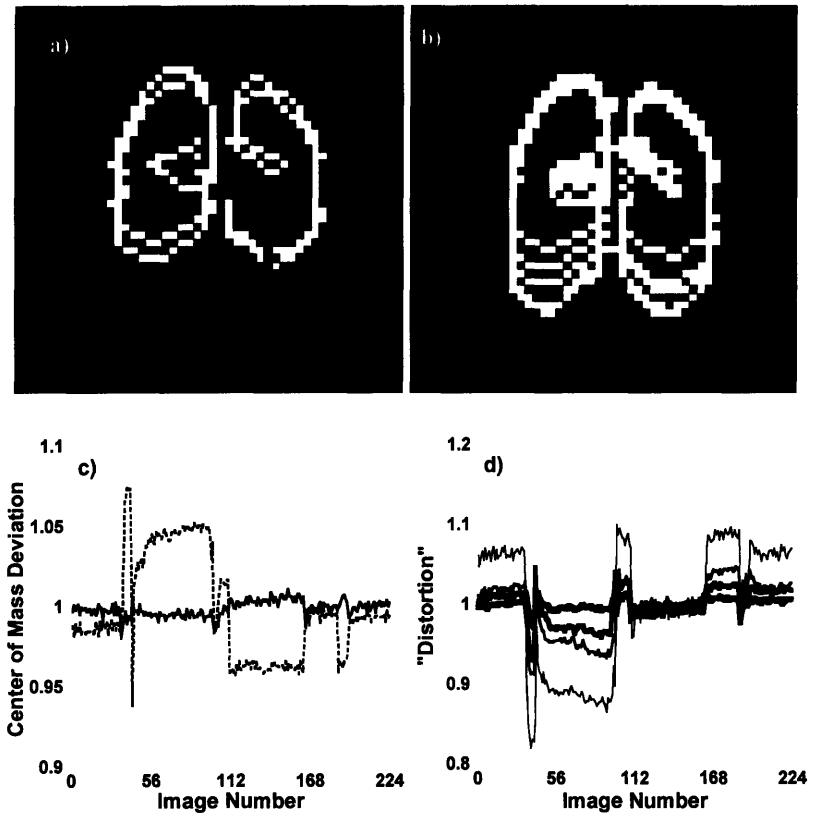

Fig. 6.1 Edge plot for a typical single-shot EPI coronal slice at a time point where mainly a) zeroth order distortions (translations) were observed, or b) first order distortions (deformations) were observed. In c) the timecourse of the slice center of mass in the x (solid line) and y (dashed line) directions is shown. As it becomes obvious from these figures, the main distortions, either translations or deformations, occur in the y, or phase encoding, direction. In d) an index of distortion (the SNR drop in a fixed ROI corresponding to the undistorted image) is plotted for four different slices, from most anterior slices suffering fewer distortions (thicker line), to most posterior slices, most severely distorted (thinner line).

As the area of the phase encoding gradient increases, the distortions in the y direction will become smaller. Therefore, multi-shot EPI is a straightforward strategy to decrease the effects of field perturbations in the images.

As can be observed in Fig. 6.2a for a typical image acquired with multi-shot EPI without the application of any corrections, the shape of the slice is stable in time, but the image intensity is smeared along the phase-encode direction. This is what one can expect from field perturbations

that remain stable on the time scale of the acquisition of each segment, but vary from segment to segment. Even for a spatially independent change in magnet field, an overall phase shift and roll are acquired by the spins of a given slice, and these vary from segment to segment. The aliased image obtained from each segment will now be shifted differently relative to an image that experienced no phase shift, such that the aliased parts will not cancel when adding the segments, and ghosting will occur.

To account for sources of artifacts in multi-shot EPI, at least three different corrections are needed:

1. $\Delta B_0(t)$: a spatially independent change in field produces a time-varying phase shift in k-space (equivalently, a positional shift in image space). We determined the phase difference across two central navigator lines embedded in each segment at $k_y = 0$, and we then corrected this phase roll across each segment. To correct for a ΔB_0 offset at the echo time (TE), we determine the total phase across the first x navigator in each segment, and remove it from each line in the segment. This correction is performed in k-space, and it is very likely the most important correction.

2. $\Delta G_x(t)$: an off-resonance x gradient will produce a shift of the peak signal in k_x, which is equivalent to a phase roll in x image space. Based upon the measured phase roll in image space for the central navigator lines, each k_y line for each segment can be corrected with a phase roll dependent upon the timing with respect TE.

3. $\Delta G_y(t)$: the strategy used to correct for an x gradient cannot be applied in the phase-encode direction, due to the sparse sampling for each segment in that direction. Thus, to correct the G_y induced shifts, the actual k_y positions need to be recorded, as determined by a y navigator line at $k_x = 0$ that was additionally added to each segment. The data can then be resampled in y onto uniform steps followed by an FFT; alternatively, data can be reconstructed without use of the FFT by using the calculated values of k_y for each line. To account for variation in sampling density in the final k-space data, temporal smoothing may prove useful.

6.3 Methods

6.3.1 Magnetic Resonance Imaging

Experiments were performed in a 3 Tesla Siemens Allegra scanner (Siemens Medical System, Erlangen, Germany) using a custom surface coil for the radio frequency excitation and reception of signal.

Multi-shot echo planar images were acquired in a 3T Siemens Allegra magnet, with variable amounts of segmentation: results reported here used 16 segments. The matrix size was 64×64 or 96×96, and the in-plane image resolution was 1.25 mm or 0.8 mm, respectively. The slice

thickness was 1.25 mm. The TR per segment was 250 msec, with a time per volume of 4 sec for 16 segments. The RF pulse was set to the Ernst angle. The number of slices acquired was set to the maximum number allowed by the time per volume. The echo time was usually set to the minimum TE allowed, for BOLD and IRON contrasts, except for the last set of BOLD experiments, where the TE was optimized to provide the best possible contrast-to-noise ratio (CNR).

In order to correct for the effects of field perturbations, the multi-shot EPI sequence was modified to acquire one y navigator line immediately after the readout for each segment, and two extra x-encoded navigator lines were added at the positions of the two central lines in k-space for all segments.

Typical image reconstruction was modified only slightly to include the distortions' corrections. Implementation details of the corrections are described in the appendix.

6.3.2 Animal Model

All experiments were performed at the Massachusetts General Hospital according to NIH and Institutional animal care guidelines, and following the general procedures as described previously (Leite et al., 2002, 2006). Two monkeys were trained to perform a high acuity fixation task while visual stimuli were presented in the background. Infrared eye tracking (DQW1_10 Version 1.10L, ISCAN, Inc. 1990-2004) was performed at all times, and water rewards discontinued if the pupil x and y positions were consistently outside a pre-defined box centered at the fixation point.

In IRON studies, a monocrystalline iron oxide nanoparticle (MION) contrast agent (Weissleder et al., 1990; Shen et al., 1993) solution (8 - 10 mg/kg of MION) was injected in the femoral vein below the knee just prior to each scanning session.

6.3.3 Visual Stimulation

The visual stimuli were projected from an LCD projector onto a screen which was positioned approximately 55 cm in front of the monkey's eyes. The stimulus covered a visual field of approximately $21° \times 24°$, and the fixation point ($0.2° \times 0.2°$) was shown in the center of the screen at all times. Stimuli were presented in a block design.

6.3.4 Data Analysis

We assumed a linear time-invariant model for the observed fMRI response (Friston et al., 1995; Boynton et al., 1996; Dale and Buckner, 1997, Leite et al., 2002; Lu et al., 2005; Leite et al., 2006), and followed the procedure described in previous work (Leite et al., 2002, 2006).

6.4 Results

The use of multi-shot EPI decreased the appearance of image distortions. Nevertheless, ghosting due to overall phase shifts between segments did occur, as can be observed in Fig. 6.2a. The outline of the slice is considerably more stable than with SS-EPI, but there are areas of signal loss inside the brain and increased signal in the background, due to incorrect cancellation of the aliased images from each segment.

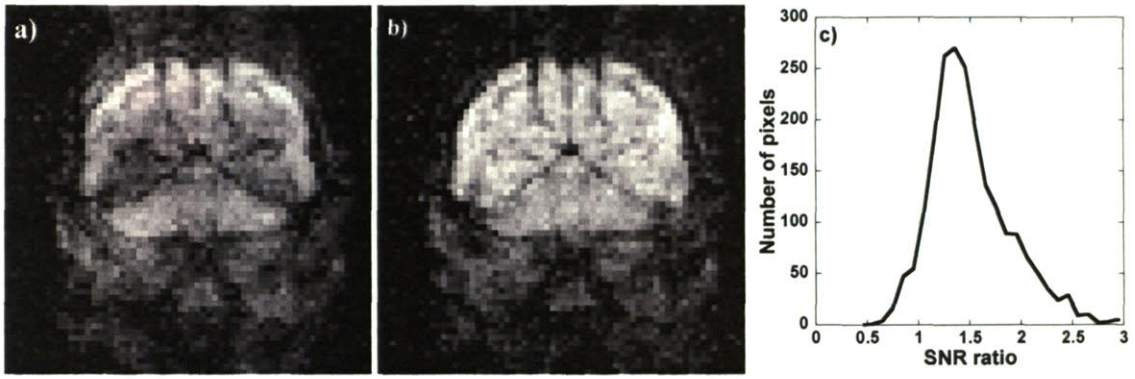

Fig. 6.2 Typical EPI image of a brain coronal slice acquired with 16 shots a) before and b) after applying navigator corrections. c) Histogram of SNR gain of corrected vs uncorrected data.

Fig. 6.2b shows a typical example of an IRON contrast coronal slice after correcting for ΔB_0 and ΔG_x. The ΔG_y correction scheme is still not implemented at this point. Applying these two navigator corrections considerably improved the image. As can be observed in Fig. 6.2c, for 16 shots the temporal SNR gain due to navigator corrections was typically 50%.

Contrast	Matrix Size	TE	Single-Shot EPI			Multi-Shot EPI		
			tSNR	aSNR	tSNR/aSNR	tSNR	aSNR	tSNR/aSNR
BOLD	*64x64*	*short*				14.91	24.67	0.60
		long	21.80	32.97	0.66			
	96x96	*short*				12.02	23.76	0.51
		long				7.03	15.34	0.46
IRON	*64x64*	*short*				13.10	20.83	0.63
		long	9.96	15.67	0.64			
	96x96	*short*				10.68	17.23	0.62
		long						

Table 6.1 Temporal to anatomical SNR ratio for single-shot EPI and multi-shot EPI for BOLD and IRON contrast fMRI. The echo time was the same for BOLD and IRON contrasts, and it was set to the minimum TE allowed by the sequences, considering some desired parameters.

In Table 6.1 we compare SS-EPI with MS-EPI for BOLD and IRON contrasts. As expected for BOLD, the anatomical SNR (aSNR) and temporal SNR (tSNR) decrease for MS-EPI, particularly for larger matrix size and increased TE. For this long TE, the SNR of the navigators drops significantly, and the phase acquired from motion in orthogonal directions increases, thus

the derived phase information fails to improve the images. For IRON contrast, even a non optimized dose of MION led to a slight increase in tSNR and aSNR of MS-EPI with respect to SS-EPI for the short TE used. The ratio tSNR/aSNR was approximately constant for IRON with SS or MS (with short or long TEs).

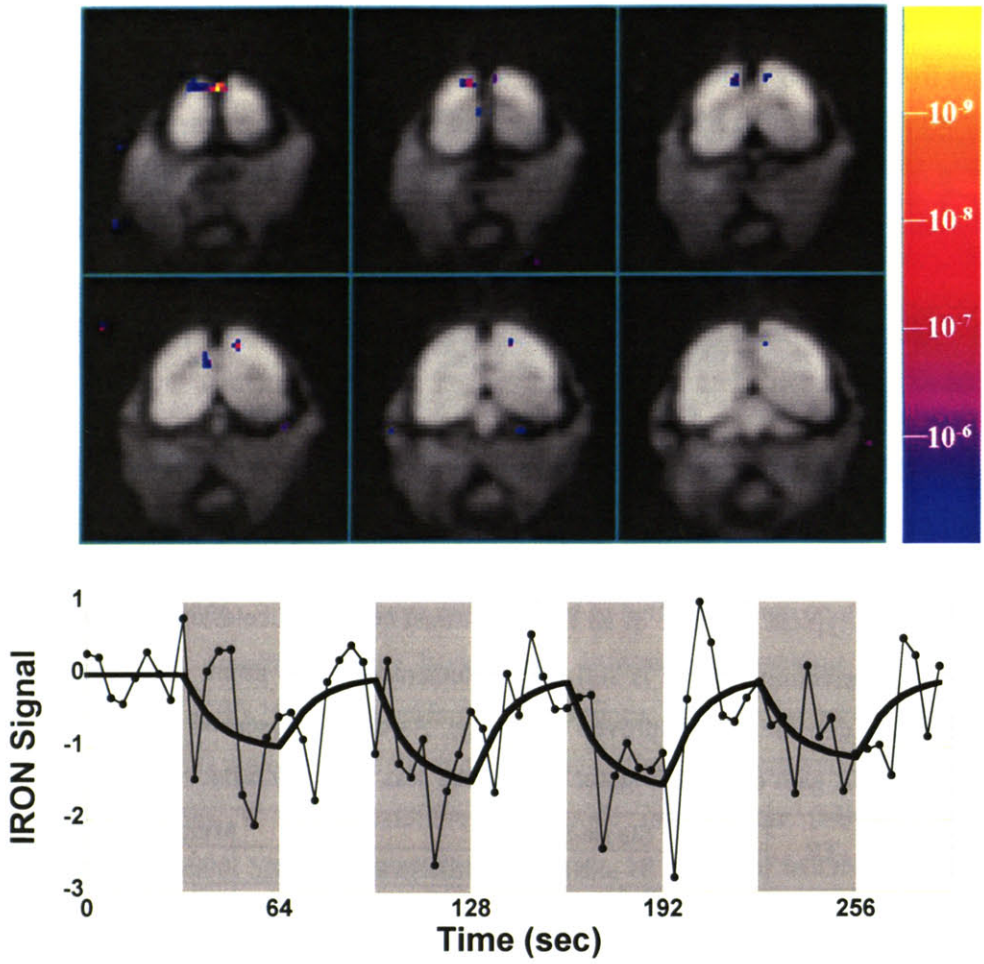

Fig. 6.3 IRON activation map and time course obtained with multi-shot EPI in response to a spots' stimulus. The IRON dose was not optimized for maximum contrast at the short TE used. Nevertheless, some activated spots can be detected, but the tSNR is very low. Due to the very short TE and relatively insufficient IRON dose, some blood signal is still apparent in the region of the sagittal sinus in the first slice.

In Fig. 6.3, a typical activation map and time course within an activated region of interest are shown for IRON contrast using MS-EPI. The IRON dose was not optimized for maximum contrast at the short TE used. Nevertheless, some spots can be seen, and the signal, although extremely noisy, shows a positive correlation with the stimulus time course.

6.5 Discussion

The implemented corrections increased the quality of the images collected using MS-EPI with short TE. Increasing the echo time to maximize BOLD contrast, the severe drop in the

navigators' SNR prevents the derived corrections to be successfully implemented. We expect multi-shot EPI to be especially useful for IRON fMRI, which can employ very short TEs to minimize phase variations, and still achieve maximum CNR even for very short TEs by increasing the MION dose (Mandeville et al., 2004).

Navigator corrections are most useful when perturbations are small. Large perturbations affect not only the images, but also the navigator lines, corrupting the correction strategy. Off-resonance perturbations in k-space directions that are orthogonal to the navigator are particularly destructive in this regard.

Perturbations can be minimized by reducing the echo time, especially since the correction for the ΔB_0 effect seems to be the most important correction. ΔG_x and ΔG_y corrections do not scale down with TE.

Using short TE is not compatible with high CNR for BOLD fMRI, so this is not a promising strategy. However, this strategy can be made compatible with IRON fMRI, provided very high doses of agent are employed (e.g., dose-TE product must be same as with long TE SS-EPI). In fact, CNR can be optimized independent of TE for IRON method but not for BOLD, where the amount of contrast agent is fixed. This strategy (short TE with high dose) has been shown for rodent imaging (Mandeville et al., 2004) and may be useful here, but the higher accumulated iron doses will be a drawback in this model.

A more successful strategy has been implemented in our lab at 7 Tesla by Hauke Kolster (*personal communication*), who built phased-array coils and is using SENSE acquisitions combined with UNFOLD to reduce image distortions. This is the strategy we are going to implement at 3 Tesla in the near future.

6.6 Appendix

As was shown in the Theory section of this paper, to first order, magnetic field perturbations in 2D echo planar images, can be expressed as a time varying field given by equation 6.3.
While the general outline to implement the corrections derived from the acquired navigator lines was already introduced in the Theory section, the detailed correction will be described here.

6.6.1 Correction for the phase offset in k_y in (x-k_y) hybrid space

The first step is to compute the absolute phase across the first x navigator line for each segment. Each line in that segment will then be multiplied by the inverse of the computed phase. The phase can also be determined using the second navigator, but consistence should be present across segments. If the first x navigator line is given by $X_1(t)$, and image lines are given by $L_n(t)$, this correction will look like:

$$L_n^{corrected}(t) = L_n(t)e^{-i\left[\text{phase}\left(\sum_t X_1(t)\right)\right]}, \tag{6.6}$$

where n is the line index, $n = 0,...,N_y/N_{seg} - 1$, N_y is the total number of k_y lines to be acquired, and N_{seg} is the number of segments. It is important to remember that both the magnitude and phase of the acquired images are kept.

6.6.2 Correction for the phase roll in k_y in (x-k_y) hybrid space

In this case, the phase slope is determined as the cross correlation between the two x navigator lines acquired for each segment. This phase slope is then multiplied by the index of the k_y line to be corrected, taking the time reference to be the time when the first navigator line is acquired. Therefore, each corrected line will be given by

$$L^{corrected}(t) = L(t)e^{-i\left[\text{phase}\left(X_1(t)X_2(t)^*\right)\right]\left(n-\frac{1}{2}\frac{N_y}{N_{seg}}\right)}, \tag{6.6}$$

where n is the line index, N_y is the total number of k_y lines to be acquired, and N_{seg} is the number of segments.

6.6.3 Correction for the phase roll in x in(x-ky) hybrid space

The phase acquired due to first order field perturbations in the readout direction is determined by calculating the phase of the autocorrelation of one of the x navigator lines. Assuming that the phase roll in image space is due to the x gradient, causing a shift in k-space, the shift (or phase roll) varies with time. Therefore, for each line to be corrected, the phase calculated above is multiplied by the fraction of time that goes from the excitation to that line. The normalization constant is the echo time. Next, each readout line is multiplied by the inverse of the calculated phase roll.

$$L_m^{corrected}(t) = L_m(t)e^{-i\left[phase\left(X_1(t)X_1(t)^*\right)\right]\left(m-\frac{N_x}{2}\right)}, \tag{6.8}$$

where m is the column index, varying between $m = -N_x/2,...,N_x/2-1$, and N_x is the total number of points acquired per line.

6.6.4 Correction for the phase roll in y in image domain

Not implemented at this point.

6.7 References

Boynton GM, Engel SA, Glover GH, Heeger DJ, 1996. Linear systems analysis of functional magnetic resonance imaging in human V1. J Neurosci 16: 4207-4221.

Dale AM, Buckner RL, 1997. Selective averaging of rapidly presented individual trials using fMRI. Hum Brain Mapp 5: 329-40.

Du YP, Parker DL, Davis WL, Cao G, 1994. Reduction of partial-volume artifacts with zero-filled interpolation in three-dimensional MR angiography. J Magn Reson Imaging 4(5): 733-41.

Ehman RL, Felmlee JP, 1989. Adaptive technique for high-definition MR imaging of moving structures. Radiology 173(1): 255-63.

Friston KJ, Holmes AP, Worsley KJ, Poline JP, Frith CD, Frackowiak RSJ, 1995. Statistical Parametric Maps in Functional Imaging: A General Linear Approach. Hum Brain Mapp 2: 189-210.

Hu X, Kim SG, 1994. Reduction of signal fluctuation in functional MRI using navigator echoes. Magn Reson Med 31(5): 495-503.

Hu X, Parrish T, 1994. Reduction of field of view for dynamic imaging. Magn Reson Med 31(6): 691-4.

Jesmanowicz A, Bandettini PA, Hyde JS, 1998. Single-shot half k-space high-resolution gradient-recalled EPI for fMRI at 3 Tesla. Magn Reson Med 40(5): 754-62.

Jones RA, Haraldseth O, Muller TB, Rinck PA, Oksendal AN, 1993. K-space substitution: a novel dynamic imaging technique. Magn Reson Med 29(6): 830-4.

Leite FP, Tsao D, Vanduffel W, Fize D, Sasaki Y, Wald LL, Dale AM, Kwong KK, Orban GA, Rosen BR, Tootell RB, Mandeville JB, 2002. Repeated fMRI using iron oxide contrast agent in awake, behaving macaques at 3 Tesla. Neuroimage 16(2): 283-94.

Leite FP, Mandeville JB, 2006. Characterization of event-related designs using BOLD and IRON fMRI. Neuroimage 29(3): 901-9.

Lu H, Soltysik DA, Ward BD, Hyde JS, 2005. Temporal evolution of the CBV-fMRI signal to rat whisker stimulation of variable duration and intensity: a linearity analysis. Neuroimage 26(2): 432-40.

Madore B, Glover GH, Pelc NJ, 1999. Unaliasing by fourier-encoding the overlaps using the temporal dimension (UNFOLD), applied to cardiac imaging and fMRI. Magn Reson Med 42(5): 813-28.

McKinnon GC, 1993. Ultrafast interleaved gradient-echo-planar imaging on a standard scanner. Magn Reson Med 30(5): 609-16.

Pfeuffer J, Van de Moortele PF, Ugurbil K, Hu X, Glover GH, 2002. Correction of physiologically induced global off-resonance effects in dynamic echo-planar and spiral functional imaging. Magn Reson Med 47(2): 344-53.

Raj D, Paley DP, Anderson AW, Kennan RP, Gore JC, 2000. A model for susceptibility artefacts from respiration in functional echo-planar magnetic resonance imaging. Phys Med Biol 45(12): 3809-20.

Raj D, Anderson AW, Gore JC, 2001. Respiratory effects in human functional magnetic resonance imaging due to bulk susceptibility changes. Phys Med Biol 46(12): 3331-40.

Riederer SJ, Tasciyan T, Farzaneh F, Lee JN, Wright RC, Herfkens RJ, 1988. MR fluoroscopy: technical feasibility. Magn Reson Med 8(1): 1-15.

Roopchansingh V, Cox RW, Jesmanowicz A, Ward BD, Hyde JS, 2003. Single-shot magnetic field mapping embedded in echo-planar time-course imaging. Magn Reson Med 50(4): 839-43.

Shen T, Weissleder R, Papisov M, Bogdanov A Jr, Brady TJ 1993. Monocrystalline Iron Oxide Nanocompounds (MION): Physiochemical Properties. Magn Reson Med 29: 599-604.

van Vaals JJ, Brummer ME, Dixon WT, Tuithof HH, Engels H, Nelson RC, Gerety BM, Chezmar JL, den Boer JA, 1993. "Keyhole" method for accelerating imaging of contrast agent uptake. J Magn Reson Imaging 3(4): 671-5.

Webb AG, Liang ZP, Magin RL, Lauterbur PC, 1993. Applications of reduced-encoding MR imaging with generalized-series reconstruction (RIGR). J Magn Reson Imaging 3(6): 925-8.

Weissleder R, Elizondo G, Wittenberg K, 1990. Ultrasmall superparamagnetic iron oxide. Characterization of a new class of contrast agents for MR imaging. Radiology 175: 489-49.

Yetkin FZ, Haughton VM, Cox RW, Hyde J, Birn RM, Wong EC, Prost R, 1996. Effect of motion outside the field of view on functional MR. AJNR Am J Neuroradiol 17(6): 1005-9.

Zientara GP, Panych LP, Jolesz FA, 1994. Dynamically adaptive MRI with encoding by singular value decomposition. Magn Reson Med 32(2): 268-74.

Chapter 7
Concluding Remarks

The awake, behaving macaque is an important model for neuroscience and biomedical studies, because it forms a bridge between rodent and human studies, eliminates complications of anesthesia, and enables critical correlative measurements that can clarify the biological basis of non-invasive neuroimaging. Despite these well-known advantages of the model, only two laboratories in the world now routinely employ fMRI in awake monkey, and both laboratories primarily rely upon the IRON method. Based upon the quantitative results presented here, IRON contrast is the method of choice in awake, behaving macaque monkeys fMRI at 3 Tesla, due primarily to the increased detection power provided by this method.

7.1 Detection Power

Sensitivity to CBV can be obtained from images that are weighted either by the longitudinal (T_1) or transverse (T_2) relaxation times. However, general principles suggest that the sensitivity of T_2-weighted imaging should be significantly greater than for T_1 methods, since the volume fraction of hydrogen spins contributing to changes in T_1 is limited to intravascular spins and a very small fraction of extravascular spins affected by spin-spin coupling via direct interaction, a mechanism limited by the exchange rate of water. By contrast, magnetic field perturbations from intravascular agents extend throughout the extravascular space (Villringer et al., 1988) and in that way dominate T_2 and T_2^* relaxation. Hence, T_2/T_2^* methods boost sensitivity relative to T_1 methods by influencing a relatively greater number of spins set by the extra- to intravascular volume fraction, which is of order 20.

Weissleder and colleagues (Weissleder et al., 1990) introduced and described MION, a stable colloid that enabled target specific MR imaging. The MION contrast agent remains intravascular for hours and has a large magnetic susceptibility, inducing magnetic field gradients that significantly extend into the extravascular space. If the dose of contrast agent is sufficiently large, changes in T_2 or T_2^* during activation mainly reflect changes in CBV, and the BOLD contribution can be neglected.

The first use of boluses of contrast agent (gadolinium-DTPA) for determining CBV at well-spaced time points (tens of minutes) was reported in the first human functional MRI experiment by investigators in our laboratory (Belliveau et al., 1991). The first use of an intravascular

paramagnetic contrast agent with a long blood half-life for dynamically measuring CBV as a function of time was reported by Hamberg et al. (1996) to measure relative blood volume changes during hyperemia after occlusion.

Two years later, Mandeville and colleagues (Mandeville et al., 1998) used MION in an anesthetized rat model to perform MR measurements of dynamically changing blood volume during hypercarbia and sensory stimulations using T_2-weighted rapid imaging at 2 Tesla and 4.7 Tesla. They quantified the increase in R_2^* due to the injection of contrast agent, and the consequent loss in SNR. In addition, they roughly predicted both the magnitude and field dependence of the enhancement in CNR. They verified that the use of MION significantly increased functional CNR relative to BOLD contrast, and that the magnetic field dependence of signal changes using CBV contrast differs from the field dependency observed for BOLD contrast. Whereas BOLD changes in R_2^* increase in an approximately linear manner with magnetic field, CBV-weighted changes should be independent of the field for a given signal drop due to the injection of contrast agent. In particular, when TE and contrast agent dose are chosen to optimize CNR, the changes in signal simply reflect changes in CBV. Two other studies using iron oxide contrast agents were published the same year (Kennan et al., 1998; van Bruggen et al., 1998), also showing an increase in CNR due to the injection of the iron oxide contrast agent.

Our 2002 study extended Mandeville's results in anesthetized rats to awake macaques and to a much wider range of stimulation paradigms (Leite et al., 2002). We showed that the use of IRON contrast increased functional sensitivity by a factor of three relatively to BOLD contrast in block designs at 3 Tesla using the shortest echo times consistent with single-shot EPI. However, this factor decreased to only 1.5 for rapidly presented paradigms with a fixed inter-stimulus duration, a consequence of the slow temporal response of CBV. In order to mitigate this loss of sensitivity for rapid stimulus presentations, we showed how IRON functional sensitivity could be optimized in event-related designs by using random or semi-random distributions of interstimulus intervals (Leite and Mandeville, 2006).

The field-dependence of the relative sensitivities of IRON and BOLD fMRI for block paradigms was recently described (Mandeville et al., 2004), with an emphasis on experiments where in recent years it has been found that the gain in sensitivity of the IRON method compared to BOLD method is significant even at much higher field strengths, as long as multi-shot sequences are used with very short TEs, and the MION dose is optimized to achieve the maximum amplification factor at each echo time.

Nevertheless, the advantages of IRON contrast using single-shot echo planar imaging at high field, is a somewhat open question, because minimum echo times are limited by the need to

acquire the entire image in a single excitation. Alternative imaging strategies, like accelerated acquisitions enabled by phased-array coil technology, or centric encoding schemes like spiral imaging, should remove limitations on echo time, and thereby enable improvements in CNR as found in anesthetized rodents using multi-shot methods. However, improved sensitivity at short echo times comes at the price of higher doses of contrast agent, and this must be considered for often repeated longitudinal studies in our awake primate model.

7.2 Temporal Response

7.2.1 Measurements

In order to understand the physiology of functional activation, and to know how to optimize experimental designs, we need a detailed understanding of the signal kinetics. The temporal evolution of CBV was examined by Mandeville in anesthetized rats (Mandeville et al., 1998), who found that the peak response of CBV was very delayed relative to the peak response of BOLD signal. Furthermore, the duration of the CBV delay was temporally consistent with the BOLD post-stimulus undershoot. A profound temporal mismatch was further observed between relative CBV and relative CBF (Mandeville et al., 1999): while the increase in relative CBF (rCBF) after stimulus onset and decrease after stimulus cessation were accurately described with a single exponential time constant of approximately 2.4 sec, relative CBV changes (rCBV) exhibited two distinct and nearly sequential processes after both onset and cessation of stimulation. A rapid change of rCBV occurring immediately after onset and cessation was not statistically different from the time constant for rCBF. In addition, a slow phase of increase at onset, or decrease at cessation, with an exponential time constant of approximately 14 sec began approximately 8 sec after the rapid phase. Furthermore, an initial dip was not observed in BOLD signal, which showed a delay with respect to rCBF that was roughly consistent with the cerebral blood transit time in rat somatosensory cortex (Marota et al., 1999).

Similarly to previous studies in rats, we found in awake macaques that the impulse response functions for BOLD and IRON signals were both multi-modal. In fact, the initial IRON response was as fast as the BOLD response, but this was only a small contribution to the total change in CBV for a long stimulus; the dominant contribution evolved with a much slower time constant. The dominant positive BOLD response could be fit using only a rapid time constant, but a description of the BOLD post-stimulus undershoot needed an additional longer time constant. Therefore, using a basis of mono-exponential basis functions, we found that the IRFs for BOLD and IRON contrasts could be accurately described by the same two time constants: a fast time constant of approximately 4.5 sec, and a slow time constant of approximately 13.5 sec. To

describe the response at high temporal resolution, we either included a time delay of 1.5 sec, or added a 1.5 sec time constant to the exponential basis. Using these methods, we could fit BOLD and IRON time courses irrespective of the stimulus paradigm.

In addition to our studies, one group subsequently has described the temporal response of IRON contrast, and measured an IRF which is very similar to the one we measured (Lu et al., 2005).

Recently, Lu and colleagues (2003) have introduced a new fMRI technique that is sensitive to blood volume changes during neuronal activity. This technique, called vascular-space-occupancy (VASO)-dependent fMRI, uses a nonselective inversion pulse in combination with an optimal inversion time (TI) to eliminate blood signals. The remaining tissue signal is determined by the amount of extravascular water protons in a voxel, and is therefore related in some way to CBV. They have shown that the BOLD undershoot appears to last much longer than the prolonged blood volume increase, as indicated by the VASO technique. They have concluded that the BOLD post-stimulus undershoot cannot be explained solely by a delayed CBV return, and suggested that this negative BOLD effect must be due to an increase in OEF. However, quantitative results for the percent change in CBV appear to be about 3 times too high using this method (Lu and van Zijl, 2005), so it is still not clear exactly what the technique is measuring.

Using diffuse optical tomography (DOT), Siegel et al. (2003) showed total hemoglobin (HbT) data tracked IRON signal extremely well. In fact, both HbT, a measurement of red blood cell volume, and IRON signal relaxation, a measurement of blood plasma volume, should exhibit a proportionality to changes in the blood volume fraction, provided that the hematocrit within the region of activation remains constant during the measurement. In addition, they showed that both dHb and HbO_2 time courses tracked BOLD time courses within the stimulus region, but their behavior in the post-stimulus undershoot differed. The time course of dHb showed a more profound undershoot than either HbO_2 or BOLD, although the shape of the curve closely matched the BOLD signal. On the other hand, HbO_2 tracked the BOLD signal better in magnitude than did dHb, but the contours of the two time courses appeared to differ. BOLD signal includes contributions from both intravascular and extravascular water. While the former effect is most pronounced at low fields, the latter is expected to be roughly linear with dHb. For this reason, high-field BOLD signal should more closely reflect dHb in the post-stimulus undershoot if the source is elevated CBV.

7.2.2 Physiology

This thesis addressed some fundamental physiological questions concerning the hemodynamic response during changes in local cerebral activity. Is CBV simply a redundant measurement of CBF, which is governed by arteriole vasocontrol, or do the kinetics of IRON signal suggest otherwise? Do changes in CBV affect the amount of deoxygenated blood in a voxel, and therefore also affect BOLD signal, or do these changes primarily represent oxygenated blood?

Buxton et al. (1998) proposed a balloon model to describe the temporal dynamics of changes in CBV and BOLD signal. This model applies conservation of mass to relate changes in volume (V) in a compliant compartment to the difference between the flown into (F_{IN}) and out of (F_{OUT}) this compartment, F_{IN}-F_{OUT} = dV/dt. Although their formulation demonstrates that a temporal mismatch between flow and volume can occur in principle, as also allowed by the earlier models described in Chapter 1, the physiology of the flow-volume relationship is unspecified by the balloon model. On the other hand, Mandeville and Marota (1999) employed a modified windkessel model in an attempt to describe the temporal evolution of CBV changes within a physiological framework. Because about 80% of CBV is contained in capillaries and veins, and only 3% to 5% of total CBV resides within the arterioles, the principal resistance vessels, they modeled capillary and venous compliance using a post-arteriole windkessel to describe a passive post-arterial response to pressure modulated by arteriole dilation and contraction, and neglected blood volume in the arterial compartment, which they assumed to be small. They described the time course of CBV changes as a rapid elastic response of capillaries and veins followed by slow venous relaxation of stress. They further suggested that venous delayed compliance could be the mechanism behind the post-stimulus undershoot in BOLD.

On the other hand, others have claimed that CBV is dominated by the arterial side of the vasculature (Lee et al., 2001), based upon a separation of arteries and veins into two compartments in terms of diffusion characteristics, with the motivation that arterial velocities are higher than venous velocities. However, the validity of their methods is questionable, as they neglected to account for the fact that blood velocity increases during activation, and assigned small diffusion weightings to arteries, although these same diffusional weightings have been shown to significantly attenuate BOLD signal (Boxerman et al., 1995).

Measuring the compartmental fractions of basal CBV, let alone the contributions of each compartment to functional changes in CBV, is difficult and indirect by any method. Our derived IRFs for BOLD and IRON contrasts allowed for a simple physiological interpretation, which turned out to be consistent with the premises and results of the windkessel model. In fact, taking

into account the relative magnitudes of the two main exponential basis functions used to fit BOLD and IRON IRFs, we identified the two time constants for BOLD signal as the responses of blood oxygenation (fast) and blood volume (slow). For the IRON method, the time constants are presumably related to arterial (fast) and capillary-venous (slow) dilations. In fact, the 2-exponential decomposition of the BOLD signal suggested that changes in CBV reduce the BOLD effect by 40% during prolonged stimulation. On the other hand, the IRON decomposition showed that the slow time constant contained 80% of the strength during prolonged stimulation. Since capillaries and veins comprise about 80% of basal CBV, our results suggest that relative changes in total CBV match those in capillary/venous CBV, and therefore the large changes that are known to occur in arterioles (a small compartment) do not beat the smaller changes that occur in capillaries and veins (a much larger compartment).

Nevertheless, some authors have suggested using a scaling factor in front of CBV in the equation that gives BOLD signal changes in terms of changes in CBF, CBV and $CMRO_2$, which will significantly down-rate its effect, therefore elevating the estimated contribution of $CMRO_2$ with the premise that CBV changes are primarily arteriolar (Kim et al., 1999).

A recent study described a new method for non-invasive measurements of venous CBV in humans (Stefanovic and Pike, 2005). They found that estimated changes in venous CBV are as large as one would expect using the relationship between changes in CBF and total CBV (Grubb et al., 1974). By inference, this implies that changes in total CBV approximately reflect changes in venous CBV, in general agreement with our results. However, their method lacks the sensitivity to provide useful information about the dynamic response of CBV.

7.3 Spatial Resolution

As described in the Introduction and in Chapter 4, previously to our work, fMRI spatial resolution had been examined mainly by assessing the possibility of measuring submillimeter structures, like ocular dominance columns in humans or orientation columns in anesthetized cat. While the ability to measure columnar activation by fMRI is an exciting goal, and many claimed to achieve the necessary functional resolution to measure these structures, only Cheng et al. (2001) established the reproducibility of their measurements. Furthermore, it is not clear whether such measurements can be generalized to regions outside columnar domains, which may have specific vascular topology.

An approach that directly attempted to measure the BOLD PSF, was introduced by Engel and colleagues who used common retinotopic stimuli (expanding checkerboard rings and rotating checkerboard wedges) to evaluate the spatial precision of BOLD fMRI at 1.5 T (Engel et al.,

1997). They found that the BOLD spatial resolution was consistent with a linespread whose FWHM was 3.5 mm.

We have directly measured BOLD and IRON point spread functions by measuring the cortical response to point-image stimulus and their inverse (holes) in a checkerboard pattern, and estimated the maximum spatial fMRI PSF in monkey V1 to be no larger than 1.5 mm for IRON contrast, and not statistically different for BOLD contrast (Leite et al., 2004, 2005). Accounting for additional blurring mechanisms, like image resolution and T_2^* decay, we estimate "true" PSFs to be approximately 0.8 mm for BOLD contrast and 0.4 mm for IRON contrast.

During the course of our work, many other groups have reported results using fMRI or optical intrinsic signals to address related issues. Preliminary experiments performed at 9.4 T in anesthetized cats found point spread functions for BOLD and CBF in the range of 1.6 mm and 0.5 mm, respectively (Olman et al., 2004; Park et al., 2004; Park et al., 2005). Using IRON contrast at 9.4 Tesla in anesthetized cats, Zhao and colleagues measured average distances between iso-orientation domains of approximately 1.4 mm and 1.7 mm in two orthogonal directions (Zhao et al., 2005).

On the other hand, optical results are variable and dependent upon analysis procedures (e.g., differential pathlength correction and other issues that can lead to error in the separation of cromophores into HbO_2 and dHb). In fact, while some groups have claimed that total Hb images provide smaller activation areas than oxy- or deoxyhemoglobin signals (Siegel et al., 2003; Culver et al., 2005), others have found that the spatial extent of the change in deoxyhemoglobin is smaller than that of oxyhemoglobin, total hemoglobin, CBF and $CMRO_2$ (Thompson et al., 2003; Dunn et al., 2005; Thompson et al., 2005).

Even though there are still some unresolved issues, we expect IRON contrast to achieve better spatial resolution if only because of its better functional sensitivity. While the intrinsic linewidth for IRON is slightly larger than for BOLD, the contribution of the relaxation linewidth will be insignificant if the imaging bandwidth is much larger that the T_2^* broadening. As can be seen in Fig. 7.1 for IRON and BOLD contrasts at 3 Tesla, this is generally the case. This figure is based upon the use of single-shot EPI with the gradient limitations of our current "Allegra" system. Also, the figure assumes that IRON fMRI always uses the shortest possible echo time, and that the dose of contrast agent at each time is adjusted to optimize functional sensitivity. For BOLD signal, the figure assumes that the echo time is set to the tissue T_2^*, or to the minimum echo time allowed by the gradients if this is longer than T_2^*. In comparison with single-shot EPI (Fig. 7.1a), multi-shot EPI or accelerated acquisitions using multiple coils will further reduce the spatial blurring due to T_2^* decay, as can be seen in Fig. 7.1b for an acceleration factor of 2.

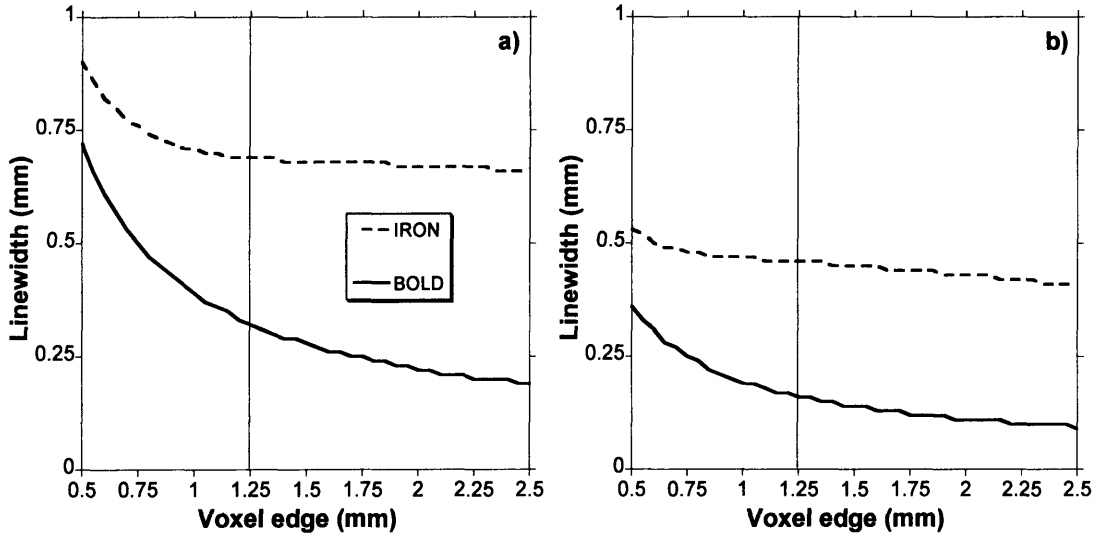

Fig. 7.1 Linewidth for BOLD (solid line) and IRON (dashed line) contrasts as a function of voxel size for a) SS-EPI acquisition and b) MS-EPI or SENSE EPI acquisition with acceleration factor of 2. The linewidth is proportional to the acquisition time and the relaxation rate R_2^* of the method of contrast employed.

Another problem that awaits solution is the correction or avoidance of motion-induced distortions. As mentioned in Chapter 4, we think that the main effects of the observed image distortions are a decrease in functional sensitivity, as real activations are wiped out by artifactual signals, and a decrease in SNR, because runs containing severely affected images are completely discarded. There is also a blurring effect of the distortions, but we have reasons to believe that this is small (distortions affect images particularly in the phase encoding direction, still the dimensions of the cortical point image are not statistically different in the phase encoding direction compared to the readout direction). On the other hand, the presence of these distortions seriously prevents attempts to increase spatial resolution using single-shot EPI, as a further increase in acquisition time, and consequently an increase in echo time, is unavoidable, as observed in Fig. 7.2a

Therefore, as we strive to increase image spatial resolution with single-shot EPI, image distortions become so severe that other solutions must be pursued. Because distortions increase proportionally to the time spent collecting the data in the phase encoding direction, a straightforward strategy is to use methods that acquire the full k-space in many rapid partial acquisitions. Therefore, multi-shot EPI or SENSE acquisitions are obvious solutions. By acquiring partial k-space with each of a given number of coils, SENSE uses the coil sensitivity profile to achieve the desired phase encoding, and therefore the required spatial resolution and FOV. Using SENSE, acquisitions for each slice are simultaneous, and static shot-to-shot phase differences between partial acquisitions will not occur. As can be observed in Fig. 7.2b, the use of

SENSE acquisition with an acceleration factor of 2 increases the BW per pixel and allows for shorter echo times, therefore improving the stability of the images with respect to motion-induced distortions even at high resolution. In fact, with SENSE-EPI and 2-fold acceleration one can go down to a voxel edge of 0.8 mm before distortions are of similar amplitude to what we observe at 1.25 mm voxel edge with SS-EPI. In addition, as observed in Fig. 7.1, phase encoding blurring will not be an issue at a voxel edge of 0.8 mm for both BOLD and IRON contrasts. Two-fold acceleration will also provide a slight increase in SNR with respect to single-shot EPI, but still significantly reduced when compared to the SNR at a voxel edge of 1.25 mm.

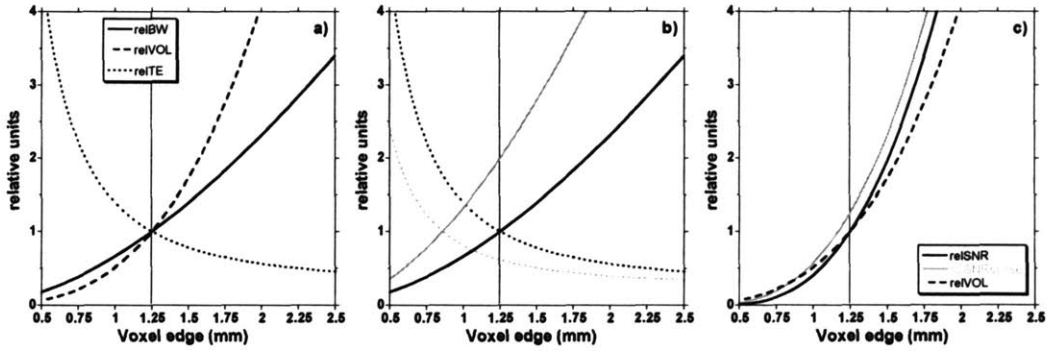

Fig. 7.2 a) Relative BW per pixel (solid line), relative voxel volume (long dashed line), and relative TE (short dashed line) versus voxel edge for single-shot EPI with our MRI system. b) Relative BW per pixel (solid line) and relative TE (dashed line) for SS-EPI (black lines) and SENSE-EPI with 2-fold acceleration (gray lines lines). c) Relative SNR for SS-EPI (black solid line) and SENSE-EPI with 2-fold acceleration (gray solid line). Also plotted is the relative voxel volume (long dashed line). All curves are relative to the observed value at a voxel edge of 1.25 mm for SS-EPI. All the image parameters used with SENSE-EPI with 2-fold acceleration were identical to SS-EPI.

Of course, SENSE acquisitions entail their own challenges. Fitting the required number of coils around the small monkey brain in order to achieve homogenous full-brain coverage is a technological problem. Other artifacts, particular to SENSE reconstruction, do exist, but results already obtained in our lab at 7 Tesla (Hauke Kolster, *personal communication*), seem to indicate this is the most effective road to follow in order to achieve higher spatial resolution.

At this point we are limited mainly by image resolution. Assuming we can surpass this limitation and obtain an estimate of the vascular PSF on the order of what is expected in V1 from psychophysics and invasive techniques, rigorous determination of the neuronal spread using electrophysiology should be performed, and the neuronal PSF deconvolved from our measured PSF in order to obtain a true measure of vascular spread.

7.4 Spatial Localization

Mandeville and Marota (1999) observed that the distribution of BOLD CNR shows a significant dorsal shift with respect to IRON method, for somatosensory stimulation in

anesthetized rats. This shift decreases with increasing field strength, and it was attributed to the gradient of resting state blood volume across the somatosensory cortex and the different CNR characteristics of the two image methods. They concluded that the IRON method has a more uniform sensitivity to percent changes in functional indicators (CBV or dHb) across regions of variable resting state CBV. Others have also found that IRON fMRI localizes activation to the middle cortical layers, whereas BOLD foci are shifted toward the outer layers (Kennerley et al., 2005).

However, IRON and BOLD contrasts may no longer show a tight spatial coupling at very high resolution, where MRI tissue elements can no longer be assumed to be typical "well-mixed" compartments showing very similar admixtures of arterials, capillaries, and veins. Assuming a conventional resistive model of brain vasculature (e.g., windkessel model), arteriole vasodilation reduces the pressure drop across that compartment, so additional pressure shifts to other compartments and causes dilation in capillaries and veins. As the relative dilation in each compartment depends upon the relative change in flow and the compliance characteristics of the vessels, increased pressure across capillaries and veins facilitates a larger component of the flow change in those compartments than in arterioles. In this way, the degree of dilation in each compartment can vary considerably, with small arterioles dilating much more than other vessels.

We found that IRON contrast has better apparent spatial specificity than BOLD contrast in our studies in macaques (Leite et al., 2002). With IRON contrast, activation was not detected in and around large draining veins, contrary to BOLD contrast. In addition, we found tissue regions showing BOLD signal with no IRON signal. The location of these tissue regions between large activation volumes that were identified by both methods, together with a lack of activation found by the IRON method, suggest that these regions are showing changes in oxygenation due to drainage from the activated regions to the large venous structures. Nevertheless, no more research was pursued in this direction during this thesis, as an accurate exploration of this issue requires MION injections in the magnet for within session comparisons, which we cannot do at this point.

Zhao and colleagues have examined the cortical layer dependence of BOLD and CBV responses. They found that GE and SE BOLD changes were spread across the cortical layers. On the other hand, GE and SE CBV-weighted fMRI responses peaked at the middle cortical layer, which has the highest experimentally determined microvasculature volume. The FWHM was < 1 mm (Zhao et al., 2006). Nevertheless, this measurement of the FWHM may be limited by the cortical thickness in that region of the cortex (in humans, cortical thickness varies from $1 - 4.5$ mm). In this case, this would be a good example of resolution set by the size of the structure,

regardless of hemodynamic regulation, and a true measurement of the vascular PSF could not be derived.

7.5 Linearity

Previously to our work, the relationship between stimulus duration and the BOLD response had been extensively studied (Boynton et al., 1996; Dale and Buckner, 1997; Friston et al., 1998; Vasquez and Noll, 1998; Glover, 1999; Birn et al., 2001). Generally, responses to long duration stimuli can be predicted approximately as time-shifted summations of the responses to shorter stimuli of about 4 sec or longer in duration, whereas very brief stimuli produce larger responses than predicted from a linear model. The nonlinearity in BOLD signal can arise from nonlinearities between the stimulus and the neural response, the neural response and the hemodynamics, or both.

Studies simultaneously measuring electrical activity and hemodynamic responses to stimuli, had shown that different metrics of the neural response vary with the hemodynamic response in an approximately linear manner over a restricted dynamic range (Ngai et al., 1999; Logothetis et al., 2001).

In addition, CBF, as measured by arterial spin labeling, had been found to be more linear in the temporal domain than BOLD signal in certain brain regions, consistent with the notion that a major source of BOLD nonlinearity is the finite headroom for changes in deoxyhemoglobin concentration (Mechelli et al., 2001; Miller et al., 2001)

Although no IRON fMRI studies had explicitly investigated neural response linearity at the time we started the work presented in this thesis, the general linear model proved to accurately describe data in a wide variety of stimulus paradigms (Leite et al., 2002; Leite and Mandeville, 2006), as described in Chapters 2 and 3.

Our assumption was further confirmed by Lu et al. (2005) who explicitly examined IRON contrast linearity. Both superposition and scaling tests showed that IRON responses are generally consistent with a linear time-invariant model. In particular, they showed that the response to a stimulus of higher intensity can be scaled from that of lower intensity. However, significant deviations exist when the stimulus duration is manipulated, particularly in the trailing edge of the IRON response curves.

Recently, additional studies simultaneously measuring electrical activity and hemodynamic responses to stimuli, have shown that different metrics of the neural response may also vary with the hemodynamic response as a power law over a wide dynamic range (Devor et al., 2003; Sheth et al., 2004) or as an inverse sigmoidal (Jones et al., 2004).

Nevertheless, the work presented in this thesis again reinforces the utility of the linear model to predict hemodynamic responses to neural activation, for both BOLD and IRON contrast mechanisms.

7.6 Summary of unique contributions

While building on a respectful volume of previous findings in the anesthetized rat model and in humans, unique contributions have been achieved in the awake non-human primate in the work presented in this thesis.

We have found that, similarly to BOLD response, the IRON response is very linear across a wide range of stimulus paradigms. Work performed by Lu et al. (2005) has also directly confirmed our finding. This property of IRON and BOLD contrasts was the basis for all the analysis performed in this thesis.

We provided the first quantitative demonstration of a large increase in detection efficiency in awake monkey models by using an exogenous iron oxide contrast agent.

By measuring the hemodynamic response functions of BOLD and IRON contrasts across different stimulus designs, we were the first to demonstrate the dependence of the sensitivity ratio on stimulation paradigms for IRON contrast. Furthermore, from linear fits to the data across the different paradigms, and using the dominant observed time constants, we were able to show that IRON and BOLD signals were accurately described by two temporal components, and we could also determine the strength of each component in each method of contrast.

We further showed that IRON contrast beats BOLD contrast for event-related designs at clinical field strengths, and optimized the IRON to BOLD efficiency ratio by using different distributions of event-types. We introduced a discrete measure of entropy, the Shannon entropy, as an upper bound in predictability, and showed that small increases in predictability could be traded for large increases in detection efficiency, particularly for the IRON contrast.

Our work constitutes, to date, the best demonstration of increased functional specificity of IRON contrast relative to BOLD contrast. We observed that BOLD activation maps show apparent draining artifacts in "tissue" regions, which are not shown in IRON activation maps.

We were the first to implement a parametric measurement of the point spread function for BOLD and IRON constrasts. Our implementation is not set by anatomy or vascular topology, in contrast with imaging functional units or cortical layers. We accounted for different sources of blurring to achieve the smallest measures of IRON and BOLD PSF to date: we determined an IRON PSF not larger than approximately 0.4 mm, and a BOLD PSF two times larger.

7.7 References

Belliveau JW, Kennedy DN Jr, McKinstry RC, Buchbinder BR, Weisskoff RM, Cohen MS, Vevea JM, Brady TJ, Rosen BR, 1991. Functional mapping of the human visual cortex by magnetic resonance imaging. Science 254(5032): 716-9.

Birn RM, Saad ZS, Bandettini PA, 2001. Spatial heterogeneity of the nonlinear dynamics in the FMRI BOLD response. Neuroimage 14(4): 817-26.

Boxerman JL, Bandettini PA, Kwong KK, Baker JR, Davis TL, Rosen BR, Weisskoff RM, 1995. The intravascular contribution to fMRI signal change: Monte Carlo modeling and diffusion-weighted studies in vivo. Magn Reson Med 34(1): 4-10.

Boynton GM, Engel SA, Glover GH, Heeger DJ, 1996. Linear systems analysis of functional magnetic resonance imaging in human V1. J Neurosci 16: 4207-4221.

Buxton RB, Wong EC, Frank LR, 1998. Dynamics of blood flow and oxygenation changes during brain activation: the balloon model. Magn Reson Med 39(6): 855-64.

Culver JP, Siegel AM, Franceschini MA, Mandeville JB, Boas DA, 2005. Evidence that cerebral blood volume can provide brain activation maps with better spatial resolution than deoxygenated hemoglobin. Neuroimage 27(4): 947-59.

Cheng K, Waggoner RA, Tanaka K, 2001. Human ocular dominance columns as revealed by high-field functional magnetic resonance imaging. Neuron 32(2): 359-74.

Dale AM, Buckner RL, 1997. Selective averaging of rapidly presented individual trials using fMRI. Hum Brain Mapp 5: 329-40.

Devor A, Dunn AK, Andermann ML, Ulbert I, Boas DA, Dale AM, 2003. Coupling of total hemoglobin concentration, oxygenation, and neural activity in rat somatosensory cortex. Neuron 39(2): 353-9.

Dunn AK, Devor A, Dale AM, Boas DA, 2005. Spatial extent of oxygen metabolism and hemodynamic changes during functional activation of the rat somatosensory cortex. Neuroimage 27(2): 279-90.

Engel SA, Glover GH, Wandell BA, 1997. Retinotopic organization in human visual cortex and the spatial precision of functional MRI. Cereb Cortex 7(2): 181-92.

Friston KJ, Josephs O, Rees G, Turner R, 1998. Nonlinear event-related responses in fMRI. Magn Reson Med 39(1): 41-52.

Glover GH, 1999. Deconvolution of impulse response in event-related BOLD fMRI. Neuroimage 9(4): 416-29.

Grubb RL Jr, Raichle ME, Eichling JO, Ter-Pogossian MM, 1974. The effects of changes in PaCO2 on cerebral blood volume, blood flow, and vascular mean transit time. Stroke 5(5): 630-9.

Hamberg LM, Boccalini P, Stranjalis G, Hunter GJ, Huang Z, Halpern E, Weisskoff RM, Moskowitz MA, Rosen BR, 1996. Continuous assessment of relative cerebral blood volume in transient ischemia using steady state susceptibility-contrast MRI. Magn Reson Med 35(2): 168-73.

Jones M, Hewson-Stoate N, Martindale J, Redgrave P, Mayhew J, 2004. Nonlinear coupling of neural activity and CBF in rodent barrel cortex. Neuroimage 22(2): 956-65.

Kennan RP, Scanley BE, Innis RB, Gore JC, 1998. Physiological basis for BOLD MR signal changes due to neuronal stimulation: separation of blood volume and magnetic susceptibility effects. Magn Reson Med 40: 840-846.

Kennerley AJ, Berwick J, Martindale J, Johnston D, Papadakis N, Mayhew JE, 2005. Concurrent fMRI and optical measures for the investigation of the hemodynamic response function. Magn Reson Med 54(2): 354-65.

Kim SG, Rostrup E, Larsson HB, Ogawa S, Paulson OB, 1999. Determination of relative CMRO2 from CBF and BOLD changes: significant increase of oxygen consumption rate during visual stimulation. Magn Reson Med 41(6): 1152-61.

Lee SP, Duong TQ, Yang G, Iadecola C, Kim SG, 2001. Relative changes of cerebral arterial and venous blood volumes during increased cerebral blood flow: implications for BOLD fMRI. Magn Reson Med 45(5): 791-800.

Leite FP, Tsao D, Vanduffel W, Fize D, Wald L, Dale A, Kwong K, Orban GA, Rosen BR, Tootell RB, Mandeville JB, 2002. Repeated fMRI using Iron Oxide Contrast Agent in Awake, Behaving Macaques at 3 Tesla. NeuroImage 16(2): 283-94.

Leite FP, Vanduffel W, Tootell RB, Mandeville JB, 2004. Point-Image fMRI Experiments in Awake, Behaving Macaques Proceedings of the 12th ISMRM Meeting.

Leite FP, Vanduffel W, Rosen BR, Mandeville JB, 2005. Comparing Spatial Resolution of IRON and BOLD in Awake Macaques. Proceedings of the 13th ISMRM Meeting.

Leite FP, Mandeville JB, 2006. Characterization of Event-related Designs using BOLD and IRON fMRI. NeuroImage 29(3): 901-9.

Logothetis NK, Guggenberger H, Peled S, Pauls J, 1999. Functional imaging of the monkey brain. Nat Neurosci 2: 555-562.

Lu H, Golay X, Pekar JJ, Van Zijl PC, 2003. Functional magnetic resonance imaging based on changes in vascular space occupancy. Magn Reson Med 50(2): 263-74.

Lu H, Soltysik DA, Ward BD, Hyde JS, 2005. Temporal evolution of the CBV-fMRI signal to rat whisker stimulation of variable duration and intensity: a linearity analysis. Neuroimage 26(2): 432-40.

Lu H, van Zijl PC, 2005. Experimental measurement of extravascular parenchymal BOLD effects and tissue oxygen extraction fractions using multi-echo VASO fMRI at 1.5 and 3.0 T. Magn Reson Med 53(4): 808-16.

Mandeville JB, Marota JJ, Kosofsky BE, Keltner JR, Weissleder R, Rosen BR, Weisskoff RM, 1998. Dynamic functional imaging of relative cerebral blood volume during rat forepaw stimulation. Magn Reson Med 39(4): 615-24.

Mandeville JB, Marota JJA, Ayata C, Zaharchuk G, Moskowitz MA, Rosen BR, Weisskoff RM, 1999. Evidence of a Cerebrovascular Post-arteriole Windkessel with Delayed Compliance. J Cereb Blood Flow Metab 19: 679-689.

Mandeville JB, Marota JJ, 1999. Vascular filters of functional MRI: spatial localization using BOLD and CBV contrast. Magn Reson Med 42(3): 591-8.

Mandeville JB, Jenkins BG, Chen YC, Choi JK, Kim YR, Belen D, Liu C, Kosofsky BE, Marota JJ, 2004. Exogenous contrast agent improves sensitivity of gradient-echo functional magnetic resonance imaging at 9.4 T. Magn Reson Med 52(6): 1272-81.

Marota JJ, Ayata C, Moskowitz MA, Weisskoff RM, Rosen BR, Mandeville JB, 1999. Investigation of the early response to rat forepaw stimulation. Magn Reson Med 41(2): 247-52.

Mechelli A, Price CJ, Friston KJ, 2001. Nonlinear coupling between evoked rCBF and BOLD signals: a simulation study of hemodynamic responses. Neuroimage 14(4): 862-72.

Miller KL, Luh WM, Liu TT, Martinez A, Obata T, Wong EC, Frank LR, Buxton RB, 2001. Nonlinear temporal dynamics of the cerebral blood flow response. Hum Brain Mapp 13(1): 1-12.

Ngai AC, Jolley MA, D'Ambrosio R, Meno JR, Winn HR, 1999. Frequency-dependent changes in cerebral blood flow and evoked potentials during somatosensory stimulation in the rat. Brain Res 837(1-2): 221-8.

Olman CA, Van de Moortele P-F, Ugurbil K, 2004. Point spread function for gradient echo and spin echo BOLD fMRI at 7 T. Proceedings of the 12th ISMRM Meeting.

Park JC, Ronen I, Toth LJ, Ugurbil K, Kim DS, 2004. Comparison of point spread functions of BOLD abd ASL fMRI at an ultra-high magnetic field, 9.4 T. Proceedings of the 12th ISMRM Meeting.

Park JC, Ronen I, Kim DS, Ugurbil K, 2005. Spatial specificity of high resolution gradient echo (GE) BOLD and spin echo (SE) BOLD fMRI in cat visual cortex at 9.4 T. Proceedings of the 13th ISMRM Meeting.

Siegel AM, Culver JP, Mandeville JB, Boas DA, 2003. Temporal comparison of functional brain imaging with diffuse optical tomography and fMRI during rat forepaw stimulation. Phys Med Biol 48(10): 1391-403.

Sheth SA, Nemoto M, Guiou M, Walker M, Pouratian N, Toga AW, 2004. Linear and nonlinear relationships between neuronal activity, oxygen metabolism, and hemodynamic responses. Neuron 42(2): 347-55.

Stefanovic B, Pike GB, 2005. Venous refocusing for volume estimation: VERVE functional magnetic resonance imaging. Magn Reson Med 53(2): 339-47.

Thompson JK, Peterson MR, Freeman RD, 2003. Single-neuron activity and tissue oxygenation in the cerebral cortex. Science 299(5609): 1070-2.

Thompson JK, Peterson MR, Freeman RD, 2005. Separate spatial scales determine neural activity-dependent changes in tissue oxygen within central visual pathways. J Neurosci 25(39): 9046-58.

Villringer A, Rosen BR, Belliveau JW, Ackerman JL, Lauffer RB, Buxton RB, Chao YS, Wedeen VJ, Brady TJ, 1988. Dynamic imaging with lanthanide chelates in normal brain: contrast due to magnetic susceptibility effects. Magn Reson Med 6(2): 164-74.

van Bruggen N, Busch E, Palmer JT, Williams SP, de Crespigny AJ, 1998. High-resolution functional magnetic resonance imaging of the rat brain: mapping changes in cerebral blood volume using iron oxide contrast media. J Cereb Blood Flow Metab 18(11): 1178-83.

Vazquez AL, Noll DC, 1998. Nonlinear aspects of the BOLD response in functional MRI. Neuroimage 7(2): 108-18.

Weissleder R, Elizondo G, Wittenberg J, Lee AS, Josephson L, Brady TJ, 1990. Ultrasmall superparamagnetic iron oxide: an intravenous contrast agent for assessing lymph nodes with MR imaging. Radiology 175(2): 494-8.

Zhao F, Wang P, Hendrich K, Kim SG, 2005. Spatial specificity of cerebral blood volume-weighted fMRI responses at columnar resolution. Neuroimage 27(2): 416-24.

Zhao F, Wang P, Hendrich K, Ugurbil K, Kim SG, 2006. Cortical layer-dependent BOLD and CBV responses measured by spin-echo and gradient-echo fMRI: insights into hemodynamic regulation. Neuroimage 30(4): 1149-60.